Quantum Optics in the Photon Number Basis

Der Naturwissenschaftlichen Fakultät
der Universität Paderborn
zur
Erlangung des Doktorgrades Dr. rer. nat.
vorgelegt von

JOHANNES TIEDAU

To Miriam

Table of Contents

Summary

Quantum optics is a rapidly advancing field that enables many new applications, especially in communication and sensing. Two perspectives, depending on the measurement, are found in this field, namely the continuous-variable (CV) and discrete variable (DV) pictures. In this thesis, we want to combine these perspectives by applying CV interpretations and DV counting techniques with new methods towards mesoscopic quantum states.

We will discuss newly developed methods in quantum state generation, detection, and characterization. For state generation, we show a new method to efficiently calculate photon-number probabilities and use it to find limits for generating higher-order Fock states in parametric down-conversion. We show the generation of higher-order Fock states up to $n = 7$ with high generation rates above 1000 counts/s, which are possible due to high squeezing values above 11 dB. On the detection side, we enhance current multiplexing schemes that enable photon-number resolved measurements using binary detectors. Using a novel time-multiplexing unit with 2x128 time bins, we increase existing characterization tools beyond the few-photon level and reveal non-classical signatures of up to ten photons spread over up to 64 modes with correlation functions. Additionally, we also demonstrate a new measurement scheme with a massively increased dynamic range of 123 dB, which can handle average powers in the nW range. This enables us to perform quantum characterizations in a completely new regime, making it possible to directly compare single-photon detectors with of-the-self power meters. Finally, we combine our generation and detection work to experimentally show quantum tomography with three new characterization schemes based on overlap variations and phase space sampling that allow for higher losses and stronger phase fluctuations. We develop a new 'truly local' local oscillator approach that helps us to overcome existing power and security constraints.

Although all measurements are made in the photon number basis, we discuss the reconstructed state in the phase-space picture and show that the interplay between CV and DV pictures enables new, robust measurements with applications in metrology and quantum communication, pushing ahead the field as a whole.

Zusammenfassung

Die Quantenoptik ist ein rasant wachsendes Gebiet mit Anwendungen im Bereich der Kommunikation und der Metrologie. Zwei Sichtweisen werden hierbei besonders häufig verwendet, die als kontinuierliche Variablen (CV) und diskrete Variablen (DV) bezeichnet werden. In dieser Arbeit verbinden wir beide Perspektiven im Hinblick auf mesoskopische Zustände, indem wir DV Messungen im CV Bild interpretieren.

Wir werden neue Methoden im Bereich der Zustandserzeugung, Detektion und der Charakterisierung diskutieren. Für die Erzeugung zeigen wir eine neue, effiziente Methode für die Berechnung von Photonen-Wahrscheinlichkeiten, die es ermöglicht die Limitationen der parametrischen Fluoreszenz in Hinblick auf höhere Fock-Zustände zu finden. Wir zeigen die Erzeugung von Fock Zuständen bis $n = 7$ mit hohen Raten über 1000 Events pro Sekunde, die durch hohe Squeezing-Werte über 11 dB erreicht werden. Im Bereich der Detektion werden wir Multiplexverfahren weiterentwickeln, die Photonenzahlmessungen ermöglichen, selbst wenn die Detektoren dazu nicht in der Lage sind. Mit einem neuen Zeitmultiplexverfahren mit 2x128 Zeitmoden erweitern wir bestehende Charakterisierungsmöglichkeiten jenseits des Einzelphotonenlevels und zeigen Nicht-Klassizität mit bis zu zehn Photononen in 64 Moden. Zusätzlich zeigen wir ein neues Messschema mit einem stark erweiterten dynamischen Umfang, der sich bis in den nW Bereich erstreckt und somit die Charakterisierung in einem völlig neuen Regime ermöglicht. Durch diese Methode ist es möglich Einzelphotonendetektoren direkt mit herkömmlichen Powermetern zu vergleichen. Abschließend werden wir Erzeugung und Detektion für die experimentelle Charakterisierung verwenden. Drei neue Verfahren, basierend auf der Variation des Messüberlapps und des Phasenraumsamplings, ermöglichen es stärkere Verluste und Phasenfluktuationen zu tolerieren. Wir führen einen „tatsächlich lokalen“ Lokaloszillators ein der bisherige Leistungs- und Sicherheitsbeschränkungen aufhebt.

Obwohl alle Messungen in der Photonenzahlbasis durchgeführt werden, diskutieren wir die Ergebnisse im Phasenraumbild und zeigen, dass dies neue und robuste Messungen mit Anwendungen in der Metrologie und Quantenkommunikation ermöglicht.

CHAPTER 1

Introduction

Explaining the properties of light and understanding its nature is a fascinating topic that has been discussed from many perspectives over the last centuries. A very prominent example is a dispute from Isaac Newton and Christiaan Huygens in the 17th century. Newton believed that light was made out of small, solid particles that can, for example, be redirected by an elastic collision (reflection). On the other hand, Huygens postulated that light can be described as a wave [1] to explain the same phenomena. After both scientists had died, the old debate gained further scientific insights with the double-slit experiment by Young in 1802. It seemed that the argument was decided in favor of Huygens' wave theory, because destructive interference effects could not be explained with particles. However, with the work from Planck in 1901 [2] and the discovery of the photoelectric effect and a novel explanation by Einstein in 1905 [3], the particle idea experienced a revival, although in a slightly different form and not as a solid particle. Einstein posited that light can only occur in discretized amounts, which are called photons. After this discovery, quantum theory experienced an enormous growth, which led to the uncovering of surprising features such as entanglement [4–6]. From the application side, a wave-like description stayed mostly sufficient for a rather long time. At first, matter properties were considered as quantum objects (first quantization), which led to the discovery of the maser [7] and laser [8]. This was a milestone for optics that opened many paths of research because light fields with well-defined properties could be generated. Quantum optics was one of these new research fields. With the first generation of non-classical states [9] (states that cannot be explained with a classical theory), the era of second quantization became practically important, and the electromagnetic wave was finally treated as a quantum object.

From a modern perspective, still, two descriptions of the light field are popular, to some extent analogous to the discussion from Newton and Huygens. On the one hand, we can describe light in terms of different photon numbers n that can occur. Importantly, and in contrast to the classical particle picture, the different photon numbers can have special relations, which are called coherence terms [10]. This description is known as the discrete variable (DV) perspective, as photons can only ever be measured in discretized values. On the other hand, we have a wave-inspired picture, where we measure amplitude and phase of the electromagnetic wave. This is called the continuous variable (CV) picture because these measurements have a continuous outcome spectrum. Both views can completely characterize an arbitrary quantum state. Depending on the exact application and measurement, one or the other might be more efficient or insightful and it is common to stick to one of the two sides. Nevertheless, a number of links have been established (e.g. [11–16]). One additional problem is that these works are often restricted to the few photon regime. Scaling, however, is a crucial factor for quantum technologies as many systems show their advantages for an increasing size, such as boson sampling [17], quantum sensing [18], or high-dimensional quantum cryptography [19]. Unfortunately, the scaling process is non-trivial because an increasing size often enforces new experimental constraints such as lower acceptable loss values. Also detecting larger states requires, in general, completely new

measurement schemes that can enable efficient readouts.

In this thesis, we will address these points and strengthen the connection between the CV and DV picture combined with new detection methods towards the characterization of mesoscopic quantum states. As a common theme, we will perform measurements in the photon number basis i.e. DV measurements. Nevertheless, we will often interpret our results (especially in Chap. 4) from the CV perspective. We will show new measurement schemes for the detection of large quantum states as well as new characterization methods that allow us to perform quantum tomography in these new parameter regimes.

The structure of this thesis is as follows: At first, we will introduce the parametric down-conversion process (PDC) in Chap. 2, which is one of the most widely used processes to generate non-classical states of light. Generating these quantum states is a non-trivial task and we will briefly discuss existing PDC applications, especially for single-photon generation. As a next step, we will discuss our new work regarding the generation of higher-order photon-number states. Although highly desirable for various applications, these special states are extremely fragile and difficult to generate. In fact, we will show some fundamental limitations for their generation via PDC with a new theoretical approach to describe the generated multimode states efficiently. In Chap. 3 we will focus on detection techniques in the photon number basis. Single-photon detection is a fast-growing field, with great improvements on the detector side over the last years. Nevertheless, many detectors are not intrinsically photon-number resolving, which led to the idea of detector multiplexing [20–25]. In detector multiplexing, an incoming light pulse is distributed over many detectors to allow for an approximate photon-number resolution. We will demonstrate a new 128-bin time-multiplexing unit and show efficient readout schemes to handle these large multiplexing devices. In addition, we also report on a new detector scheme that can handle detector saturation effects to investigate extremely bright states and a new readout scheme for multi-element detectors. The discussed detection methods will be used in Chap. 4, where we focus on the quantum characterization aspect and show three new methods to characterize quantum states. We will use photon counting in combination with phase-space interpretations to demonstrate these new characterization tools. Finally, we will conclude our work in Chap. 5 and give an outlook on further extensions of our work.

CHAPTER 2

Quantum state generation

Contents

Generating optical states that cannot be explained classically is a non-trivial task. It requires a profound understanding of the underlying physics to design the appropriate generation process. In this thesis, we will focus on parametric down-conversion (PDC), a process where a pump photon decays into two daughter photons to generate these quantum states. PDC is one of the most widely used processes in quantum optics to generate non-classical states and we will discuss existing schemes from the discrete and continuous variable side. Despite the widespread use of PDC, there are still open research questions about PDC applications especially in the multimode regime. We therefore investigate the generation of higher-order Fock states and introduce a new, efficient method to calculate photon number probabilities from multimode PDC states in Sec. 2.3.3. But to start with, we will discuss the physical basics of the underlying process.

2.1 Background

In order to understand and design our desired quantum process, we will consider the underlying physics from the classical perspective first. As a next step, we will quantize our process to learn more about the specific properties of our quantum state.

2.1.1 Nonlinear optics

In nonlinear optics, an optical light field interacts with a medium in a non-trivial way. Non-trivial in this context means that we can see effects on top of the well-known interactions such as reflection and absorption. Frequency modifications in a medium are, for example, a clear indication of nonlinear effects. Historically, one of the major challenges in nonlinear optics was the required light intensity to see these higher-order effects. With the discovery of stimulated light emission in lasers, optical fields were strong enough to see, for example, frequency doubling in a nonlinear optical crystal [26].

The deeper reason behind the generation of new frequencies are accelerated charges inside the nonlinear medium, which can create new electromagnetic waves. An incoming light field can dynamically change the orientation of atomic dipoles $\mathbf{p}$. The combination of N dipoles will lead to an overall polarization $\mathbf{P} = N\mathbf{p}$. The relation between the polarization $\mathbf{P}$ and the electric field is given by the so-called electric susceptibility χ, a material property that quantifies the

degree of polarization given an electric field

$$\mathbf{P} = \varepsilon_0 \chi \mathbf{E} \,. \tag{2.1}$$

To give a more formal definition of nonlinear optics, we can expand the polarization in terms of the electric field

$$\mathbf{P} = \varepsilon_0 \left(\chi^{(1)}\mathbf{E} + \chi^{(2)}\mathbf{E}\mathbf{E} + \chi^{(3)}\mathbf{E}\mathbf{E}\mathbf{E} \right) \,. \tag{2.2}$$

If the polarization depends linearly ($\chi^{(1)}$) on the electric field, resulting effects are considered as linear optics. We will only consider the first nonlinear term mediated by $\chi^{(2)}$ in this thesis and neglect higher-order terms, which have a cubic (or even higher) dependence on the electric field. Depending on the frequency combinations involved, these processes have established names such as difference frequency generation (DFG), sum-frequency generation (SFG), second harmonic generation (SHG, special case of SFG) or optical rectification (OR). In this thesis, we will only consider second-harmonic generation, where the incoming light field is doubled in frequency and the decay of a high-frequency photon into two daughter photons with lower energy, known as parametric down-conversion (PDC). To capture the full dynamic behavior, we will now explicitly write out the time dependency of the parameters e.g. $E(t)$, which will become important in the following.

Up to now, all fields were treated classically. A very common method to quantize these fields is to start with the energy (Hamiltonian) of the system. As a preparatory step, we can therefore write the total energy in a nonlinear medium, which is given by [27]

$$H(t) = \int d^3r \left(\int_0^{\mathbf{H}(t)} \mathbf{B}(t) \cdot \delta\mathbf{H}'(t) + \int_0^{\mathbf{D}(t)} \mathbf{E}(t) \cdot \delta\mathbf{D}'(t) \right) \,, \tag{2.3}$$

with a magnetic flux density $\mathbf{B}(t)$, a magnetic field strength $\mathbf{H}(t)$ and an electric displacement field $\mathbf{D}(t) = \varepsilon_0\mathbf{E}(t) + \mathbf{P}(t)$. Instead of using this rather complex equation, we will use the better-known equation of a linear medium instead

$$H(t) = \frac{1}{2} \int d^3r \mathbf{B}(t)\mathbf{H}(t) + \mathbf{E}(t)\mathbf{D}(t) \,, \tag{2.4}$$

which gives the same results up to normalization constants.

2.1.2 Quantizing the Hamiltonian

The quantization of the electromagnetic field is a complex process and a variety of methods have been suggested [28–30]. As a rather easy first step, we will quantize a monochromatic electromagnetic field with an angular frequency ω inside a defined volume V (e.g. [31]). The resulting potential is described by a quadratic function of a harmonic oscillator. Solving the eigenequation of the Hamilton operator we can find the discrete energy eigenstates, as shown in Fig. 2.1. The energy eigenvalues are given by $E_n = \hbar\omega(n + \frac{1}{2})$. Due to the structure of the Hamilton operator, the energy eigenstates are directly linked to photon numbers n. Therefore

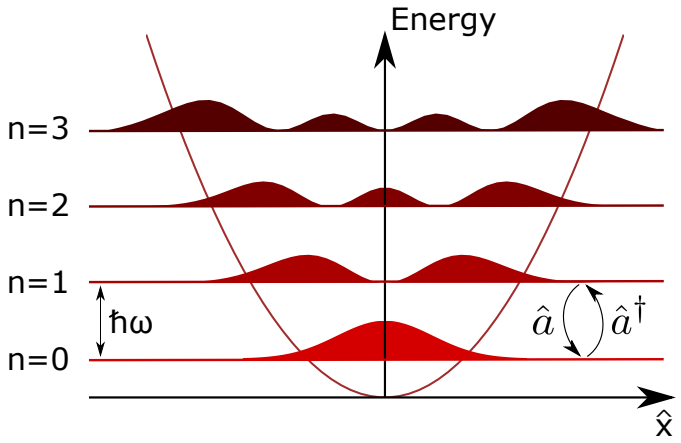

Figure 2.1 – Probability densities of the four lowest energy eigenstates in a harmonic potential. Transitions between these states can be made with the annihilation $\hat{a}$ or creation $\hat{a}^\dagger$ operator. See text for further details.

we can identify each eigenstate with a photon number. We can also define the annihilation $\hat{a}$ and creation $\hat{a}^\dagger$ operators as introduced by Dirac for transitions between the photon-number states $|n\rangle$

$$\begin{aligned} \hat{a}\,|n\rangle &= \sqrt{n}\,|n-1\rangle \\ \hat{a}^\dagger\,|n\rangle &= \sqrt{n+1}\,|n+1\rangle \ . \end{aligned} \tag{2.5}$$

These fulfill the commutation relation $\left[\hat{a}, \hat{a}^\dagger\right] = 1$, which means that the order of the operators cannot be swapped.

As a next step, we want to consider our nonlinear medium. We can divide the Hamiltonian in Eq. 2.3 into two parts; a harmonic oscillator part, as we have discussed before and, more importantly, an interaction term $H_I(t)$, which is given by the interplay of an electric field $E(t)$ and the nonlinear polarization [32]

$$H_I(t) \propto \int dV\, \mathbf{P}_{\mathrm{NL}}(t) \cdot \mathbf{E}(t) \ . \tag{2.6}$$

We can expand this equation via Eq. 2.2 to

$$H_I(t) \propto \int dV\, \chi^{(2)}_{klm} \mathbf{E}_k(t) \mathbf{E}_l(t) \mathbf{E}_m(t) \ . \tag{2.7}$$

In general, Eq. 2.7 includes 27 possible combinations of the three fields. As discussed before, we only want to focus on the PDC case where a pump photon decays into two daughter photons.

By quantizing the electric field, we can write the PDC Hamiltonian as

$$\hat{H}_{\text{PDC}}(t) \propto \int dV\, 2\hat{E}_p^{(+)}(t) \underbrace{\left(\hat{E}_1^{(-)}(t)\right)^2}_{\text{part I}} + \hat{E}_p^{(+)}(t) \underbrace{\hat{E}_1^{(-)}(t)\hat{E}_2^{(-)}(t)}_{\text{part II}} + h.c.\,, \tag{2.8}$$

with the electric field operator

$$\hat{E}_j^{(-)}(t) = \hat{E}_j^{(+)\dagger}(t) \propto \int d\omega_j \exp\left[-i(k_j z + \omega_j t)\right] \hat{a}_j^\dagger(\omega_j)\,. \tag{2.9}$$

We can see that the down-converted photons can either be generated in the same (part I) or orthogonal polarization modes (part II), which we call signal and idler modes. We refer to these cases as a type I or a type II PDC process, respectively.

The derived Hamiltonian $\hat{H}_{\text{PDC}}(t)$ completely describes the (quantum) behavior of our process. We are interested in calculating the resulting quantum state $|\Psi_{\text{out}}\rangle$ for a given input state $|\Psi_{\text{in}}\rangle$, which is given by a unitary transformation $\hat{U}$

$$|\Psi_{\text{out}}\rangle = \hat{U}\,|\Psi_{\text{in}}\rangle\ , \tag{2.10}$$

resulting from the Schrödinger equation. Unfortunately, we cannot use the simple definition $\hat{U} = \exp\left(i\hat{H}t/\hbar\right)$ because our PDC Hamiltonian is time dependent[1]. Therefore, we have to integrate over the interaction time to derive our unitary operator

$$\hat{U}_{\text{PDC}} = \exp\left[-\frac{i}{\hbar}\int dt\, \hat{H}_{\text{PDC}}(t)\right]\,. \tag{2.11}$$

To evaluate this expression further, we make some assumptions: The pump field has a very high mean photon number, which justifies a classical treatment. This allows us to perform the integration over the pump frequency and the integration over the crystal length (we assume a waveguided crystal, which allows us to integrate over the transversal coordinates giving a constant factor [35]). Finally, we can derive our desired unitary operator [36]

$$\hat{U}_{\text{PDC}} = \exp\left[-\frac{i}{\hbar}\left(A\int d\omega_s \int d\omega_i\, \alpha(\omega_s+\omega_i)\Phi(\omega_s,\omega_i)\hat{a}_s^\dagger(\omega_s)\hat{a}_i^\dagger(\omega_i) + h.c.\right)\right]\,, \tag{2.12}$$

with a pump function $\alpha(\omega_p)$ and a phase-matching function

$$\Phi(\omega_s,\omega_i) = \text{sinc}\left(\frac{(k_p-k_s-k_i)L}{2}\right)\exp\left(i\frac{(k_p-k_s-k_i)L}{2}\right) \tag{2.13}$$

over a nonlinear crystal of length L.

[1] Actually the situation is even worse, as the Hamiltonian does not even commute with itself for different times. To give a physical explanation for this: If a very large amount of pump photons decay into daughter photons, these new photons can reconvert to a pump photon. These additional conversion paths are called time-ordering effects. The effect of time-ordering has been studied [33, 34] but is rather small for PDC, especially in the low gain regime. Therefore, we will neglect the effects of time-ordering throughout this thesis.

Over the last decades, a number of naming conventions have been established to describe the PDC process, which we will also use in this thesis:

- We see that the spectral properties of the PDC state can be summarized in a so-called **joint spectral amplitude (JSA)** function $f(\omega_s, \omega_i) = \alpha(\omega_s + \omega_i)\Phi(\omega_s, \omega_i)$.
- We refer to this state as a **spontaneous parametric down-conversion (SPDC)** state if the PDC process is acting on the vacuum field $|\Psi_{\text{SPDC}}\rangle = \hat{U}_{\text{PDC}}\,|0\rangle$. In general, the PDC operation can be applied to any input state, which is known as **seeding** when the input state is non-vacuum.
- The resulting state after a type-II (or a type-I, where the generated photon pairs can be separated in frequency) PDC process is called a **two-mode squeezed** state. Otherwise, it is a **single-mode squeezed** state. We will revisit squeezed states from an intuitive perspective in Sec. 2.4.1.

As a last step, we want to write down the single-mode and two-mode squeezed vacuum states (TMSV) in the photon number basis. To simplify this step, we will only consider the output state in a single spectral mode and therefore drop time and frequency dependencies. After some algebra, as shown in [37], we can derive our states

$$|\Psi_{\text{SPDC, single-mode}}\rangle = \sqrt{\text{sech}(r)}\sum_{n=0}^{\infty}\tanh^n(r)\frac{\sqrt{(2n)!}}{2^n n!}\,|2n\rangle\ , \tag{2.14}$$

and

$$|\Psi_{\text{SPDC, two-mode}}\rangle = \text{sech}(r)\sum_{n=0}^{\infty}\tanh^n(r)\,|n,n\rangle\ . \tag{2.15}$$

2.1.3 Time-frequency modes

Before we can start to discuss applications that involve PDC, we want to review the concept of time-frequency modes (sometimes also known as temporal modes [38]). Throughout this thesis we will use pulsed laser light, which has a broad spectral distribution in the frequency domain. However, the quantization of the vacuum modes only considered single-mode creation and annihilation operators $\hat{a}^\dagger$ and $\hat{a}$, respectively. To capture quantum states in broadband modes, sets of broadband operators were introduced [39]

$$\hat{A}_j^\dagger = \int d\omega\, f_j(\omega)\hat{a}_j^\dagger(\omega)\ , \tag{2.16}$$

with normalized weight functions $f_j(\omega)$. These operators still fulfill the standard bosonic commutation relation $[\hat{A}_j, \hat{A}_k^\dagger] = \delta_{jk}$. In addition, it is very convenient to consider complete $\sum_j f_j^*(\omega)f_j(\omega') = \delta(\omega - \omega')$ and orthogonal $\int d\omega\, f_j^*(\omega)f_k(\omega) = \delta_{jk}$. If we analyze the free-space case, no basis is preferred. However, for the PDC process, we will see that a description in a specific mode naturally follows, such as Hermite-Gauss modes [40, 41].

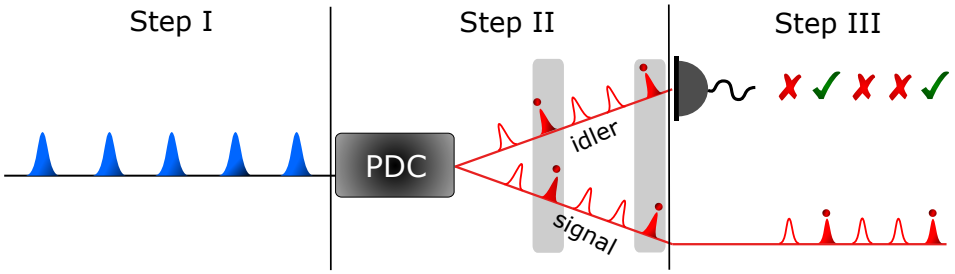

Figure 2.2 – Schematic illustrating the generation of single-photon states via SPDC. Step I: A high-energy pulse train is sent to a nonlinear material. Step II: Pump pulses are probabilistically decaying into pairs of signal and idler photons via SPDC. Step III: The idler mode is measured with a single-photon detector. Due to the detection and photon number correlations between signal and idler modes, the positions of single-photons are known.

2.2 PDC for generating single-photon states

One of the main applications for SPDC is the generation of single photons. These states are highly relevant for many situations, for example, in fundamental physics [42, 43] or metrology [18, 44]. In this section, we will briefly review important aspects of the single-photon generation with SPDC, before we start to discuss our new analysis of generating higher-order Fock states in the next section.

We have already derived the SPDC state in the photon-number basis in Eq. 2.15. As each pump photon can only decay into a pair of signal and idler photons, we always have perfect photon-number correlations in these modes. Therefore, by detecting one photon in the idler mode, we can be certain that we also have one photon in the signal mode. Due to the probabilistic nature of the decay process, we cannot predict when a pump photon decays, but we have an indicator (herald) for it, as shown in Fig. 2.2. This process is known as heralding and is one of the most widely used methods to generate single photons [45–49]. Still, many imperfections such as losses, spectral correlations, or noise contributions from higher-order photon components (more than one pump photon decays) will decrease the quality of the heralded state. All these limitations have been studied in detail for the single-photon generation by *Christ et al.* [50]. We have to differentiate fundamental limitations resulting from the probabilistic nature of SPDC and adjustable factors such as losses and spectral properties. In the following, we want to focus on spectral properties, which are highly relevant for optimizing the quality of the heralded single-photon state.

2.2.1 Spectral properties

A crucial factor in the heralding process are spectral correlations between signal and idler modes. If these correlations are present, the heralding process will project the signal photon in a mixed state and degrades the usability for many following applications. Therefore it is desirable to

produce a decorrelated SPDC state, which can produce pure single-photon states. To quantify this aspect, we have to analyze the JSA function $f(\omega_s, \omega_i)$. This function describes all spectral correlations between signal and idler modes. We want to investigate this function further in order to generate quantum states with tailored properties.

Schmidt decomposition

As a first step, we need to quantify the correlations by analyzing the JSA function $f(\omega_s, \omega_i)$ [51]. To do so, we will use a mathematical tool known as the singular-value decomposition (in this context known as the Schmidt decomposition) to write this function as a tensor product of two orthonormal sets $\{|\phi\rangle_k\}$ and $\{|\psi\rangle_k\}$ [36, 52]

$$-\frac{i}{\hbar} A f(\omega_s, \omega_i) = B \sum_k \lambda_k |\phi\rangle_k \otimes |\psi\rangle_k \ . \tag{2.17}$$

The factors $\lambda_k \geq 0$ are called Schmidt coefficients, which are labeled in descending order $\lambda_k \geq \lambda_{k+1}$ and the individual states $|\phi\rangle_k \otimes |\psi\rangle_k$ are called Schmidt modes. To express the result from the Schmidt decomposition in a single number we define an effective Schmidt number K [53]

$$K = \frac{1}{\sum_k \lambda_k^4} \ . \tag{2.18}$$

This Schmidt number K quantifies our desired goal of measuring the spectral correlations. A Schmidt number of one implies no correlations between signal and idler modes, which means that measuring the idler mode does not improve our knowledge about the signal mode. Spectral correlations are indicated by a higher Schmidt number. With these definitions, we can also define a squeezing value r_k per mode k [36]

$$r_k = B\lambda_k \ . \tag{2.19}$$

The value is often quantified in a logarithmic way via squeezing [dB] $= -10 \log_{10}(\mathrm{e}^{-2r_k})$. This squeezing parameter also defines the mean photon number per mode

$$\langle n_k \rangle = \sinh^2(r_k) \ . \tag{2.20}$$

However, it is often advantageous to quantify the optical pump strength independently of the Schmidt decomposition. For this purpose, the more general optical gain parameter B is used, which is the generalized version of the squeezing parameter for multimode systemes (also typically given in dB). Experimentally this parameter can be modified by changing the pump intensity and therefore the PDC decay probability. We can now write our SPDC state as a product of two-mode squeezers [37]

$$\begin{aligned} |\Psi_{\text{SPDC}}\rangle &= \hat{U}_{\text{PDC}} |0,0\rangle \\ &= \bigotimes_k |\Psi_{\text{SPDC, two-mode}}\rangle \ . \end{aligned} \tag{2.21}$$

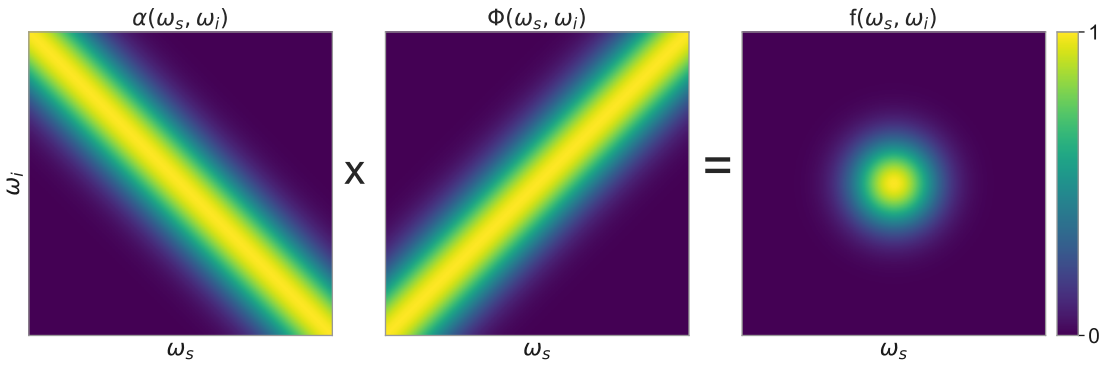

Figure 2.3 – Decorrelated JSA $f(\omega_s, \omega_i)$ with Gaussian pump bandwidth α that is matched to the Gaussian phase-matching bandwidth Φ.

If we can write the JSA as a double Gaussian function, the Schmidt coefficients are exponentially decreasing [54]

$$\lambda_k = \sqrt{1-\mu^2}\mu^k \,, \tag{2.22}$$

with $\mu \in [0, 1]$. For this case, an analytic expression for the Schmidt modes can be found [41].

Spectral engineering

We are now able to quantify spectral correlations in an SPDC state via the JSA function. As a next step, we are interested in ways to modify this behavior. We have seen in Sec. 2.1.2 that the JSA function $f(\omega_s, \omega_i)$ depends on the pump function α and the phase-matching function Φ (illustrated in Fig. 2.3). Both terms (as well as the nonlinear coefficient) need to be sufficiently large in order to enable an efficient nonlinear process. The constraint given by the pump function is directly connected to energy conservation. If a pump photon with the energy E_p decays, the same energy must be present in signal and idler modes (E_s and E_i respectively)

$$E_p = E_i + E_s \,. \tag{2.23}$$

The phase-matching function Φ is linked to momentum conservation with a potential mismatch Δk given by

$$\Delta k = k_p - k_s - k_i \,. \tag{2.24}$$

For some wavelength combinations and nonlinear materials, phase matching is directly possible. Small deviations can also be compensated by adjusting the crystal orientation (critical phase matching) or temperature (noncritical phase matching) [55]. However, these variations are often not sufficient to generate the desired wavelength combination. Therefore a process known as periodic poling was invented. Here the crystal orientation is periodically inverted to compensate for the phase mismatch [56]. With this technique, it is possible to design a process with the specified center frequencies. Nevertheless, adjusting the Schmidt number and therefore the correlations inside the JSA can be challenging. For example, the sharp edges at the beginning

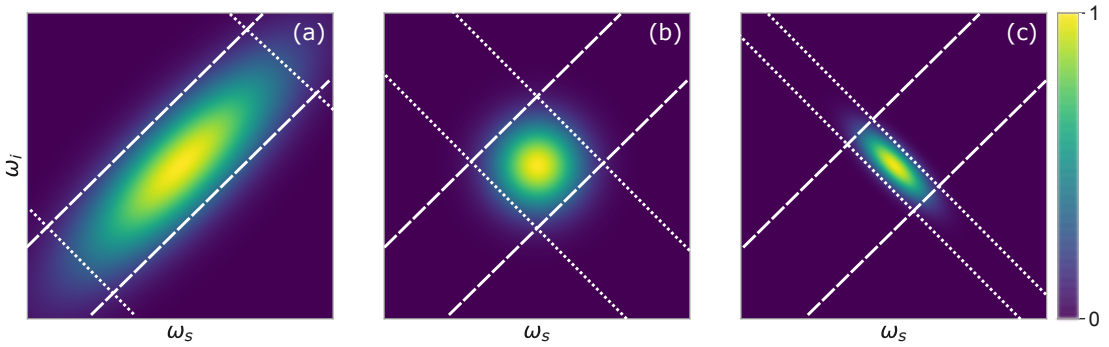

Figure 2.4 – JSA functions of a SPDC state with a broad (a), matched (b), and narrow (c) pump bandwidth. If the pump bandwidth (white dotted) is not matched to the phase-matching function (white dashed), additional correlations in the SPDC state can be seen.

and end of the crystal, where the nonlinearity is suddenly turned on and off, cause a sinc-shaped phase-matching function, which causes additional correlations. Special poling patterns have been investigated to overcome this limitation [57–59].

An additional problem that cannot be solved with periodic poling is the angle between the abscissa and the phase-matching function. In order to create a decorrelated state with bandwidth matched signal and idler photons, it is necessary to have a phase-matching function perpendicular to the pump function. The phase-matching angle is given by the dispersion properties of the material. For communication purposes, light emission at 1550 nm is advantageous, as optical losses in fibers are minimal for this wavelength. Potassium titanyl phosphate (KTP) has become the workhorse for generating decorrelated states at this wavelength, as it offers nearly $45°$ phase matching.

Last but not least, the crystal length will change the phase-matching bandwidth. It is necessary to adjust the pump bandwidth to match the phase-matching bandwidth to avoid additional correlations, as shown in Fig. 2.4. This process, combined with selecting an appropriate phase-matching function, is often referred to as spectral engineering and has been shown first for bulk crystals at 830 nm [60]. Later the material was changed to KTP to enable single-mode emission at 1550 nm [61–63]. Figure 2.3 shows the perfect case of a decorrelated state where phase-matching bandwidth and pump bandwidth are matched.

In principle, spectral filtering could be used to generate a decorrelated JSA. However, this comes with the cost of additional losses [64]. Therefore, spectral engineering is crucial for high performance single-mode PDC emission, which enables the generation of pure single-photon states.

2.2.2 Solutions for deterministic single-photon generation

To overcome the fundamental limitations of SPDC, two solutions are possible. Firstly, the probabilistic nature of SPDC can be overcome by combining multiple sources into one channel (source multiplexing), as summarized in a recent review article by *Meyer-Scott et al.* [65]. To do so, an active element and fast processing (feed-forward) is crucial. Secondly, it is also possible to generate single-photon states with a deterministic process. For example, quantum dots are investigated in this context, but they often suffer from different disadvantages such as lower indistinguishability or fidelity [66], although many solutions are discussed [67–69]. Nevertheless, PDC has the advantage that additional states can be generated with this process. One example is the already mentioned generation of higher-order Fock states, which we will discuss in the next section.

2.3 PDC for generating higher-order Fock state

Fock states, also known as photon-number states, are fascinating fundamental quantum states. These states are highly non-classical as they have no energy uncertainty. In contrast, we are still able to understand these states intuitively from the DV particle picture [70]. In addition to the fundamental point of view, Fock states are also essential from the application perspective. For example, Fock states are a key resource to generate Schrödinger cat states [71] or Holland-Burnett states which are advantageous for phase estimation [72]. Besides, Fock states also have the potential to improve spectroscopy applications [73–75], and quantum information processing protocols [76].

Despite their broad interest, generating Fock states is a challenging task and various ways have been explored [77–81]. In this section, we will discuss how high-order Fock states can be generated with spontaneous parametric down-conversion (SPDC). In previous theoretical works, only up to two photons or Schmidt modes have been considered [50, 82, 83]. We use a new method to theoretically investigate the limitations of SPDC for Fock state generation with up to seven photons and 35 modes and compare our theory with experimental data. The content of this section was published in [84].

2.3.1 Generation scheme

The most common method to generate higher-order Fock states is a type-II SPDC process [85–90]. This process is very similar to the single-photon generation scheme. The main difference is that we will deliberately enforce multiple decay events, which results in multiple photon pairs in the signal and idler modes. As these photons are always produced in pairs from a pump photon, the signal and idler modes show perfect photon-number correlation. Therefore, post-selecting (heralding) on a specific photon number n in the idler mode enables the preparation of an n-photon number state in the signal mode, which can be used for further purposes. One drawback of generating higher-order Fock states with SPDC is again the probabilistic nature of this process. To some extent, the generation probability can be changed by varying the incoming pump intensity and, therefore, the chance of a photon decay. The photon number probability p_n of generating an n-photon state will be a key parameter in the following calculations. The second

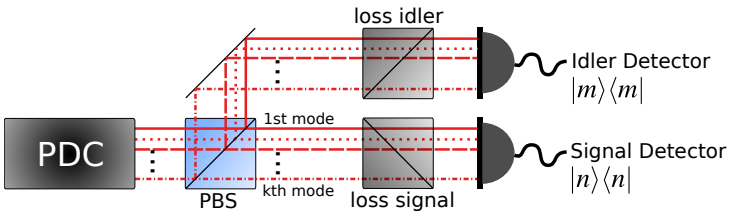

Figure 2.5 – A two-mode squeezed state is generated with parametric down conversion (PDC). The polarization modes, named signal and idler, are split on a polarizing beam splitter (PBS). Losses and multimodeness will influence the detected signal state that is prepared given a specific measured photon number in the idler mode. Reprinted from [84]. ©2019 by American Physical Society

important figure of merit is the fidelity of the generated state to a single-mode n-photon Fock state. Two main mechanisms can degrade the quality of the produced state, namely losses and multimodeness. The calculation of the state fidelity in the presence of (spectral) multimodeness presents a particularly challenging problem.

2.3.2 Parametric down-conversion limitations: single-mode

As we have seen in Sec. 2.2.1 the general multimode SPDC state $|\psi\rangle_{\text{PDC}}$ can be described as a product of two-mode squeezed vacuum states in orthogonal modes k

$$|\psi\rangle_{\text{PDC}} = \bigotimes_{k=1}^{\infty} \sqrt{1-|\Lambda_k|^2} \sum_{n=0}^{\infty} \Lambda_k^n \, |n,n\rangle_k \ . \tag{2.25}$$

Here $\Lambda_k = \tanh(r_k)$ defines the squeezing as a function of the squeezing parameter r. In the following, we will analyze the limitations of this process for the single-mode case and then generalize our findings with a new theoretical tool for the multimode case.

As a first step, we will consider the single-mode case ($\Lambda_{k\neq 1} = 0$). We will denote this case with a capital $K = 1$ and consider the idler mode as the heralding arm $\rho_i = \text{tr}_s(|\psi\rangle\langle\psi|_{\text{PDC},K=1})$. The probability p_n of heralding an n-photon state in the idler arm is then given by

$$\begin{aligned} p_{n,K=1} &= \text{tr}\left(|n\rangle\langle n| \, \rho_i\right) \\ &= (1-|\Lambda_1|^2)\Lambda_1^{2n} \\ &= q_1(1-q_1)^{2n} \ , \end{aligned} \tag{2.26}$$

where the vacuum probability $q_1 = (1-|\Lambda_1|^2)$ was introduced. If we want to maximize the heralding probability for a specific photon number, we can change the pump power to change the squeezing strength. As we can see from Eq. 2.26 the photon number p_n is given by a geometric

distribution. Therefore each photon number n has a maximum generation probability

$$p_{\max,K=1}(n) = \frac{n^n}{(1+n)^{1+n}} \,. \tag{2.27}$$

This means that the PDC pump power can be varied to optimize the heralding probability p_n, but the maximum value exponentially decreases with the photon number n.

In addition to the heralding probability, we will investigate the quality of the heralded state. Therefore we choose the fidelity $\mathcal{F}$ to the desired n-photon Fock state as the figure of merit [91]. We will assume ideal photon number resolution for the detection, which is approached in practice by transition edge sensor (TES) detectors [92]. In this chapter, we will treat detectors as a black box with perfect properties (n photons produce an n-detection event and detectors have a frequency-independent response). We will discuss further details about the detection process in Chap. 3. The dominating experimental imperfection that needs to be considered is optical loss. In contrast to the limits of the heralding probability, unit fidelity can be reached in principle. As a first step, we will only take losses for the heralding arm into account as losses for the heralded mode will depend on the actual application scenario. We have already discussed the measurement operator for lossy photon number detection Π_n with a transmission η in Eq. 3.4. Therefore the heralded signal state after the detection of n photons in the idler mode can be written as

$$\rho_s = \frac{\mathrm{tr}_i(\Pi_n \left|\psi\right\rangle\!\left\langle\psi\right|)}{\left\langle\psi\right| \Pi_n \left|\psi\right\rangle} \,. \tag{2.28}$$

With this result, the fidelity to the desired Fock state $\left|n\right\rangle$ can be written as

$$\begin{aligned} \mathcal{F}(\left|n\right\rangle\!\left\langle n\right|, \rho_s) &= \left\langle n\right| \rho_s \left|n\right\rangle \\ &= \frac{\eta^n q_1 (1-q_1)^{2n}}{\sum_{i=n}^{\infty} \binom{i}{n} (1-\eta)^{i-n} \eta^n q_1 (1-q_1)^{2i}} \,. \end{aligned} \tag{2.29}$$

Heralding probability and heralded state fidelity are shown in Fig. 2.6 (a,b) as a function of the optical gain, which is equivalent to the squeezing parameter in the single-mode case. All plots are shown for three different loss values in the heralding arm, and three heralded photon numbers.

It can be seen that the general shape of the heralding probability is independent of heralding losses. Losses can always be counteracted with higher squeezing values. This effect can be explained if we consider only the idler mode of the two-mode squeezed vacuum (signal mode is traced out). The resulting state is a thermal state, which stays thermal under losses.

The situation is quite different for the heralded state fidelity. For the lossless case, detecting n photons in the heralding mode will project the heralded state to an n-photon Fock state. However, if we consider losses in the heralding arm, heralding n photons in the heralding mode will project on at least n photons in the signal mode, as additional photons could have been lost. These additional higher-order photon number contributions will lower the fidelity. It can be seen that both higher losses and stronger squeezing increase these higher-order terms and therefore reduce the state fidelity. In general, we can see a trade-off between state fidelity and generation probability. For weak squeezing values, the heralding probability increases with pump power,

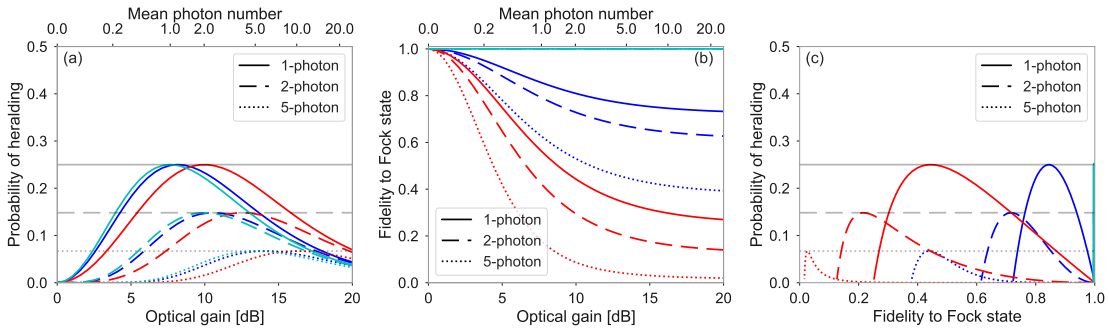

Figure 2.6 – Heralding probability (a) and fidelity to a Fock state (b) as functions of the optical gain for idler transmission values of 1.0 (cyan), 0.85 (blue), and 0.5 (red). Fundamental limits for the heralding probability are shown with grey horizontal lines. Heralding probability and fidelity plots can be combined as a parametric plot (c). See text for further details.

whereas the state fidelity is decreasing.

Figure 2.6 (c) combines heralding probability and state fidelity as a parametric plot. These combined plots are ideal for analyzing the performance of any probabilistic photon source and have been shown for the single-photon case in [50]. The optimal working point is (independent of the photon number) in the right top corner where a deterministic source with unit fidelity is situated. For single-mode sources (see next section for the multimode case) the heralding probability is limited due to the geometric distribution of a thermal state. In addition, losses will limit the accessible parameter range further.

2.3.3 Efficient modeling of multimode PDC

As a next step, we want to generalize our findings for multiple (spectral) modes. Unfortunately, this extension is not obvious because the detectors cannot distinguish individual frequency modes. Therefore, calculating the probability p_n of having n photons independent of the (spectral) mode is challenging. Previously this problem has been investigated with generating functions [93] or calculated analytically for two Schmidt modes [83]. To illustrate the underlying problem we can write the detection probability p_n as

$$p_n = \sum_{|\mathbf{i}|=n} p_{\mathbf{i}} \,. \tag{2.30}$$

The kth entry of the multi-index $\mathbf{i}$ defines the photon number in the kth spectral mode. Calculating Eq. 2.30 can be a demanding task as all permutations that lead to a total photon number of n need to be considered. For example, calculating the probability of detecting only three photons $n = 3$ occupying three modes $K = 3$ requires ten terms

$$p_n = p_{3,0,0} + p_{0,3,0} + p_{0,0,3} + p_{2,1,0} + p_{2,0,1} + p_{1,2,0} + p_{0,2,1} + p_{1,0,2} + p_{0,1,2} + p_{1,1,1} \,, \tag{2.31}$$

where for example $p_{2,1,0} = p_{n=2,k=1}p_{n=1,k=2}p_{n=0,k=3}$ with a probability $p_{n,k}$ of having n photons in the kth mode as given by Eq. 2.15. It can be directly seen that the number of terms that need to be considered grows exponentially in n and K.

In [84], we present a new approach to calculate the convoluted photon number probability p_n based on discrete phase-type distributions [94]. It requires that all spectral modes have the geometric distribution of a thermal state with a vacuum probability q_k. These vacuum probabilities are easy to calculate given a squeezing value r_k

$$q_k = \mathrm{sech}(r_k)^2 \,. \tag{2.32}$$

With the vacuum probabilities q_k and considering K_{max} spectral modes we can calculate the photon number probability p_n with

$$p_n(q) = \alpha M^{n+K_{\text{max}}-1} M_0 \,, \tag{2.33}$$

where the matrix M is defined by

$$M = \begin{bmatrix} 1-q_1 & q_1 & 0 & \dots & 0 \\ 0 & 1-q_2 & q_2 & \dots & 0 \\ 0 & 0 & 1-q_3 & \dots & 0 \\ \vdots & \vdots & \vdots & \ddots & \vdots \\ 0 & 0 & 0 & \dots & 1-q_{K_{\text{max}}} \end{bmatrix} , \tag{2.34}$$

with $\alpha = (1, 0, ..., 0)$ and $M_0 = (0, ..., 0, q_{K_{\text{max}}})^T$. For this new approach it is straight forward to calculate the photon number probability p_n as only matrix multiplications need to be carried out. With this new tool, we are now able to investigate the heralding process for the multimode case.

2.3.4 Parametric down-conversion limitations: multimode

We want to consider both figures of merit, the generation probability p_n and the state fidelity $\mathcal{F}$ to the desired Fock state, in the general multimode case as well. Without loss of generality, we will consider spectral modes as an example for multimode emission. We have already discussed that this problem is more demanding as the heralding detector cannot resolve the time-frequency modes of the SPDC state. Detecting n photons, therefore, produces a mixed state that can occupy a variety of different modes, even for the lossless case. As we have discussed in the previous section, we suggest a new method to compute the generation probability p_n (see Eq. 2.33). This very general approach can be simplified further if we assume a double Gaussian joint spectral intensity function (see Sec. 2.2.1). We have seen that for this case the squeezing value per Schmidt number is exponentially decreasing (see Eq. 2.22). Using the vacuum probability q_k for the kth Schmidt mode, we can calculate the heralding probability via

$$p(n) = \sum_{j=1}^{K_{\text{max}}} \frac{(-1)^j (1-q_j)^{n+K_{\text{max}}-1}}{\prod_{m\neq j} |q_j - q_m|} \cdot \prod_{i=1}^{K_{\text{max}}} q_i \,, \tag{2.35}$$

where K_{max} defines the largest Schmidt mode that is still considered, as we have shown in [84].

Investigating the fidelity is an even more challenging task. To start with, we will differentiate two different infidelities in this context. As already stated, in general we are interested in the state fidelity to a specific Fock state n in a single spectral mode (and vacuum in all other modes). It is advantageous to define the desired mode with n photons as the first Schmidt mode because any desired squeezing value in this mode can be reached with minimal pump power. However, measuring this fidelity can be hard as current single-photon detectors do not resolve time-frequency modes. Therefore we will also introduce the fidelity to a multimode photon number state (mmPNS) for this purpose. We define a mmPNS as a state with a specific photon number n that occupies an incoherent mixture of modes. In the following we want to specify both fidelities.

Firstly, we only consider losses in the heralding arm. We can calculate the state fidelity to a single-mode state with the probability of having n photons in the signal and idler mode $p_{k=1}(n,n)$ and vacuum in all other spectral modes for signal and idler $p_{k>1}(0,0)$.

$$\begin{aligned}\mathcal{F}(|n\rangle\langle n|_{k=1} \otimes |0\rangle\langle 0|_{k>1}, \rho_s) \\ = \frac{1}{p_n} p_{k=1}(n,n) p_{k>1}(0,0) \,.\end{aligned} \tag{2.36}$$

The heralding probability p_n defines the probability of having n photons independent of spectral properties and can be calculated with Eq. 2.35. If losses in the signal mode are also considered, more cases can lead to the desired photon number n in the first spectral mode. The full derivation can be found in the supplement of [84]. The final fidelity is given by

$$\begin{aligned}\mathcal{F}(|n\rangle\langle n|_{k=1} \otimes |0\rangle\langle 0|_{k>1}, \rho) \\ = \frac{1}{p_n} \sum_{i=0}^{n} p_{k=1}(n, n-i) p_{k>1}(0,i) \,,\end{aligned} \tag{2.37}$$

where all probabilities already incorporate losses. Likewise the fidelity for the mmPNS can be found

$$\mathcal{F}_{\text{mmPNS}}(\rho) = \sum_{\sum n_k = n} \mathcal{F}\left(\bigotimes |n_k\rangle\langle n_k|, \rho\right) \,, \tag{2.38}$$

which we will become important for comparing our findings to experimental data in the next section.

Similar to the single-mode case, the results of the previous equations are illustrated in Fig. 2.7. Different colors represent three different Schmidt numbers of 1.0, 1.5 and 2.0 (blue, green, yellow, respectively). The heralding probability actually increases with an increasing Schmidt number Fig. 2.7 (a). The reason behind this finding comes from the fact that the convolution of geometric distributions approaches a Poissonian distribution. Therefore, the maximum heralding efficiency in the limit of an infinite Schmidt number is given by [95]

$$p_{\text{max, multimode}}(n) = \frac{e^{-n} n^n}{n!} \,. \tag{2.39}$$

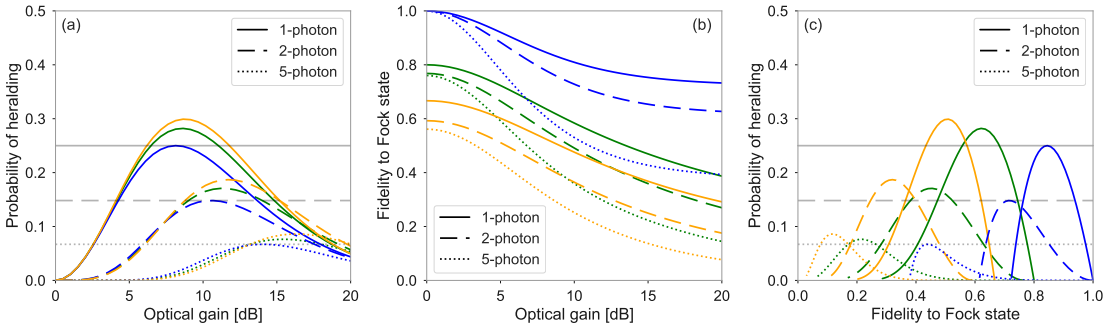

Figure 2.7 – Heralding probability (a) and fidelity to a Fock state in a single spectral mode (b) as a function of the optical gain for a Schmidt number of 1.0 (blue), 1.5 (green), and 2.0 (yellow). All curves are calculated for a heralding efficiency of 0.85. Heralding probability and fidelity to a Fock state plots can be combined as a parametric plot (c). See text for further details.

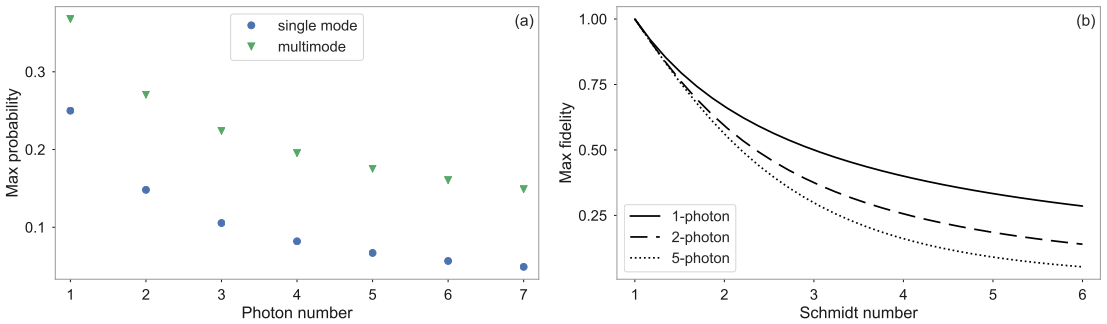

Figure 2.8 – (a) Absolute limits for the heralding probability as a function of the photon number for the single mode and multimode case. (b) Limits for the state fidelity as functions of the Schmidt number for three different photon-number states.

Although the effect of an increased heralding probability seems desirable, this effect is cumbersome for most applications. This becomes apparent if we additionally analyze the state fidelity to a single-mode Fock state. As shown in Fig. 2.7 (b) the state fidelity decreases with an increasing Schmidt number. In addition and in contrast to losses, an increased Schmidt number cannot be counteracted with a lower optical gain. Optimizing the SPDC state for single-mode emission (see Sec. 2.2.1) is therefore desirable for Fock state generation.

The absolute limits of heralding higher-order Fock states with SPDC are shown in Fig. 2.8. Due to the underlying distribution (geometric distribution for the single-mode case and Poisson for the multimode case) a maximum heralding efficiency can be calculated (see Fig. 2.8 (a)). The Schmidt number will limit the achievable state fidelity to the desired single-mode Fock state (Fig. 2.8 (b)).

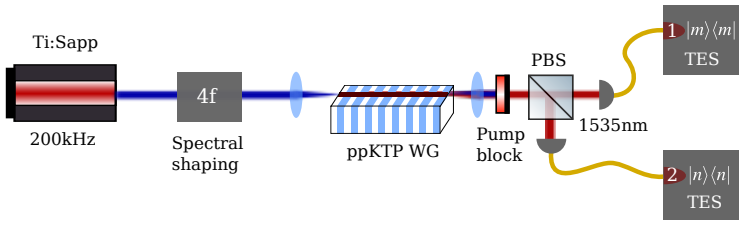

Figure 2.9 – Experimental setup for heralding higher-order Fock states. A two-mode squeezed vacuum state is split on a polarizing beam splitter (PBS). Both modes are detected with transition-edge sensors (TES). See text for further details.

2.3.5 Experimental setup

In order to compare our theoretical findings with experimental data, we recorded both modes of a two-mode squeezed vacuum state with transition-edge detectors (TES) [84]. These TES detectors as introduced in Sec. 3.2 offer intrinsic photon number resolution such that convolutional effects from multiplexing are not apparent. However, TES detectors cannot distinguish between the time-frequency modes of the SPDC state, as they have a constant frequency response function over the measurement spectrum. The two-mode squeezed vacuum state is generated inside a source-engineered periodically poled potassium titanyl phosphate (PPKTP) crystal via type-II SPDC. Single-mode emission around 1550 nm [61–63] and very high brightness [89] have been demonstrated for these waveguided sources. The crystal is pumped with a frequency shaped (4f-configuration) Ti:Sapph oscillator at 767.5 nm and a repetition rate of 200 kHz. For this experiment, a non-ideal pump spectrum was chosen in order to increase the Schmidt number and therefore amplify multimode effects. The setup can be seen in Fig. 2.9.

2.3.6 Results

The comparison between experimental data and multimode theory is shown in Fig. 2.10, where heralding probability and the fidelity to an mmPNS are investigated. In contrast to the previous sections, signal losses are considered as well to match the experimental data. The theoretical model can describe our experimental findings with high accuracy. For these plots only signal and idler losses and the effective Schmidt number are fitted to the experimental data. We estimate signal and idler efficiencies (Klyshko efficiency) of 0.64 and 0.59, respectively, as well as a Schmidt number of 1.61. The highest measured mean photon number corresponds to an initial squeezing value of 11.5 dB at the source. As expected for this multimode case, a heralding probability above 25% is measured.

Measuring the fidelity to a single mode Fock state is a very demanding task and would require a time-frequency mode selective measurement. This has been shown, for example, by using a local oscillator, which acts as a frequency selective filter (see Chap. 4). However, this approach poses additional constraints for the local oscillator generation, which often limits the available

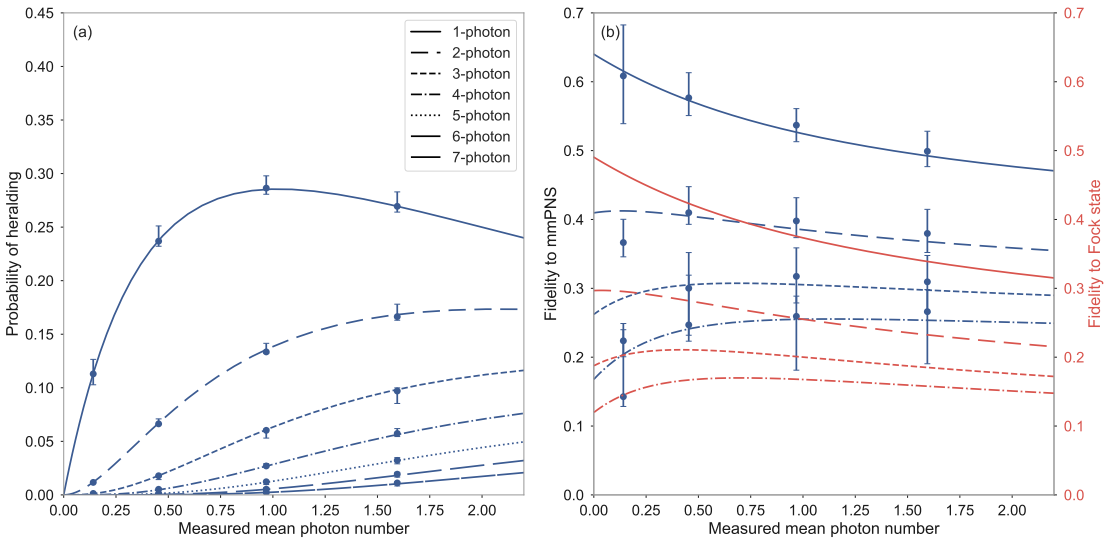

Figure 2.10 – Experimental data for the heralding probability (a) and state fidelity to an mmPNS state (b) as functions of the measured mean photon number. The fidelity to a single-mode Fock state is shown in red as a comparison. See text for further details.

pump power for the PDC process [88, 96]. Therefore, we measure the fidelity to a multimode photon number state, which is independent of the underlying mode structure. Nevertheless, the presented approach of fitting our multimode theory to the experimental data offers insights to the underlying mode structure. Therefore it is possible to gain information about the spectral mode-structure without mode-resolved detection. To be more specific, it is obviously not possible to determine the shape of an individual spectral mode without any reference, but the effective Schmidt number and, to some extent, the mode distribution can be extracted.

These results highlight the advantages of a single-pass SPDC configuration in combination with waveguides because low losses and high squeezing values can be reached simultaneously. Our new theoretical approach is still able to model these parameter regimes efficiently. An additional application for our theory can be found in Appendix B, where we investigate multimode measurements in the high gain regime. The presented theory, therefore, is a tool to evaluate the feasibility of new experiments that require Fock states. At the same time, this work also shows the need for new approaches [80, 81, 97] to generate high-quality higher-order Fock states.

2.4 PDC in the continuous variable picture

Up to now, we have considered PDC in the discrete variable (DV) picture. This means that we have always measured properties with a discrete outcome (in our case, photon numbers). In this section, we will consider a different class of observables instead, which have a continuous output spectrum (continuous variable (CV) measurements). To simplify our discussion, we will

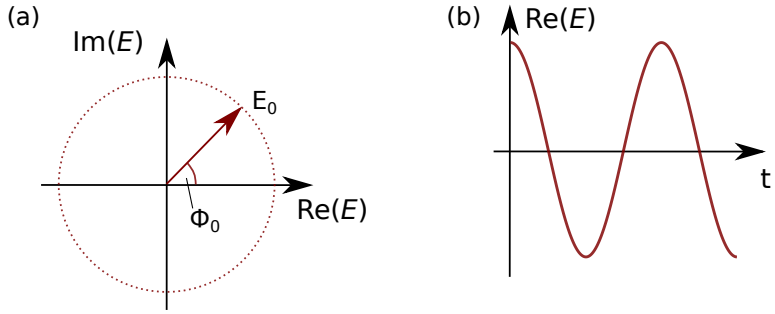

Figure 2.11 – The complex electric field with an amplitude E_0 is rotating with an angular frequency ω around the origin (a). The projection on the abscissa reveals the real part of the electric field (b).

restrict ourselves to the single-mode case. Both descriptions are equivalent, but, depending on the measurement and the application, one or the other point of view might be more favorable. Following the measurement, also representing the state is generally done on one or the other side. For a photon-number measurement, a description as a density matrix in the Fock basis is natural, whereas quadrature measurements can be better expressed in the phase-space picture (although we see in Chap. 4 that a link between these worlds can be beneficial). We want to motivate these phase-space functions in a simple form known as a phasor-diagram.

2.4.1 Phasor diagrams

Phasor diagrams can be very insightful to get an intuitive understanding of many quantum states and processes. To understand these diagrams, we will start again from the classical perspective where we can write a monochromatic electric field $E(t)$ as a complex number

$$E(t) = E_0 \exp(i\omega t + \Phi_0) \, . \tag{2.40}$$

The imaginary and the real part of the electric field $E(t)$ can be illustrated as projections of a rotating vector (see Fig. 2.11 (a)). These diagrams are called phasor diagrams [98]. The time-varying projection of the electric field vector on the abscissa can be seen in Fig. 2.11 (b). In the next step, we can quantize the electric field operator $\hat{E}$. Instead of using this operator directly, it is more common to define dimensionless quadrature operators $\hat{X}_1$ and $\hat{X}_2$

$$\begin{aligned} \hat{X}_1 &= \frac{1}{2}(\hat{a} + \hat{a}^\dagger) \\ \hat{X}_2 &= \frac{-i}{2}(\hat{a} - \hat{a}^\dagger) \, , \end{aligned} \tag{2.41}$$

which still have the same characteristics as the electric field operator. The quadrature operators do not commute ($[\hat{X}_1, \hat{X}_2] = i$), which limits the knowledge of both values according to the generalized Heisenberg uncertainty principle.

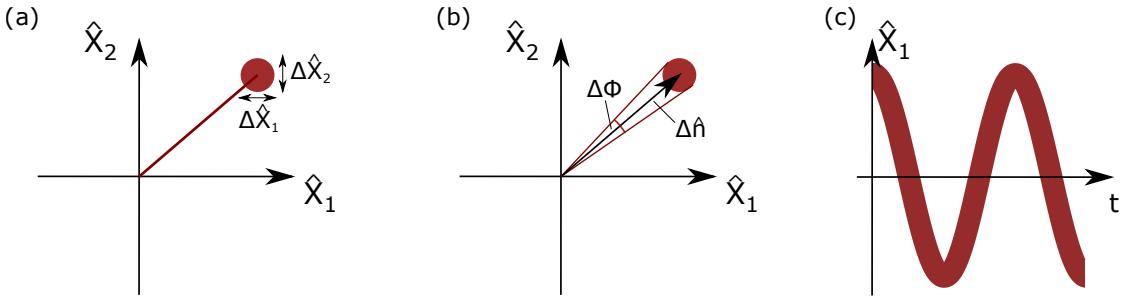

Figure 2.12 – Phasor diagram of a coherent state $|\alpha\rangle$ with a quadrature uncertainty $\Delta\hat{X}_1 = \Delta\hat{X}_2 = 1/2$ (a). The coherent state has an amplitude and phase uncertainty (Δn, $\Delta\Phi$ respectively), which is changing relative to the amplitude (b). Time dependence of the electric field in terms of $\hat{X}_1$ (c).

To see the impact of this finding in the phase space picture, we will investigate coherent states

$$|\alpha\rangle = \mathrm{e}^{\frac{-|\alpha|^2}{2}} \sum_{n=0}^{\infty} \frac{\alpha^n}{\sqrt{n!}} |n\rangle \ . \tag{2.42}$$

These states have the smallest equally-split uncertainty with respect to the quadrature operators

$$\sigma_{\hat{X}_1} = \sigma_{\hat{X}_2} = \frac{1}{2} \ , \tag{2.43}$$

with a quadrature standard deviation given by $\sigma_{\hat{X}} = \sqrt{\Delta\hat{X}} = \sqrt{\langle\hat{X}^2\rangle - \langle\hat{X}\rangle^2}$. The uncertainty is often indicated as a circle in the phasor diagrams (Fig. 2.12 (a)). Figure 2.12 (b) illustrates that these quadrature uncertainties also have an effect on the amplitude and phase uncertainty. However, these uncertainties change as a function of the mean photon number $\bar{n} = \langle\hat{n}\rangle = |\alpha|^2$. If we, for example, consider the photon number uncertainty σ_n relative to the mean photon number $\bar{n}$, we can see that the uncertainty is vanishing for large photon numbers

$$\frac{\sigma_n}{\bar{n}} = \frac{1}{|\alpha|} \ . \tag{2.44}$$

This is also the underlying reason why the discretized nature of the electric field is barely visible for bright states.

2.4.2 Generating squeezed states

In addition to the generation of Fock states, we can also use SPDC to produce squeezed states. We have already seen the phasor diagram of a coherent state in Fig. 2.12. With parametric down-conversion, it is possible to reduce the uncertainty along one quadrature axis at the cost of increasing the uncertainty in the orthogonal quadrature. If the PDC process is acting on the vacuum field, a single-mode squeezed vacuum field is generated (Fig. 2.13 (a)). In contrast to

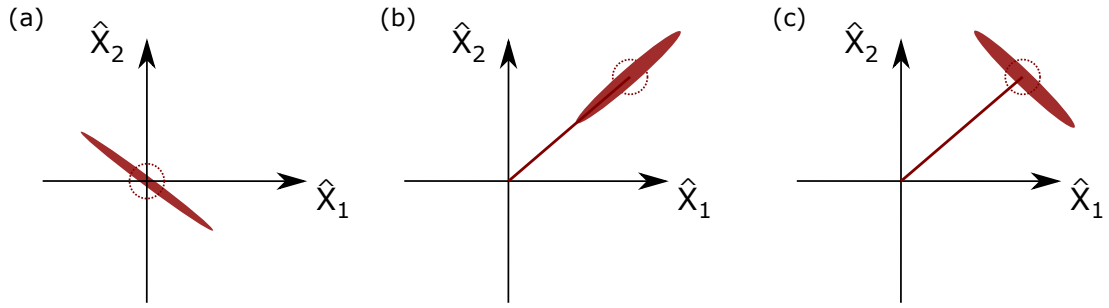

Figure 2.13 – Phasor diagrams of single-mode squeezed states. The squeezing operation can be applied on the vacuum field (a) or on a coherent state (b,c). Depending on the phase between the coherent state and the squeezing operation, we can distinguish phase squeezing (b) or amplitude squeezing (c). The coherent state uncertainty is indicated with a dashed circle.

our previous considerations, we can also apply PDC to a coherent state. These states are known as bright squeezed states, and the squeezing will have an additional phase with respect to the coherent state phase. If the squeezing is perpendicular or parallel to the amplitude vector, these states are called phase (Fig. 2.13 (b)) or amplitude (Fig. 2.13 (c)) squeezed states, respectively.

If we consider a type-II PDC process (or non-degenerate type-I), we will produce a two-mode squeezed state instead. Here the individual signal and idler modes (the second mode is traced out) show the increased noise level of a thermal state. No quantum correlations are visible as shown in Fig. 2.14 (a,b). However, if we consider joint measurements of the signal and the idler mode, we can uncover quantum correlations Fig. 2.14 (c). For this reason, we define superposition quadrature operators, which are given by the quadrature measurements in the signal $\hat{X}_s$ and idler $\hat{X}_i$ mode [31]

$$\begin{aligned}\hat{X}_{1,\text{super}} &= \frac{1}{\sqrt{2}}(\hat{X}_{1,i} + \hat{X}_{1,s}) \\ &= \frac{1}{2\sqrt{2}}(\hat{a}_i + \hat{a}_i^\dagger + \hat{a}_s + \hat{a}_s^\dagger)\,,\end{aligned} \tag{2.45}$$

and the second quadrature operator defined by $\hat{X}_{2,\text{super}} = \frac{1}{\sqrt{2}}(\hat{X}_{2,i} + \hat{X}_{2,s})$. We will come back to details of these phasor diagrams in Chap. 4.

Both single-mode squeezing and two-mode squeezing have a wide range of applications, especially in quantum sensing. A prime example where squeezing is readily used is gravitational wave detection [99]. Compared to the generation of other exotic quantum states, the generation of squeezing is rather simple and deterministic, and it can be shown that the phase sensitivity in lossy interferometers is optimal for squeezed states compared to all other states [100]. Nevertheless, squeezed states are loss sensitive and the additional work required to generate these states needs to be justified. In general, it can be said that squeezing can improve a lot of phase-sensitive measurements if classical optimizations (increasing optical power, reducing classical noise from

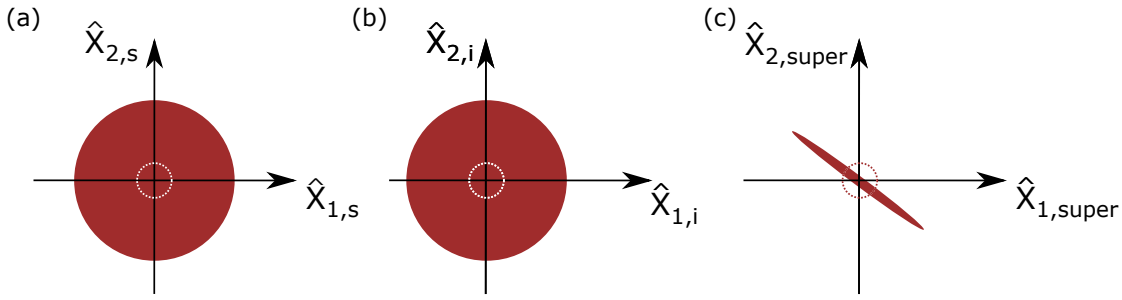

Figure 2.14 – Phasor diagrams of a two-mode squeezed state. The individual signal and idler modes on their own show an increased noised level compared to a coherent state (a,b), which is indicated with dashed circles. Correlations can only be seen if the quadrature values between both modes are measured jointly (c).

the laser) cannot give additional benefits. In this case, the achievable amount of squeezing often limits the measurement sensitivity. Therefore, it is desired to increase the effective nonlinearity as much as possible. In most cases either cavity systems or waveguided crystals are used to increase the pump power per interaction volume. As we have seen for the Focks state generation, in this thesis we will focus on the latter, which has been studied in detail in recent years [35, 47, 61, 63, 89]. We will use squeezed states in the context of quantum tomography in Chap. 4.

2.5 Conclusion

In this chapter, we have introduced the process of PDC and discussed how we can describe it from the DV and CV perspectives. As an example of the generation of large quantum states, we investigated the production of higher-order Fock states. Absolute limits for the generation probability and state fidelity were derived as a function of the heralded Fock state n and the degree of multimodeness quantified by the Schmidt number K. For typical squeezing values (below 7dB), we have a trade-off between state fidelity and heralding probability. In this range, increasing one parameter comes at the cost of reducing the other, while for higher squeezing values, both parameters are reduced. We compare our new theoretical model described in Sec. 2.3.3 with experimental data and show that this data can be modeled with very high accuracy. To achieve high heralding rates for the higher-order Fock states (up to $n = 7$) in a single-pass configuration, waveguided nonlinear materials are required. With this configuration we show inferred squeezing values above 11 dB. These achievements build the foundation for the next chapters, where we will use SPDC states as a resource.

CHAPTER 3

Photon-number detection

Contents

In general, a variety of detectors have been designed to uncover quantum properties of light. In this chapter, we will focus on photon-number measurements and demonstrate new detection methods towards the measurement of mesoscopic states.These measurements have discretized outcomes due to energy quantization, which is connected to the DV perspective. However, we can often rephrase the results to get insights into the CV perspective as well. Therefore this chapter is also a building block for further quantum state characterizations shown in Chap. 4.

3.1 Background

Before we can start to investigate the photon-number detection process, we will briefly discuss the meaning of measurements in quantum optics. As a next step, typical measurement imperfections, namely losses and single-photon detector properties, will be considered. Finally, we will have a look at the Mandel Q-parameter as a specific example to quantify non-classicality in the photon-number basis.

3.1.1 Measurements in quantum optics

Measurements in quantum optics do not fulfill the intuition from our 'classical' daily living. For example, in quantum mechanics, the measurement process will influence the measured quantity - in contrast to our experiences. Even Albert Einstein had some problems with this fact, which lead to his famous quote 'I like to think the moon is there even if I am not looking at it'. Despite the unintuitive nature of quantum measurements, this process was studied in detail in the last century and precisely formalized. Still, the exact transition between a quantum state wave function and a measurement outcome (measurement problem in quantum mechanics) remains an open research problem [101]. Following an axiomatic approach to quantum mechanics [28] a measurement can be identified with Hermitian (self-adjoint) operators performing a projection on the quantum state. The eigenvectors of these operators form an orthonormal basis. After the measurement, the state will be projected onto one of these eigenstates of the operator. To cover all cases, measurements have to be described in a more general way. To illustrate this, we will consider an example from quantum optics, which is a lossy measurement (more details about losses can be found in Sec. 3.1.2). In the case of no losses, the measurement projects on photon-number

states which form an orthogonal set. If losses are present, two different photon-number states can have the same detection outcome, which means that the measurements are not orthogonal anymore. Instead, the measurement can be described as a set of Hermitian positive semidefinite operators E_i which have to fulfill

$$\sum_{i=1}^{n} E_i = I \ . \tag{3.1}$$

This general measurement scheme is called positive-operator valued measure (POVM). According to Neumark's dilation theorem, a POVM can always be expressed as a projective measurement on a larger Hilbert space. For our example this means that the corresponding larger Hilbert space would also include all the photons that are lost (in an additional mode). From the experimental side, lost photons cannot be detected, which shows that a description with POVMs is required. At the same time, the informational content of the measurement is changed. This means, for example, that we cannot infer the initial photon number if we consider a single-shot measurement.

3.1.2 Measurement losses

Optical linear losses are the most important experimental imperfection for many quantum experiments. From a theoretical point of view, losses are equivalent to a random sampling of the optical field. This can be modeled by a propagation through a beam splitter with a transmission value of η and a vacuum field entering through the other input port. If we now consider n photons that pass through this beam splitter, we can calculate the probability of having n' photons remaining with a binomial distribution. In matrix notation, this can be expressed as

$$L_{n'n}(\eta) = \binom{n}{n'} \eta^{n'} (1-\eta)^{n-n'} \ . \tag{3.2}$$

For known photon-number probabilities p_n of a quantum state, the photon-number probabilities after losses $p_{n'}$ can be simply calculated via

$$p_{n'} = L_{n'n}(\eta) p_n \ . \tag{3.3}$$

If not stated otherwise, the Einstein summation convention is used. The POVM of a lossy photon-number measurement is therefore given by

$$\Pi_{n'} = L_{n'n}(\eta) \pi_n \ , \tag{3.4}$$

with $\pi_n = |n\rangle\langle n|$.

3.1.3 Single-photon detectors

To characterize our quantum state in the photon number basis, we require single-photon detectors that can resolve discretized energy levels. However, intrinsic photon-number resolution is a desired but seldom property of detectors at the single-photon level. One example where this

is fulfilled is a Transition-Edge Sensor (TES) [92]. Here a superconducting material is operated at the transition region between the superconducting and normal-conducting state, which causes an extremely high resistance change for a given temperature change. This dependence is, in fact, strong enough to measure the temperature increase due to an absorbed photon. As the transition region is linear within a specific range, n absorbed photons will change the resistance n times stronger than a single photon. The resistance change can then be transformed into a voltage signal using sophisticated electronic components. With this technique, efficiencies above 97% have been shown [92]. The drawback of TES detectors is that they need to be operated in the mK regime, which requires expensive and technically challenging cooling strategies.

Other detectors like Single-Photon Avalanche Detectors (SPADs) are easier to operate as they do not require cryogenic cooling. However, these detectors have a very limited detection efficiency of around 25% at the telecom wavelength of 1550 nm (minimal absorption wavelength for optical fibers, which is crucial for various applications). A very promising compromise is given by a rather new detector type, which is known as Superconducting Nanowire Single-Photon Detector (SNSPD). These detectors have a very thin and meandering nanowire, which is superconducting and biased with a constant current. If a photon is absorbed by this material, a local, normal conducting hotspot is generated, which produces a voltage peak. SNSPDs only require cryogenic cooling of around 1 K, which is much easier to achieve than the demanded temperature for TES detectors. The main advantage of SNSPDs is that very high efficiencies of 98% [102] in addition to other desired properties such as low dark-count rates [103], fast recovery time after a detection event [104], and very low intrinsic jitter values [105] are possible. For these reasons, SNSPDS are becoming a standard tool for quantum optical experiments and all experiments presented from this point on will be based on these detectors.

One major drawback of SPADs and SNSPDs is that they cannot distinguish individual photon numbers. Instead, they have a binary response, which means that they either 'no-click' if vacuum is present or they 'click' if at least one photon is present. Therefore these detectors are also often called 'click'-detectors. Their corresponding POVM elements are given by 'no-click': π_0 and 'click': $\pi_1 = 1 - \pi_0$. Measuring a photon number distribution is not possible with binary detectors. We discuss this problem in detail in Sec. 3.2.

3.1.4 Mandel Q-parameter

As a last step, we want to briefly discuss the 'quantum' aspect of photon number distributions. One could assume that measuring the discretized nature of the light field is already a proof for non-classicality. However, this result on its own could be described with a classical particle theory [70]. This shows that identifying non-classical light is a non-trivial task. Different methods have been developed that focus on a particular aspect of the quantum field and therefore reveal criteria that are sufficient but not necessary to identify non-classicality. Here we want to focus on the Mandel Q-parameter [106] as a specific example, which can be calculated by knowing the photon-number distribution of a quantum state. The Mandel Q-parameter is defined as

$$Q = \frac{(\Delta n)^2 - \langle n \rangle}{\langle n \rangle} \tag{3.5}$$

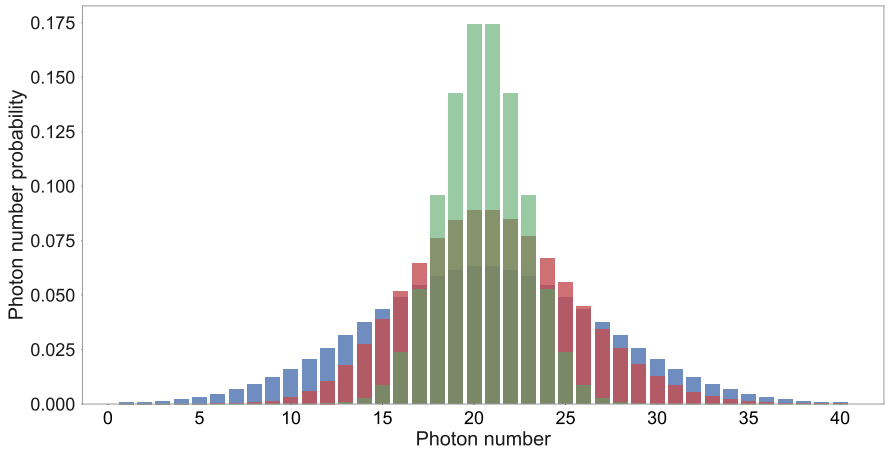

Figure 3.1 – Three photon-number probability distributions are plotted. Red: photon-number distribution of a coherent state which is given by a Poisson distribution. The mean and the variance of this distribution have the same value. Blue: super-Poissonian light where the variance is higher than the mean value. Green: sub-Poissonian light (non-classical) where the variance is smaller than the mean value.

where $\langle n \rangle$ is the mean photon number and $(\Delta n)^2 = \langle n^2 \rangle - \langle n \rangle^2$ is the photon-number variance. Fig. 3.1 shows three different photon-number distributions. One of the most common distributions is known as a coherent state (red) which has a Poissonian distribution

$$p_{\text{coh}}(n) = e^{-|\alpha|^2} \frac{|\alpha|^{2n}}{n!} \,. \tag{3.6}$$

For example, the photon-number distribution produced by a laser is often a coherent state. The Mandel Q-parameter for a coherent state is 0 as mean and variance are equal. Secondly, if an incoherent mixture of coherent states is present, the variance of the photon-number distribution will be larger than the mean (blue), and the Mandel Q-parameter is $Q > 0$. Thirdly, the interesting case for $Q < 0$ describes a state that has a photon-number variance that is smaller than its mean photon number. This is a sufficient criterion for having non-classicality. The extreme case is given by photon-number states with $Q = -1$, which are also known as Fock states. These states do not have any uncertainty in the photon number. As typical for many non-classicality criteria, losses have a strong effect on this value. For example, a photon-number state after loss will tend towards a Poissonian distribution.

This concludes our discussion of some basic properties required for photon-number measurements. We will now focus on the problem of measuring photon-number distributions with binary detectors.

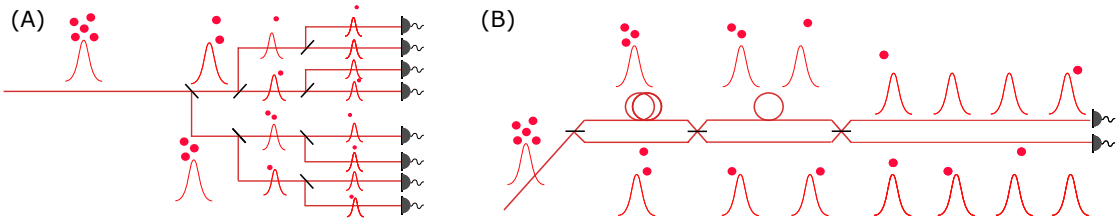

Figure 3.2 – Two examples of the multiplexing concept. In both cases an incoming light field with five photons is characterized. After each beam splitter (black lines) one possible splitting case of the five photon state is shown. (a) Spatial multiplexing: The incoming light beam is divided by seven beam splitters into eight spatial modes which are then detected by eight detectors. (b) Temporal multiplexing: The incoming light beam is divided at a beam splitter. Then one mode is delayed with a fiber delay line before both modes are combined at the next beam splitter. With this method an incoming pulse is split into two spatial modes with four time bins each and only two detectors are required for the detection.

3.2 Time-multiplexed detection for large input states

We have seen that binary detectors, especially SNSPDs, offer many advantages but cannot resolve individual photon numbers. Nevertheless, photon-number resolution is a necessary property for many quantum characterization methods, which led to the development of multiplexing [20–25]. The idea is quite simple: an incoming light field is split on multiple beam splitters into m modes. If this number is large compared to the maximal photon number n_{max} in the state, the probability that two photons are in the same mode is small. These modes can now be measured with binary detectors, and the number of 'clicks' is a good approximation of the photon number as the probability of for higher photon number contributions is small. To be more specific, the action of multiplexing is often expressed as a convolution matrix C_{kn} that maps the probability of having n photons to k clicks. This matrix is given by (e.g. [107])

$$C_{kn} = \binom{m}{k} \frac{k!}{m^n} S(k,n) \,, \tag{3.7}$$

where S is the Sterling number of second kind. Multiplexing can be implemented in different physical systems. Fig. 3.2 illustrates how multiplexing can be achieved in the spatial or in the temporal domain (cf. [108, 109]). If we compare the effect on an increasing number of output modes, we can see a big difference between these approaches: While the number of detectors increases with the output mode size for spatial multiplexing, it stays constant for temporal multiplexing. However, time-multiplexing detection (TMD) requires pulsed input to identify individual output modes. In this thesis, this assumption is fulfilled, as we will always consider pulsed states.

Previously up to eight-bin TMDs have been demonstrated (e.g. [109]). In this section, we

want to investigate the detection of large quantum states and demonstrate new TMD units. A naive approach would suggest that larger TMDs are always beneficial for detecting an unknown quantum state. If more bins are available, the measured click-distribution approximates the actual photon-number distribution more precisely. However, this simple consideration neglects the effects of optical losses, which also increase for an increasing number of modes. Therefore we can find a trade-off between available bin size and loss value. This effect has been studied in detail in [110] and an optimal bin number of < 256 was derived. However, it is important to note that the actual optimum depends on the specific measurement. Here, single-shot experiments (a measurement for a single input state is evaluated) and ensemble measurements (a measurement for many identical input states) have to be distinguished. The optimal bin number < 256 was derived for a single-shot configuration and a specific figure of merit (overlap of a Fock state before and after TMD). In general, the optimal bin number can be much higher than this value. For example, we can consider a recently demonstrated approach to characterize a PDC process with correlation measurements (moment generating functions) [111], which is loss robust. In this scenario, larger TMDs can uncover non-classicality due to higher correlation functions, whereas smaller TMDs would not be able to achieve this goal. Therefore we will discuss properties of TMDs in this section and analyze how large TMDs can be designed. Additionally, we demonstrate a new, highly efficient 128-bin TMD with two input modes that is able to detect large quantum states.

3.2.1 Designing TMDs

The most important design rule is that the TMD must be tailored to the final single-photon detector. All design parameters will depend on the specifications of these detectors. In this subsection, we will focus on SNSPDs; nevertheless, other single-photon detectors such as SPADs can be used as well. One of the most important specifications is the dead time of the detector (time after a detection event before the detector is able to detect a photon again with full efficiency). The detector dead time defines the minimal spacing between the individual time bins. To date, typical SNSPDs have dead times in the tens of ns range, which makes free space TMDs unreasonable. For this reason, we will only discuss fiber-based TMDs here. We will investigate the critical single-photon detector properties and implications for the TMD.

Polarization
SNSPD property: Typical SNSPDs are polarization-dependent due to their specific geometry.
TMD: The TMD should be built from polarization maintaining fiber for maximal detection efficiency. Otherwise, the polarization can be different for the individual time bins, which results in a bin-dependent efficiency. Note: For polarization maintaining fiber, the input light must be inserted in one of the two main axes because the relative phase between these polarization axes is not fixed for polarization maintaining fiber.

Dead time
SNSPD property: After a detection event, the detector needs some time before it can detect the next photon. This effect is known as detector dead time.

	2x2 splitter design	4x4 splitter design
Beam splitter loss	< 0.1 dB	< 0.25 dB
Number of beam splitters	7	4
Fiber	7	4
Required fiber length	20 m, 40 m, 80 m, 160 m, 320 m, 640 m, 1280 m	20 m, 40 m, 60 m, 80 m, 160 m, 240 m, 320 m, 640 m, 960 m
Expected loss	1.34 dB	1.48 dB
Required detectors	2	4

Table 3.1 – Comparison of a 2x2 and 4x4 TMD design.

TMD: The detector dead time defines the minimal spacing between two time bins.

Timing jitter and dark counts
SNSPD property: The single-photon detector, in combination with the readout electronics, will have a specific timing jitter. We will assume that the time duration of the optical state is much shorter than the timing jitter. In addition, the single-photon detector will have a dark count rate often specified in counts/s.
TMD: The detection jitter will define the width of the individual detection time bins. In combination with the detector dark count rate, this defines the noise floor of the TMD measurement and, therefore, the lower limit of the TMD dynamic range.

Dispersion
TMD: Dispersion is a fiber property that can in principle require additional bin time-bin separation (see [110]). For typical specifications (> 100 fs pulse duration, < 100 ns dead time and < 256 time-bins) this effect can be neglected with respect to the detector dead time. However, as shown in Sec. 3.2.3 this effect can significantly broaden the detection windows and therefore influence the detection noise floor.

Finally, the fiber TMD can be arranged in different geometries. The typical design is based on 2x2 fiber beam splitters (see Fig. 3.2 (b)) with straight connections or fiber delay lines in between. The fiber delays have to be chosen in such a way that each propagation path has a unique delay (which are separated at least by the detector dead time τ). The jth delay should have a length $\tau 2^j$. For very large TMDs (> 256 bins), it can be beneficial to use a different geometry, for example, based on 4x4 beam splitters to avoid effects from fiber dispersion and fiber loss. For this design, the required fiber length is shorter, but the loss per beam splitter is higher due to fabrication process.
For our specified goal of a 128-bin TMD, a 2x2 beam splitter design is still optimal as shown in Table 3.1.

3.2.2 Assembly of a 128-bin TMD

As discussed in the last section, we have designed a 128-bin TMD that consists of seven 2x2 beam splitters and fiber delay lines (20 m, 40 m, 80 m, 160 m, 320 m, 640 m and 1280 m). To minimize coupling losses between the individual components, a Fujikura polarization aligning fusion splicer was used. This device is able to give an approximation for the splice loss through a CCD image of the splice connection. All splices had an estimated loss below 0.01 dB. Special care was taken to design a compact TMD that can be moved between labs. The final TMD is shown in the Appendix in Fig. F.1.

3.2.3 Characterization

The most important parameter for a TMD is the device efficiency η. If sub-Poissonian light is investigated, losses will broaden the photon-number distribution (towards a Poisson distribution) and therefore diminish the non-classicality. Although this effect can be partially overcome using sophisticated analysis tools [112], practical restrictions such as noise counts and time-dependent fluctuations during the measurement will limit these approaches. Therefore it is always desirable to aim for highly efficient TMDs. In addition, we will also characterize the bin dependence of our TMD. A non-uniform bin click probability p_j can fake sub-Poissonian distributions and therefore should be included in the analysis as a systematic error. As an example to illustrate this problem, consider the extreme case where only one of the 128-bins is functioning. For bright (classical or not) light states, the recorded click probability c_k (probability of k simultaneous clicks) will always show one click, which is a highly non-classical distribution. Therefore considering the click probability is an important factor.

Efficiency characterization:
We characterized the device efficiency with a continuous-wave laser at the desired wavelength of 1550 nm. For the first input, an average transmission losses of 0.65 dB (86.1% transmission efficiency) was found whereas the second input had an average loss of 0.90 dB (81.3% transmission efficiency). The difference between the two input ports can be explained by an additional 1.3 km of polarization maintaining fiber after the second input port. This fiber is needed to separate the exiting pulses from the first and second input port in time. The overall efficiency is better than expected as the (maximal) loss specifications for the individual TMD components (fiber beam splitters and fiber delay lines) was calculated to be 1.34 dB (74% efficiency).

Time-bin characterization:
The bin click probability p_j was characterized with a pulsed input laser with a repetition rate of 50 kHz and a pulse length of 200 fs. The timing histogram of the exiting pulse train is shown in Fig. 3.3 (a). As expected, it can be seen that dispersion broadens the pulses, which naively results in the appearance of a strongly decreasing bin click probability. In the next step, the individual bins are integrated over the time windows to calculate the bin click probability. The bin dependent click number for the first input mode is shown in Fig. 3.3 (b). The click number is slightly decreasing with increasing bin number due to the additional fiber delay loss. Still a high uniformity with a standard deviation of 7% is found. This uniformity is an important factor for quantum state characterizations, as we discuss in Sec. 3.5.3.

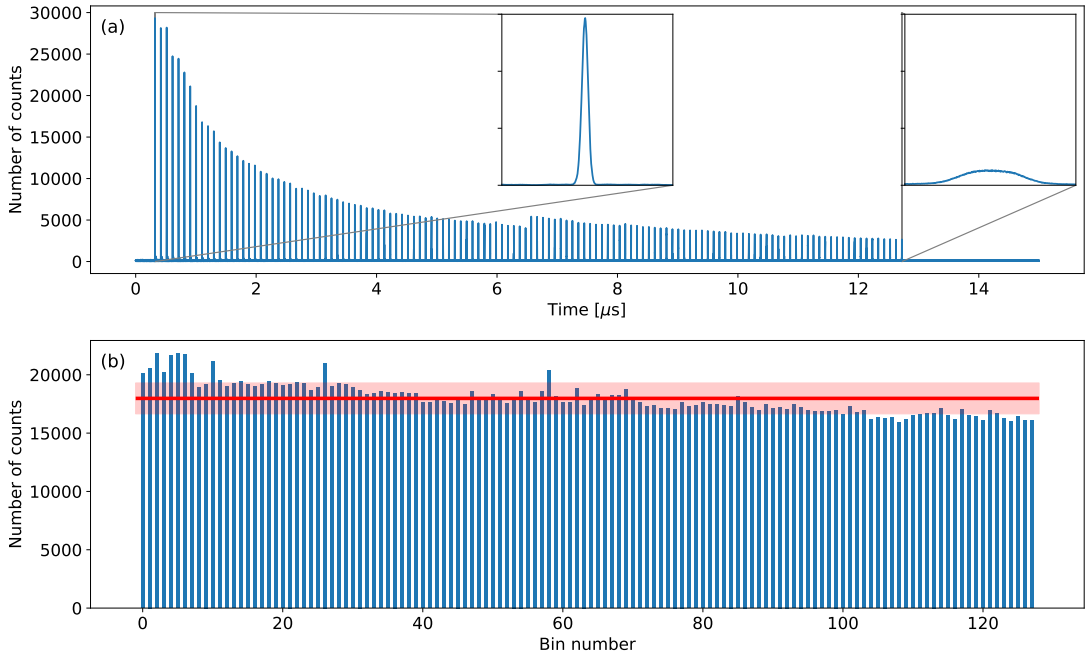

Figure 3.3 – Timing histogram of the first output (a). A jump from bin 64 to 65 can be seen, that marks the end of input one and the beginning of input two (slightly higher input power on input two compared to input one). The pulse amplitude decreases due to dispersive broadening of the pulses, as shown in detail in the insets that magnify the first and the last time bin. (b) Integrated click number for the first input mode of the TMD (bins 1 to 64 from output one and two). The red line shows the mean number of counts and the standard deviation. An overall high uniformity in the bins can be seen with a slightly decreasing bin height due to fiber losses.

With these characterizations, we have shown that our device is able to investigate quantum states. The presented unit is the largest TMD demonstrated so far and is a building block for measuring large quantum states, as shown in [89]. Our work proves that time-multiplexing is a low-cost alternative to investigate large quantum states that were previously investigated with demanding (in terms of costs and handling) TES detectors.We will now discuss new readout strategies that are required to evaluate large TMD units before we investigate quantum correlations with the 2x128-bin TMD.

3.3 Evaluating time-multiplexed detection data

Large detection schemes, as shown in the previous section, directly challenge existing readout methods. For example, our new TMD unit can generate $2^{256} \approx 10^{77}$ individual click patterns,

which is approaching the estimated number of atoms in the universe. This shows that it is crucial to extract, process and store the relevant information. In the context of our TMD unit, we have to address the two questions, which contain the required information: 'How many times has a bin clicked?' (bin probability) and 'Which bins have clicked simultaneously?' (coincidences). A variety of electrical devices can be used to analyze the voltage response from the single-photon detector. Here we want to discuss the methods that were used and newly developed to analyze TMD data.

3.3.1 Oscilloscope

The most important advantage of an oscilloscope is that it is generally available in laboratories. However, in order to use the full advantage of e.g. SNSPDs with respect to their timing jitter (few ps) it is important to use oscilloscopes with a very high input bandwidth ($> 100\,\mathrm{GHz}$) which are not that common due to their high cost. Another disadvantage is that standard oscilloscopes can only record data for a specific time interval (measurement trace). After the measurement, the data needs to be processed and stored, which prevents continuous data recording (without any timing gaps). Last but not least, an oscilloscope has vertical resolution (can measure different voltage values). This is an advantage for many debugging scenarios but causes a significant data overhead if only the arriving time of a photon is of interest. For these reasons, oscilloscopes are great for debugging, but time taggers are, generally speaking, the better choice to record data from binary detectors.

3.3.2 Time tagger

The concept of a time tagger is that a timestamp is stored each time a specific voltage threshold on an incoming electric signal is surpassed. Inside every time tagger, a key component known as a Time-to-Digital Converter (TDC) is used to accomplish this task. The working principle is quite simple; a high-speed internal counter is increased every time step (state of the art: 1 ps). Each time a signal reaches the TDC, the counter value is stored as a raw timestamp (one time tag). As many operations must be carried out simultaneously, Field Programmable Gate Arrays (FPGAs) are used for this task and the additional processing. The timestamps contain all required information to answer our two initial problems of bin probabilities and coincidences. Two basic strategies, which were developed in the context of this thesis, will be compared. In the beginning, a way to analyze TDC data in post-processing using C++ is shown. Then we focus on a more recent approach that enables a broad range of TDC data evaluation on the fly.

For work presented in this thesis, two commercial time taggers were used (TTM 8000 from Austrian Institute of Technology GmbH and TimeTagger Ultra from Swabian Instruments). The manufacturers offer several basic functions e.g. shifting channels, applying dead times, etc. The following sections describe how these functions can be extended to analyze TMD data.

3.3.3 Analyzing raw timestamps

A common way to analyze TMD data is to save all timestamps to a hard drive without any further processing. At a later point, the raw data is loaded and processed further. This method offers a

lot of flexibility as analyzing parameters such as an artificial dead time can be changed after the measurement. However, it is not possible to analyze the data instantaneously, which might be desired for aligning the experiment. Besides, a substantial amount of data can be produced with these measurements (GByte/min) requiring careful data analysis code optimization. Although all data acquisition code used in this thesis was written in the Python programming language, this code in the standard form is not fast enough to analyze large data sets in a reasonable time. Therefore C++ was chosen to analyze large raw data files, which are then passed to Python code for further processing.

While handling these large file sizes, it is important to read in large data blocks. If data is loaded time tag after time tag from a hard drive, this process is often inefficient as executing this command produces an additional timing overhead. On the other hand, data blocks cannot be too large as they need to be stored in the RAM for further processing. Analyzing data blocks comes with some additional difficulties. Often timestamps will depend on each other e.g. a time tag should be discarded if it arrives within the detector dead time. Therefore the information about these cases has to be passed from one block to the next. Both time tagger companies provide basic functions to solve these problems. In this thesis, functions for introducing global delays per channel, applying artificial dead times and evaluating multi-coincidences were used. In addition to these basic functions, the analysis of time tags from a multiplexed detector was implemented in C++ (see Appendix C).

3.3.4 Analyzing TDC data on the fly

Instantaneous timestamp analysis offers many advantages. For example, specific measurements can be directly graphically visualized to optimize the parameters in an experiment and not all raw timestamps need to be stored. Two main approaches to handle the data are possible. Either the data is directly processed on the FPGA or the raw timestamps are sent to a connected computer where the analysis is carried out. Direct FPGA processing offers the advantage of calculating many operations simultaneously due to the intrinsic parallel architecture of an FPGA. However, adapting the FPGA code to new tasks is rather complicated and the manufactures of FPGAs typically do not offer user-specific modifications. In contrast, computer-based evaluation is much more flexible but comes with the disadvantage of requiring a considerable amount of computational power. If complex functions have to be computed based on timestamps with a high repetition rate, the computational power might not be sufficient. This means that whenever timestamps are analyzed on a computer, special care should be taken that no events are lost. Swabian Instruments offers many basic functions for timestamp analysis, which can be easily controlled and adjusted using a high-level programming language like Python, which would be otherwise too slow to handle calculations itself. An essential concept for this kind of data analysis is the virtual channel. Here a time tag stream from a physical channel is copied and shifted in time with a constant offset. This process can be repeated as long as the computer processor is still able to handle all time tags from all generated channels. Further measurement classes handle virtual channels and physical channels in the same way.

In the following, a new method is explained showing how TMD data can be analyzed in a very efficient way. This method is based on the basic functions provided by Swabian Instruments. As

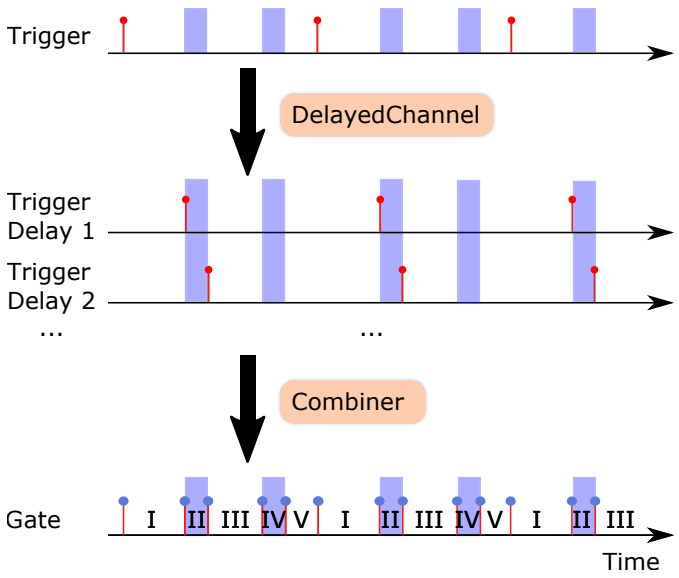

Figure 3.4 – Illustration for the `get_gate` function. A trigger signal from the time tagger is used to generate multiple delayed copies using the inbuilt function `DelayedChannel`. The trigger is delayed such that the new positions encircle the time positions of the TMD bins (marked in blue). Then the `gate` channel is generated using the inbuilt `Combiner`-function.

an example, the analysis of a 2-bin TMD is shown.

Step 1 - Generating a gate-signal:
As a first step, a virtual channel called `gate` has to be generated. This channel will mark the positions of the time bins for further processing steps. Fig. 3.4 illustrates the two stages that are needed to generate the `gate` channel. The initial trigger signal (physical channel that connects the optical experiment with the time tagger) is used to generate multiple delayed copies. This can be realized with the Swabian Instruments `DelayedChannel` function. For an n-bin TMD, $2n$ delayed copies have to be generated in order to mark the beginning and the end of all time bins. Now the Swabian Instruments `Combiner` function is used to merge all created channels. The resulting channel is called the `gate` channel and separates the timeline into $2n+1$ areas (labeled with Roman numerals in Fig. 3.4). An example function to generate the `gate` signal can be found in App. C.1. It is important that the complexity of this problem only scales linearly in the number of bin n.

Step 2 - Measuring clicks:
As a second step, the Swabian Instruments function `CountBetweenMarkers` is called to measure how many clicks have occurred in different areas. The function is set such that it will generate a list with $(2n+1)\cdot M$ entries, where M defines the number of measurements (=number of recorded trigger events). Additionally, a detector channel and the `gate` channel are passed to

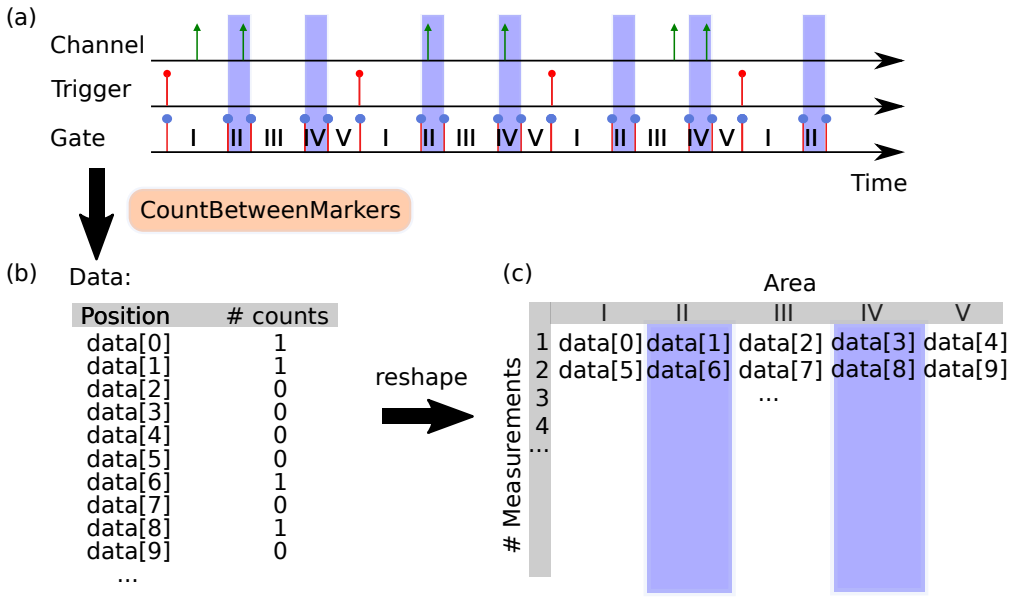

Figure 3.5 – This figure illustrates how the Swabian Instruments `CountBetweenMarkers` function is used to measure TMD data. A Detector channel (green) and the gate channel (a) are used to generate a data list (b). This list is reshaped to an array for further processing (c). Time bins from the TMD are marked in blue. See text for further details.

the function. The working principle of `CountBetweenMarkers` is as follows: With the first event from the gate channel, an internal counter is started. Each time an event from a detector channel is detected, the counter is increased. If a new event from the `gate` channel is recorded, the function stores the value of the counter in the output data list, the internal counter is reset, and the function moves to the next entry of the data output list (for further details see [113]). This behavior is illustrated in Fig. 3.5 (a) and (b). The resulting data list contains the information of how many events have occurred in each individual area.

Step 3 - Reshaping and analyzing the data:
In the last step, the data list from `CountBetweenMarkers` is reshaped into a $(2n+1, M)$-dimensional matrix (see Fig. 3.5 (c)). Each row in this matrix represents now a new measurement, which starts with a trigger signal from the experiment and consists of $2n+1$ time areas. Each column specifies one of the time areas. We are interested in all even columns as they contain the information of the TMD time bins (blue areas in Fig. 3.5). Now two different summations can be carried out. If we sum over all rows, we are left with $2n+1$ entries containing the information of which areas have clicked how many times (area-click frequency). For standard TMDs, this information does not give any insights into the quantum state as all bins have the same click probability. Only for asymmetric bin-click probabilities, this property should be considered further (cf. Sec. 3.5). In contrast, if we sum over all areas (columns), the resulting array of length M contains the information of how many bins have clicked each measurement

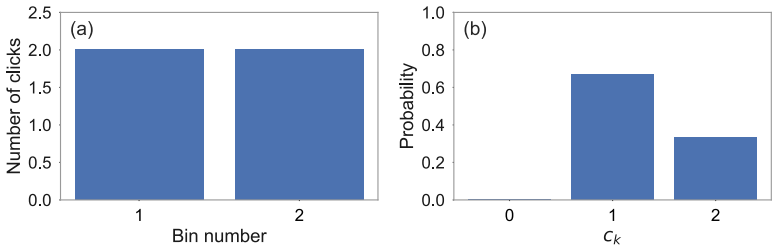

Figure 3.6 – Example evaluation for the clicks shown in Fig. 3.5. The summation over all rows of the output matrix (Fig. 3.5 (c)) gives the bin-click frequency (a). From the summation over all columns the coincidence probability c_k of having k coincidences per measurement can be calculated (b). See text for further details.

run. From this list, we can calculate the coincidence probability c_k of having k simultaneous clicks per measurement. This property is crucial for many non-classicality measures (e.g. [114]) as it is directly linked to the photon-number probability of the input state (see Sec. 3.2).

As an example evaluation, we will consider the case shown in Fig. 3.5 (a). After the first trigger, an event occurred in the first TMD time-bin. After the second trigger (measurement two), both TMD bins had recorded an event, and for the third trigger, only the last bin was occupied. This means that both TMD time-bins saw two events (shown in Fig.3.6 (a)). For two measurements, only one of the two bins "clicked", while for one measurement both of them were occupied. This results in a coincidence probability c_k, as shown in Fig. 3.6 (b).

Simulating p_j and c_k requires considerably different approaches as well. For calculating the bin-click probability p_j each bin can be treated individually. However, if we calculate the coincidence probability c_k, conditional probabilities need to be considered. As an example, we can assume a single photon at the input. If the first bin has detected an event, this will change the probability of the second bin (which now is zero as only one photon can be detected). For arbitrary bin-click probabilities, this is a computationally demanding task.

From the experimental side, special care should be taken to ensure that the detection dead time is larger than the TMD time window (blue regions). Otherwise, measured counts will be affected by additional noise counts. At the same time, the detection dead time should be shorter than the time window separation. If this is not the case, the bin efficiency will depend on previous measurement results, which can strongly influence non-classicality measures.

The same analysis process can be generalized for multimode inputs (e.g. both modes from a two-mode squeezed vacuum state into two separate TMDs). Here for each trigger event, the number of clicks per mode is recorded. All relevant information is then stored in a $c_{k,j}$ matrix where the number of simultaneous clicks in the first mode k and the second mode j are stored.

The final $c_{k,j}$ matrix can be calculated in both ways, either by analyzing the raw timestamps after the measurement or using the presented approach that enables instantaneous analysis. The analysis of large TMDs (>60 bins) is preferably done after the measurement as the requirements for the computer CPU and RAM become demanding.

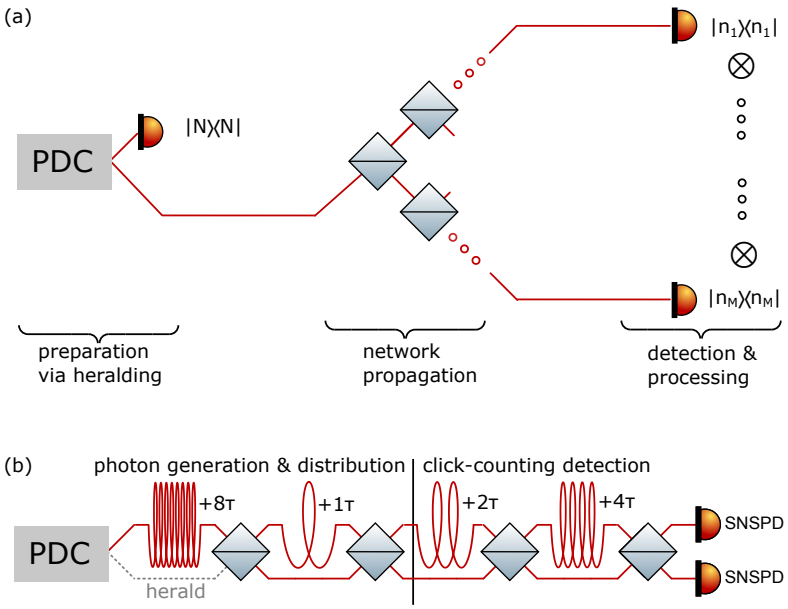

Figure 3.7 – Benchmark protocol in the spatial (a) and temporal (b) domain. Three steps can be seen: The generation of an N-photon state by heralding a PDC state. A propagation step, where the photons are spread over M modes and, finally, the detection with photon-number-resolving detectors (ideal) or D detection bins. For the temporal case we can combine these steps. We will use the first section (before vertical line) of our TMD for distributing our photon-number state and the second part for the detection. Please note: the shown temporal case is a simplification with $MD = 16$. For our experimental realization we will use a much larger TMD with $MD = 128$.

3.4 Quantum correlations in high-dimensional systems

In this section, we want to combine our newly developed 2x128-bin TMD with our readout schemes, discussed in the previous section, to investigate quantum correlations in large photonic systems. Currently, various physical systems are under investigation to provide a scalable platform for quantum algorithms [115–119]. In general, these platforms require very complex forms of quantum entanglement [120–127]. However, it has recently been shown that non-classicality can be regarded as an equally valuable resource [128].

Photonic systems have gained an increasing interest in this context over recent years because highly complex quantum systems can be designed by spreading many photons over many modes [129–135]. One of the most well-known examples in this context is boson sampling, where several indicators for quantum enhancements have been developed [136–141].

Here, we will present a new benchmark protocol to investigate large-scale photonic systems. In our theory, we analyze the three steps of quantum state generation, distribution, and detection jointly, in contrast to previous works.

3.4.1 Measurement scheme and theoretical considerations

To investigate large photonic systems with our TMD unit, we will theoretically split the TMD into two sections. The first section will be used to spread a PDC state over M modes, while the second part is used for the detection with D time bins. Figure 3.7 shows the schematic setup with its spatial analog.

If we herald an N-photon state with our setup and distribute it over M modes, we can write the resulting state as

$$|\Psi_{N,M}\rangle = \sum_{\substack{n_1,\dots,n_M\in\mathbb{N}\\ n_1+\dots+n_M=N}} \left(\frac{1}{M^N}\frac{N!}{n_1!\dots n_M!}\right)^{1/2} |n_1,\dots,n_M\rangle \ , \tag{3.8}$$

being highly entangled. By measuring this state with photon-number resolution, we can calculate the correlation functions

$$\begin{aligned} G^{(m_1,\dots,m_M)} &= \langle : \hat{n}_1^{m_1}\dots\hat{n}_M^{m_M} : \rangle \\ &= \frac{1}{M^{m_1+\dots+m_M}}\frac{N!}{(N-[m_1+\dots+m_M])!} \ . \end{aligned} \tag{3.9}$$

As a next step we want to quantify non-classicality in a single mode or a subset of $K < M$ output modes. Here, we have to consider our binary detectors at the TMD output as an experimental imperfection. To account for this, click counting techniques were derived [142]. We will use the matrix of moments that can be calculated from the measurement outcome to investigate K-mode non-classicality [143]

$$\Gamma_K = \left[G^{(m_1+m_1',\dots,m_K+m_K',0,\dots,0)}\right]_{(m_1,\dots,m_K),(m_1',\dots,m_K')} \ , \tag{3.10}$$

with the multi-index $\mathbf{m}$ and $\mathbf{m}'$ defining the rows and columns, respectively.

Finally, we want to discuss how we can define non-classicality with this approach. If we have classically correlated light in K modes, we have a corresponding positive-semidefinite matrix of moments $\Gamma_K \geq 0$. This means that we can uncover non-classicality if the minimal eigenvalue is negative. In order to calculate these eigenvalues, we can use the symmetry of the output (exiting time-bins can be swapped)[1]. Otherwise, calculating eigenvalues without this approach is not feasible (matrix of moments has the size $10^{19} \times 10^{19}$).

3.4.2 Experimental setup

The experimental setup is shown in Fig. 3.8. A Ti:Sapph laser is directly coupled to a periodically poled KTP waveguide after pulse picking with an electro-optic modulator (50 kHz). No spectral filtering is employed for the pump, as the measurement is independent of the spectral mode structure. Inside the waveguide a (spectrally multimode) two-mode squeezed state is gen-

[1] We can take the bin-probability variation, shown in Fig. 3.3, to calculate a systematic error connected with this approach.

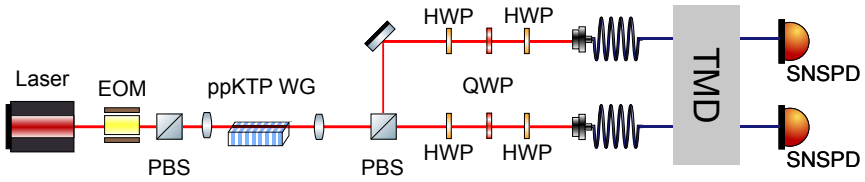

Figure 3.8 – A Ti:Sapph laser is pulse picked with an electro-optic modulator (EOM) and used for pumping a PDC type-II process in a periodically poled KTP waveguide (ppKTP WG). Signal and idler beams are split on a polarizing beam splitter (PBS) and polarization optimized with half-wave plates (HWP) and quarter-wave plates (QWP) before coupling to our TMD. The exiting modes are measured with two SNSPDs.

erated. Signal and idler are spatially separated with a polarizing beam splitter and coupled to our previously described 2x128-bin TMD unit. Both TMD output modes are measured with SNSPDs with a dead time of 60 ns (TMD time-bin separation is 100 ns). The SNSPD response is measured with a time tagger and stored for the additional analysis.

One important result from our TMD characterization is that time-bins can experience huge dispersive broadening, depending on the fiber delay. We therefore fit Gaussian functions to the exiting pulse train to extract the mean and variance of each time-bin. As a result, we can dynamically adjust our evaluation time-windows to the optical beam width. For the analysis, we show 2σ and 3σ time windows.

3.4.3 Results

With our setup, we can record a click-correlation matrix between signal and idler mode, as shown in Fig. 3.9. For our additional analysis, we use the idler mode for heralding up to $N = 10$ counts (before statistical uncertainties become dominating). Figure 3.10 shows all ten heralded states, which are spread over $M = 64$ modes. Therefore, we are able to analyze correlations in $K = 1$ to $K = 64$ modes. As expected, it can be seen that the minimal eigenvalue is decreasing for increasing mode size M (better indication for non-classicality). For example $N = 1$ and $K = 1$ does not show any signs of non-classicality due to high noise values when all other 63 modes are traced out. Likewise, for $N = 10$ statistical uncertainties prevent a clear identification of non-classicality. In a range from $N = 3$ to $N = 7$, we can identify non-classicality with the highest significance (simultaneously accounting for the absolute value and measurement uncertainties).

In summary, we have shown a new benchmarking tool to analyze state generation, propagation, and detection jointly. With our setup, we could demonstrate nonclassical correlation signatures with binary detectors between the output modes. Up to ten photons spread over up to 64 correlated modes were analyzed with correlation functions, having a maximal order of 128.

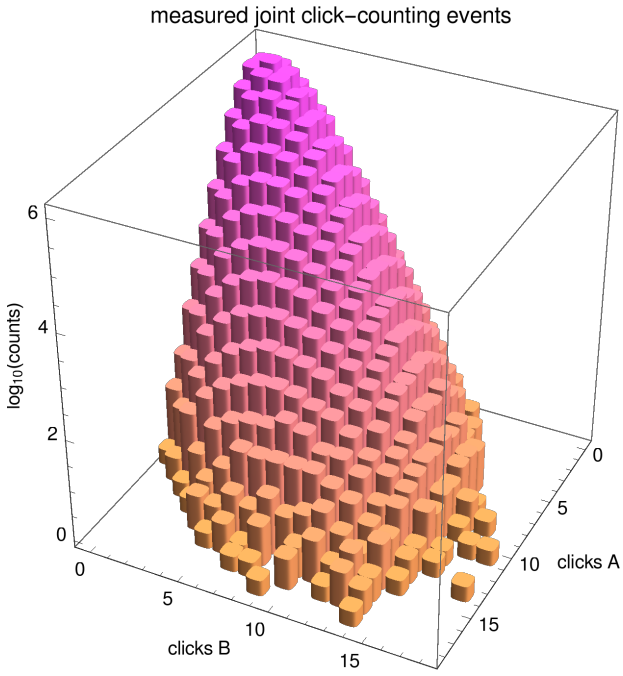

Figure 3.9 – Coincidence matrix between signal and idler mode for a pump power of 500 μW. For the analysis 3σ time windows were chosen.

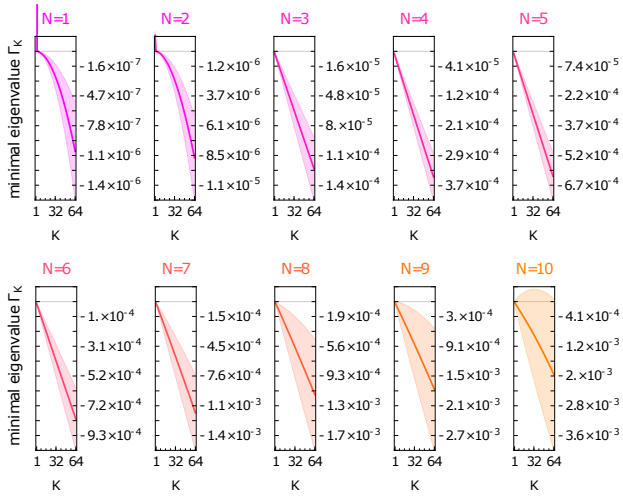

Figure 3.10 – K-mode non-classicality derived via the minimal eigenvalues of the matrix of moments Γ_K with $N \in \{1, ..., 10\}$ heralded photons distributed over $M = 64$ modes. Shaded area shows one-standard-deviation error margin and includes random and systematic errors. For the analysis, a dynamical 2σ time window was chosen for the exiting pulses. Nearly all 640 analyzed cases can verify non-classicality.

3.5 High dynamic range detection

In this section, we will discuss how the dynamic range of single-photon detectors can be extended even further. The content of this section was published in [144, 145]. To be more precise about the dynamic range, we will differentiate between four different response areas. Initially at very low light levels, many detectors have a noise floor where the detector response is independent of the incoming light field. Secondly, we can see a linear region where the response function is proportional to the incoming light intensity. This region is crucial to extract information about the incoming light field from the detector response. Above this region, we define the saturation region as an area where the response function from the detector is again independent of the incoming light intensity. It is finally limited by the breakdown intensity, which is the point where the detector response is permanently changed (i.e. damaged or latched).

We have already seen in Sec. 3.2 that 'click'-detectors have an extremely low (single-shot) dynamic range as they can only differentiate between 'no-photons' and 'one or more - photons'. For many situations (e.g. quantum state tomography), this extreme case is not valid, and ensemble measurements, where the same copy of an incoming pulse is investigated multiple times, must be considered. In this case, the lower limit of the linear dynamic range can be substantially decreased as it is bounded by the dark-count rate per measurement time window. Still, the upper end of the linear range is given by one photon per measurement window. The idea of multiplexing was developed to extend the dynamic range towards the few-photon regime. This idea can be realized in various physical implementations, which have been analyzed in detail over the past few decades [20–25, 109, 146–154]. However, saturation effects in multiplexed detectors were avoided and considered as a limiting factor [110]. Although saturation effects can be compensated to some extend by careful calibration routines, the fundamental problem is still present: large intensity fluctuations cause small response changes. The effect of detector saturation has also been addressed for intrinsic photon-number-resolving detectors [155]. However, the fundamental problem stays: If additional noise sources (for example from coupling drifts or dark counts) are present, a precise inversion of the photon-number convolution from the multiplexing element is often not possible.

In [145] we addressed this problem and explored the saturation region of multiplexed detectors. The key property of the experimental setup is an asymmetric multiplexing scheme where the bin click probability is changing (in our case exponentially decreasing due to the cycling loop configuration). This has the advantage that the initial bins can be saturated (which means limited informational content) while later bins are not. The next sections will illustrate how this method can be implemented to significantly increase the upper limit of the linear dynamic range far beyond the few photon regime and therefore increase the dynamic range of single-photon detectors. As an application, a direct calibration routine for single-photon detectors is shown.

3.5.1 Measurement scheme

The measurement scheme for the high dynamic range detector is shown in Fig. 3.11. The setup itself is an old concept that was introduced in 2003 [22] and further investigated in [24, 146, 156]. An incoming light pulse is split on a beam splitter that has a (variable) transmission value. In the following, we will differentiate two schemes. Firstly, a beam splitter reflectivity R that is

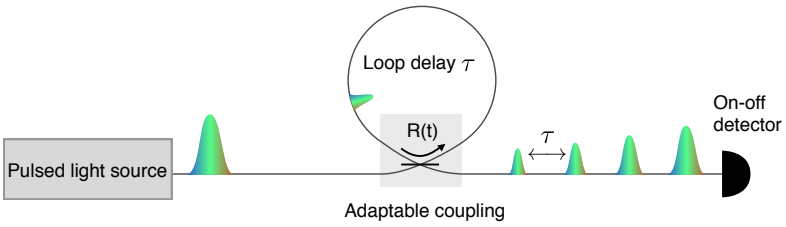

Figure 3.11 – Pulsed light is sent to a beam splitter with a variable reflectivity $R(t)$. Light exiting the loop will follow an exponential decay. See text for further details. Reprinted from [145]. ©2019 Optical Society of America.

constant for all times (passive case) and secondly a beam splitter that transmits everything for the first incoming pulse and has a constant reflectivity R for all later times (active case). For both cases, the one output port of the beam splitter is connected to the second input port of the same device. Therefore some parts of the light field will stay inside the loop while some proportion is constantly coupled out and detected with a 'click' detector. Due to the constant coupling ratio, the pulses leaving the loop exponentially decrease in intensity. The separation of these pulses τ is given by the loop traveling time and should be set such that the pulse separation τ is longer than the dead time of the detector.

3.5.2 Theoretical considerations I: Calculating click probabilities

For the following calculations, it is important to know the click probabilities for the j-th time-bin p_j^{click} leaving the loop. This probability will depend on the dark-count rate per bin ν and the probability of having n photons present in the j-th bin $p_j(n)$. Using the unit measure axiom for the probabilities we can write

$$\begin{aligned} p_j^{\text{click}} &= 1 - p_j(0) p_{\text{no dark counts}} \\ &= 1 - p_j(0)(1-\nu) \\ &= 1 - p_j(0) + p_j(0)\nu \,. \end{aligned} \tag{3.11}$$

In order to calculate the vacuum probability $p_j(0)$, we have to take into account the actual measurement scheme (active or passive case). Especially the first bin ($j = 1$) shows a difference as either the whole light is coupled into the loop (active) or some proportion is directly coupled to the detector (passive). The probabilities can be written as

$$p_{j=1}(0) = \begin{cases} [1 - \eta\,(1-R)]^n & \text{active} \\ (1-R)^n & \text{passive} \,. \end{cases} \tag{3.12}$$

For all following bins, the click probability is given by

$$p_{j\geq 2}(0) = \begin{cases} \left[1-(R\eta)^{j-1}\,\eta\,(1-R)\right]^n & \text{active} \\ \left[1-(R\eta)^{j-1}\,R^{-1}\,(1-R)^2\right]^n & \text{passive}\,. \end{cases} \tag{3.13}$$

With these equations we can now derive analytic expressions for Fock states $p_{\text{Fock}}(n) = \delta_{n,\bar{n}}$, coherent states $p_{\text{coh}}(n) = \exp\left[-\bar{n}\right]\frac{\bar{n}^n}{n!}$ and thermal states $p_{\text{therm}}(n) = \frac{\bar{n}^n}{(1+\bar{n})^{n+1}}$ with the same mean photon number $\bar{n}$. For the active case, this results in

$$p_j^{\text{click, Fock}} = 1-(1-\nu)\left[1-(1-R)\,R^{-1}\,(R\eta)^j\right]^{\bar{n}}\,, \tag{3.14}$$

$$p_j^{\text{click, coh}} = 1-(1-\nu)\exp\left[-(1-R)\,R^{-1}\,(\eta R)^j\,\bar{n}\right]\,, \tag{3.15}$$

$$p_j^{\text{click, therm}} = 1-(1-\nu)\,\frac{R}{R+(1-R)\,(R\eta)^j\,\bar{n}}\,. \tag{3.16}$$

For the passive case, the probabilities are given by

$$p_j^{\text{click, Fock}} = \begin{cases} 1-(1-\nu)\,(1-R)^{\bar{n}} & j=1 \\ 1-(1-\nu)\left[1-(1-R)^2\,R^{-1}\,(R\eta)^{j-1}\right]^{\bar{n}} & j\geq 2\,, \end{cases} \tag{3.17}$$

$$p_j^{\text{click, coh}} = \begin{cases} 1-(1-\nu)\exp\left[-R\bar{n}\right] & j=1 \\ 1-(1-\nu)\exp\left[-(1-R)^2\,R^{-1}\,(\eta R)^{j-1}\,\bar{n}\right] & j\geq 2\,, \end{cases} \tag{3.18}$$

$$p_j^{\text{click, therm}} = \begin{cases} 1-(1-\nu)\,\frac{1}{1+R\bar{n}} & j=1 \\ 1-(1-\nu)\,\frac{R^2\eta}{R^2\eta+(1-R)^2(R\eta)^j\bar{n}} & j\geq 2\,. \end{cases} \tag{3.19}$$

Figure 3.12 shows the bin click probability for these three states and two mean photon numbers of $\bar{n}=1$ and $\bar{n}=800$ in the active case. It can be seen that the shape of the bin probabilities is state-dependent. This is a unique feature for asymmetric loop architectures causing non-uniform bin click probabilities in combination with saturation. This feature can be understood intuitively by considering the non-linearity of the bin height with respect to the number of incoming photons for this bin. For example, we can compare coherent states and thermal states with the same mean photon number. The probability of having a photon number smaller than the mean is now higher for a thermal state compared to a coherent state. If we are close to the saturation region, having more photons has a weaker effect on the bin probability than having fewer photons. Therefore the thermal state has lower values in the transition from the saturation region to the exponential decay region compared to the coherent state (see Fig. 3.12 (b)). We will revisit the effects of the photon-number distributions more quantitatively in the next section.

For now, we will investigate one of these states, namely the coherent state in detail. The click probability versus bin number is shown in a linear and logarithmic scale in Fig. 3.13, where we can identify three different areas I-III. Area I shows the saturation regime of the detector where the mean photon number per bin is far above one and therefore the click probability is

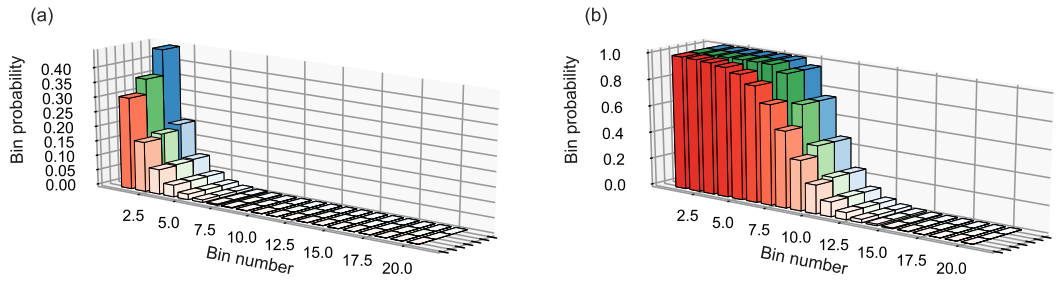

Figure 3.12 – Calculated click probabilities p_j for a Fock state (blue), coherent state(green) and thermal state(red) for a mean photon number of $\bar{n} = 1$ (a) and $\bar{n} = 800$ (b). Both figures show active switching with a beam splitter reflectivity $R = 0.5$ and a loop transmission $\eta = 0.9$. See text for further details.

nearly one. After the saturation region, we can see an exponential decay with a linear slope in the logarithmic plot (area II). This area is of practical interest as these bins are susceptible to small intensity variations. It is important to note that this area always exists independent of the incoming light field. For higher or lower light intensities, it is simply shifted to lower or higher bin numbers. In other words, this detection method is self-adjusting the linear range of the detector. The only limiting factors are the damage threshold, where the detector is permanently changed, and the dark count level. For high intensities, the first bin will receive a significant amount of the incoming light field, which can cause a permanent change of the detector. For very low light intensities the detector dark-count rate becomes important. This level is finally shown in area III.

3.5.3 Theoretical considerations II: Mandel Q-parameter revisited

In this section, we will discuss how features of non-classical light can be uncovered using the loop. In Fig. 3.12 we have already seen that the bin click probabilities p_j are state-dependent. Here we want to be more quantitative about this property and use the idea of the Mandel Q-parameter as discussed in Sec. 3.1.4 to quantify non-classicality. Although the Mandel Q-parameter is a straightforward concept, it is usually difficult to compute as the actual photon-number distribution needs to be known. This problem has been addressed in [114], where the concept of the Mandel Q-parameter was generalized for click detectors. In this case, the binomial distribution of click detectors with the corresponding Q_{B}-parameter is investigated. The Q_{B}-parameter is able to identify non-classicality for equally split multiplexed detection schemes. Unequal splitting combines a majority of photons in a few bins. Therefore it is intuitively clear that unequal splitting can fake sub-Poissonian light if this effect is not appropriately accounted for. Theoretically, this property was analyzed in [157], where an additional factor is added to compensate for this effect. The final parameter which is suitable to quantify the non-classicality

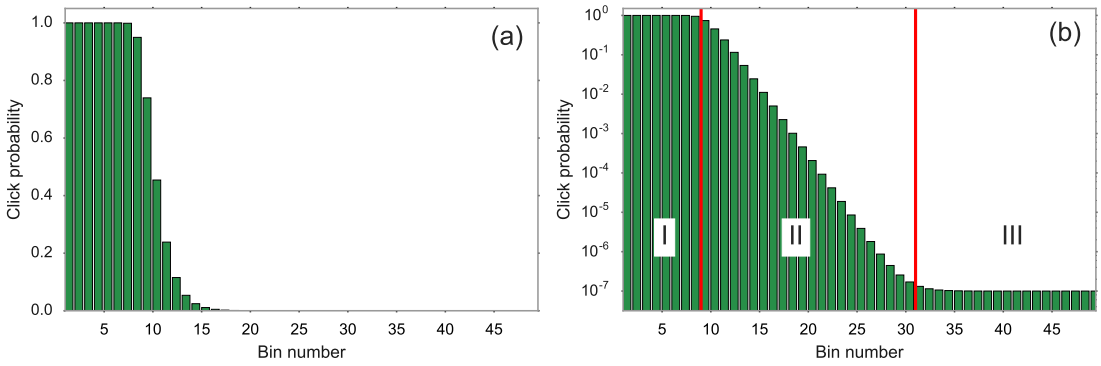

Figure 3.13 – Expected bin click probability (passive case) for a coherent state with a mean photon number of 800 on a linear (a) and logarithmic scale (b). In the logarithmic case (b) three different areas can be identified (separated with red lines). (I) Saturation regime with unit click probability, (II) exponential decay region with a linear slope in the logarithmic plot and (III) noise level from detector dark counts.

for the given loop detector is called the Q_{PB}-parameter which is defined as

$$Q_{PB} = N \frac{\langle (\Delta c)^2 \rangle}{\langle c \rangle \left(N - \langle c \rangle\right) - N^2 \sigma^2} - 1 \, . \tag{3.20}$$

Here the mean and variance of the probability c_k that k bins detect a photon at the same time are given by

$$\langle c \rangle = \sum_{k=0}^{N} k c_k; \; \langle (\Delta c)^2 \rangle = \sum_{k=0}^{N} \left(k - \langle c \rangle\right)^2 c_k \, . \tag{3.21}$$

Likewise the mean probability m and variance σ of the bin click probability p_j can be calculated from a total number of N bins

$$m = \frac{1}{N} \sum_{j=1}^{N} p_j; \; \sigma^2 = \frac{1}{N} \sum_{j=1}^{N} \left(p_j - m\right)^2 \, . \tag{3.22}$$

All these parameters commonly require the knowledge of the number of bins c_k that clicked simultaneously, instead of only evaluating the average bin probability p_j. We have already seen that bin click probabilities p_j can be easily calculated, whereas the calculation of c_k is more demanding. Likewise, it is also not possible (without the knowledge of the quantum state) to convert the bin probabilities p_j into the number of bins that simultaneously clicked c_k. If the quantum state is known, calculating c_k from p_j is, in general, still a complicated problem as all permutations leading to k simultaneous events need to be considered. A trivial example, however, is the coherent light field as it does not show any photon-number correlations after a beam splitter. This means that the click probability for each bin is independent of all other

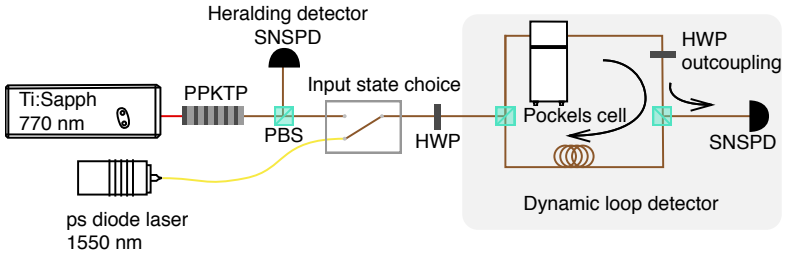

Figure 3.14 – Experimental setup showing a loop with a dynamically variable beam splitter. Either thermal light and heralded single photons from a KTP waveguide or coherent states from a diode laser can be coupled to the loop. The amount of light exiting the loop can be determined with a half-wave plate (HWP). Reprinted from [145]. ©2019 Optical Society of America.

bins. It can be shown that the Q_{PB}-parameter is zero for a coherent state, and a negative value indicates sub-Poissonian light and therefore non-classicality.

3.5.4 Experimental setup

One advantage of our detection scheme is that the experimental setup can be realized with only a beam splitter and a fiber delay line. Here we used a slightly more complicated setup to dynamically change the beam splitter reflectivity while the light pulse is traveling in the loop, as shown in Fig. 3.14. The switching was realized with a free-space electro-optic modulator (EOM), which enables high transmission values above $98\,\%$ and fast switching times in the μs regime. For this reason, a round trip time of 2.4 μs was chosen corresponding to a loop length of 480 m. We have investigated coherent states from a PicoQuant diode-laser, thermal states, and heralded single photons from parametric down-conversion. Further details about this setup are shown in [158]. The exiting light field was measured with an SNSPD, which is connected to a time tagger. Start-(multi)stop histograms were recorded with the incoming laser pulse as the trigger.

3.5.5 Results

The recorded histograms were analyzed each measurement run (one incoming pulse to the loop defines one measurement) to evaluate the bin click probability p_j and the simultaneous click probability c_k. This enables us to calculate the Q_{B}-parameter and the Q_{PB}-parameter, which are shown in Fig. 3.15. The measurement illustrates that an asymmetry in the splitting ratio must be considered in the analysis; otherwise, as given by the Q_{B}-parameter of the thermal light, non-classicality signatures can be counterfeit. The error bars were calculated based on a Monte-Carlo-simulation with 10000 runs, where the mean and variance of the c_k parameter are experimentally determined.

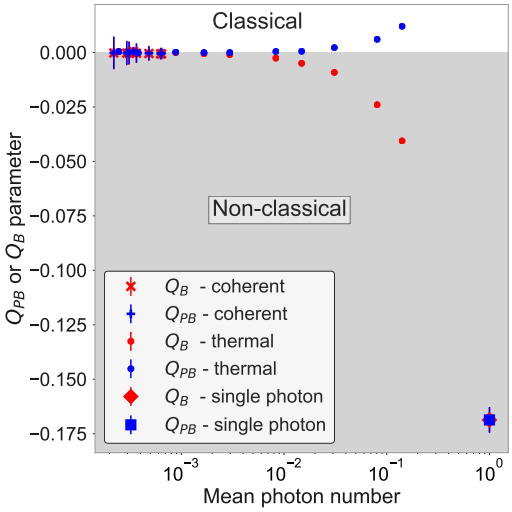

Figure 3.15 – Q_{B} and Q_{PB} parameter as a function of the mean photon number for coherent, thermal and single-photon states. See text for further details. Reprinted from [145]. ©2019 Optical Society of America.

3.5.6 Application: Calibration of single-photon detectors

To show the full potential of our new measurement scheme, we want to address an outstanding problem for single-photon detectors: A direct calibration of a single-photon detector based on a reference power meter. On the one hand, calibrated power meters are available, which are typically sensitive down to the few 100 pW range where the noise floor starts to dominate the measurement. One the other hand single-photon detectors can typically only resolve count rates up to a few MHz before they alter their operation (e.g. change to a permanently normal conducting state in case of SNSPDs), which is equivalent to an optical power of around 100 fW assuming not more than one photon per count. In order to close this gap and calibrate single-photon detectors to a known power meter reference, calibrated attenuators are necessary (e.g. [159, 160]). In [145], we showed for the first time that for SNSPDs, today one of the most commonly used single-photon detectors, the dynamic range can be extended to the nW range. This enables direct calibration of SNSPDs without the need for attenuators.

3.5.6.1 Theoretical considerations

In the following, we will derive a calibration procedure for the passive case. Further information, for example, about the active case and additional considerations regarding the measurement uncertainties, can be found in [145]. All equations shown above relate the photon numbers before the multiplexing loop to a click probability. If the beam splitter reflectivity R and loop

losses η are known, we can relate the input and output power

$$\bar{n}_{\text{out}} = \frac{\bar{n}_{\text{in}}(-R-\eta+2R\eta)}{-1+R\eta}, \tag{3.23}$$

where $\bar{n}_{\text{in}}$ is the mean photon number per pulse present before entering the loop and $\bar{n}_{\text{out}}$ the mean photon number after the loop. In case R and η are not known, a simple measurement can be performed to extract these values. An unknown attenuator is placed in front of the loop. It is important to note that the value of this attenuator is irrelevant for all further calculations. The only reason for this attenuator is to lower the optical power going to the click detector such that the first bin is not saturated anymore. If this is the case, then a simple fit based on Eq. 3.18 can be used to extract R and η. This additional measurement is only necessary for the passive case where the first bin is distinct (light in this bin does not see the loop loss η. Therefore, the symmetry between R and η for all later bins is not present). In the active case, this additional step is not necessary as only the product of R and η can be observed, which is given by the slope of the exponential decay region. Nevertheless, we concentrate here on the calibration procedure based on the passive case because a reliable, ultrafast active switch is difficult to implement. After this measurement, the additional attenuator can be removed. Using Eq. 3.18 and Eq. 3.23 we can now calculate for each bin individually the expected number of photons having measured the click probability p_j

$$\bar{n}_{\text{out}}|_j = \begin{cases} \frac{(R+\eta-2\eta R)\ln\left[\frac{1-\nu}{1-p_j}\right]}{R(1-R\eta)} & j=1 \\ \frac{(R+\eta-2\eta R)(R\eta)^{1-j}R\ln\left[\frac{1-\nu}{1-p_j}\right]}{(1-R\eta)(R-1)^2} & j\geq 2\,. \end{cases} \tag{3.24}$$

Considering the individual uncertainties an estimate for the measured photon number can be derived

$$\bar{n}_{\text{measured}} = \frac{\sum_j w_j \bar{n}_{\text{out}}|_j}{\sum_j w_j}\,, \tag{3.25}$$

where

$$w_j = \frac{1}{\sigma^2_{\bar{n}_{\text{out}}|_j}} \tag{3.26}$$

shows the uncertainty per bin $\sigma_{\bar{n}_{\text{out}}|_j}$. By either placing an optical power-meter after the loop or connecting it directly to SNSPDs the system detection efficiency η_{SDE} of the click detector can be calculated without the need of changing the power level

$$\eta_{\text{SDE}} = \frac{\bar{n}_{\text{measured}}}{\bar{n}_{\text{PM}}}\,. \tag{3.27}$$

A detector calibration procedure requires the following steps

1. Connect a pulsed laser to a loop detector, as shown in Fig. 3.16.

2. Measure the optical power with a calibrated power meter after the loop.

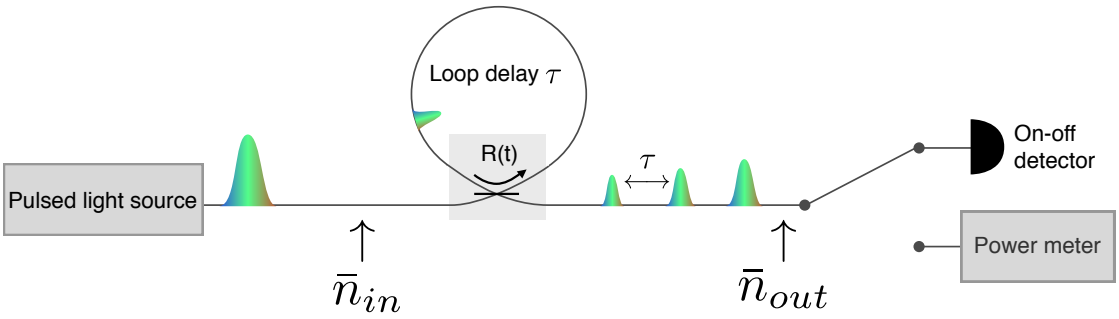

Figure 3.16 – Schematic picture of the calibration procedure. The loop detector is either connected to a single-photon detector or a power meter. Reprinted from [145]. ©2019 Optical Society of America.

3. Connect the loop to the SNSPD.
4. Measure the bin click probability p_j.
5. Insert unknown attenuator before the loop such that the first bin is not saturated anymore.
6. Measure the bin click probability p'_j again.
7. Calculate beam splitter reflectivity R and loop efficiency η based on p'_j.
8. Calculate the measured mean photon number based on Eq. 3.25.
9. Calculate the system detection efficiency based on Eq. 3.27.

3.5.6.2 Experimental realization

The suggested calibration routine presented in the previous section is now implemented to determine the system efficiency of an SNSPD. A key result from our work is that the response from an SNSPD is, to first-order, independent of the pulse peak power. The laser repetition rate, however, is a more critical parameter. Therefore high average optical powers can be measured if the repetition rate is low and the peak power is high. This behavior is shown in Fig. 3.17, where the number of counts is shown as a function of the laser repetition rate and photon number per pulse. White areas show regions where latching occurred. For the experiment again a PicoQuant diode-laser with a repetition rate of 50 kHz is used to generate a pulse train entering the loop. The exiting pulse train is either measured with a reference power meter or an SNSPD and a time tagger. The key property is that the same power level can be measured without the need for additional attenuators for the single-photon detector. An example histogram from the time tagger is shown in Fig. 3.18 (a). Exiting pulses have a separation of 156 ns, which is determined by the loop round trip time. In contrast to the previously described experimental setup, we will use a polarization-maintaining fixed-ratio beam splitter and a polarization-maintaining delay fiber

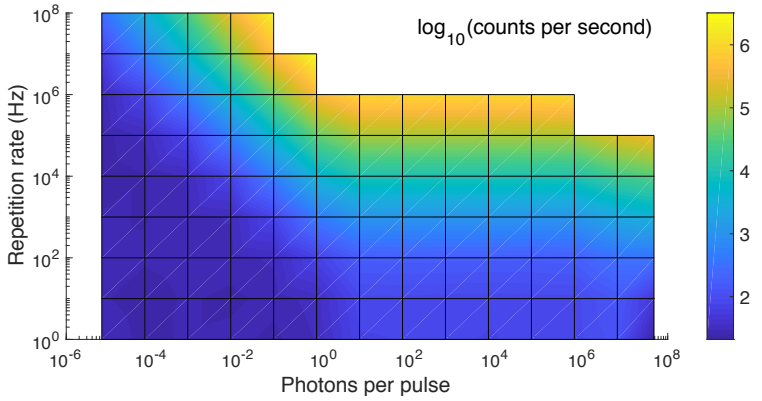

Figure 3.17 – Detector count rate in dependence on the laser repeititon rate and pulse energy. Detector latching occoured in white areas. See text for further details. Reprinted from [145]. ©2019 Optical Society of America.

for the loop. This guarantees maximal stability for the required parameters during the measurement run. A polarizer was placed before the setup to couple to the polarization preserving axis of the fiber. All clicks are integrated over a four ns time window around these maxima of the histogram. We will refer to these windows as time bins. Knowing the number of clicks per time bin, the bin click probability p_j can be calculated, which is shown in Fig. 3.18 (b). The three areas (saturation regime, decay region, and noise level) can be clearly seen in the logarithmic plot Fig. 3.18 (c). From the noise level of 10^{-7} photons/pulse to the latching threshold of $> 2.5 \cdot 10^5$ photons/pulse, we can span a dynamic range of 123 dB with our detection scheme. Following the calibration steps shown before, we can also calculate the detector system efficiency of $82.8 \pm 4\,\%$.

In summary, we have shown that our new characterization device can characterize optical states over a very large dynamic range and is still able to identify sub-Poissonian light statistics. In this context, another link between CV and DV is important: Bright amplitude squeezed states have sub-Poissonian light statistics [15, 161] (if the squeezing value is not too high with respect to the amplitude). As squeezed states are becoming more important for sensing applications (e.g. [162]), we have created a new method that will be helpful to verify the quantum aspect of these states.

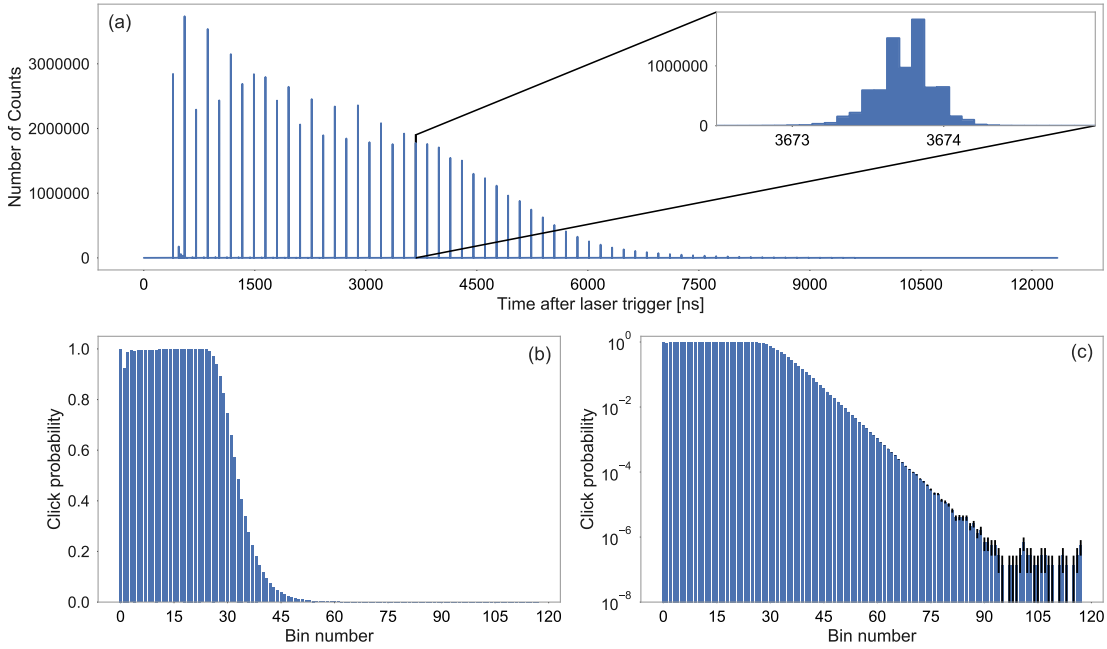

Figure 3.18 – Time tagger histogram of the exiting pulse train detected with a single photon detector. Pulse heights vary due to the binning of the detected clicks (compare with inset showing a single time bin). All time bins are integrated over a 4 ns window to determine the bin click probability shown on a linear scale (b) and logarithmic scale (c). Error bars (black lines) are calculated from the measured binomial distribution. See text for further details.

3.6 Multi-element SNSPDs

While the previous sections focused on temporal multiplexing, we will now consider spatial multiplexing as an alternative. One way to achieve spatial multiplexing is to split the active area of a binary detector into multiple detectors with smaller active areas (known as pixels). This research field has gained increasing attention in recent years, mainly because it offers the possibility to use SNSPD detectors with their advantages for image reconstruction. In addition, SNSPDs can be designed to be sensitive to wide range of optical frequencies such as mid- and far-infrared [163], making them a perfect candidate for exoplanet search or military imaging applications. To date, SNSPD units of 1024 pixels have been demonstrated [154] and the route towards megapixel detectors is under investigation. On the quantum side, larger detectors enable, for example, the characterization of bright quantum states, which are interesting for metrology applications.

One major challenge for these detectors is a suitable readout strategy. Connecting each pixel individually from the detector to the readout electronic is not feasible as this significantly increases the heat load on the cryogenic system. For this reason, a variety of readout schemes

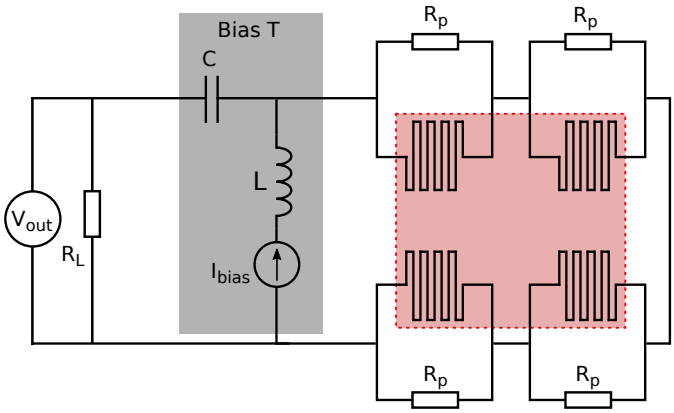

Figure 3.19 – Four-pixel SNSPD wired in series (red). Each pixel is connected to a resistor R_p which acts as a shunt resistor. All pixels are constantly biased with a current I_{bias} using a bias T configuration. The output voltage V_{out} is measured across a load resistor R_L.

has been investigated [164] based on on-chip or off-chip processing. In this section we will show a readout method based on a single electric wire. The discussion shown here focuses on multi-element SNSPDs in the context of photon-number resolution. Nevertheless, the presented method can be adapted to imaging applications as well.

In the context of the readout scheme, we will also analyze the error associated with the readout. Although we focus in this section on a quite specific example (single-channel readout scheme for multi-pixel SNSPDs), the analysis shown here is more general. Significantly, the distinction between ensemble measurements and single-shot experiments is often neglected in the literature. An ensemble measurement records data for multiple measurement runs. Then an outcome value is extracted from this data set. In contrast, a single-shot experiment extracts an outcome value for each measurement. As an example, a complete state characterization is possible with a single binary detector (see Chap. 4, ensemble measurement), whereas the same detector is entirely unsuitable for heralding of higher-order Fock states (see Sec. 2.3, single-shot). Therefore we differentiate these two cases in our error analysis. The content of this section was published in [165].

3.6.1 Single-channel readout method

In order to read out a multi-pixel SNSPD with a single electric channel, the individual pixels are connected in series, as shown in Fig. 3.19. All pixels are biased with a constant current using a bias T configuration. If a photon is absorbed by one pixel, the resistance of this pixel increases, and the current is redirected through the corresponding parallel resistor R_P. This leads to a voltage peak V_{out}, which can be measured over a load resistor R_L. The measured voltage will have discrete amplitude values depending on the number of pixels that detected a photon. We can model the voltage response $V(t)$ after an event with n pixels with an exponentially

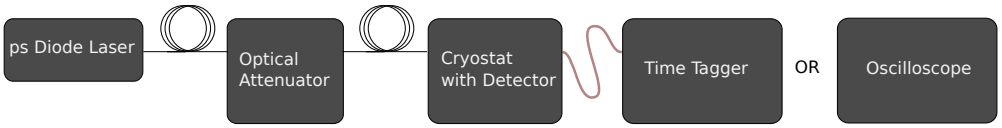

Figure 3.20 – Schematic measurement setup used to evaluate a four-pixel SNSPD. See text for further details.

decreasing function

$$V_n(t) = nAe^{-\frac{t}{\tau}} \tag{3.28}$$

with a decay constant τ and an amplitude A.

In many measurement configurations, SNSPDs are evaluated with time taggers (see Sec. 3.3). The drawback of such a measurement is that the time tagger is only sensitive to a specific threshold. However, the information on the 'how many pixels' is encoded in the peak height of the voltage pulse. Here an oscilloscope measurement would be better suited but suffers from the disadvantages described in Sec. 3.3. We therefore suggest a new method, which is based on the time-over-threshold value of a multi-pixel SNSPD. For this method, both the time when the signal rises past the threshold A_0 as well as the time when the signal falls past this value is recorded. The time difference defines the time-over-threshold value $t_{\text{over thres}}$

$$t_{\text{over thres}}(n) = -\tau \ln\left(\frac{A_0}{nA}\right) , \tag{3.29}$$

which will be used to determine the number of pixels that detected a photon n. As a comparison, we will use an oscilloscope measurement as a reference.

3.6.2 Experimental setup

The measurement setup consists of a pulsed diode laser (PicoQuant, pulse duration 50 ps) that emits light with a repetition rate of 100 kHz and a wavelength of 1550 nm (see Fig. 3.20). The emitted light pulses are attenuated with an optical attenuator to the few photon level and detected with a four-pixel SNSPD detector (PhotonSpot), as shown in Fig. 3.19. The electrical output from the detector is either measured with an oscilloscope or a Time Tagger Ultra (Swabian Instruments). Twenty-five different thresholds A_0 are investigated with the time tagger and the corresponding time-over-threshold value is recorded.

3.6.3 Evaluating click probabilities

In order to evaluate the quality of the presented readout scheme, we have to calculate the click probability c_k of k simultaneous detection events. The general idea of the evaluation is demonstrated in Fig. 3.21. The voltage response of 500 outcomes of a four-pixel detector is shown as a heatmap in (a). As a next step, the time-over-threshold value is recorded for three different thresholds (12 mV, 16 mV, and 28 mV) and plotted as a histogram (b)-(d). Finally, we compare

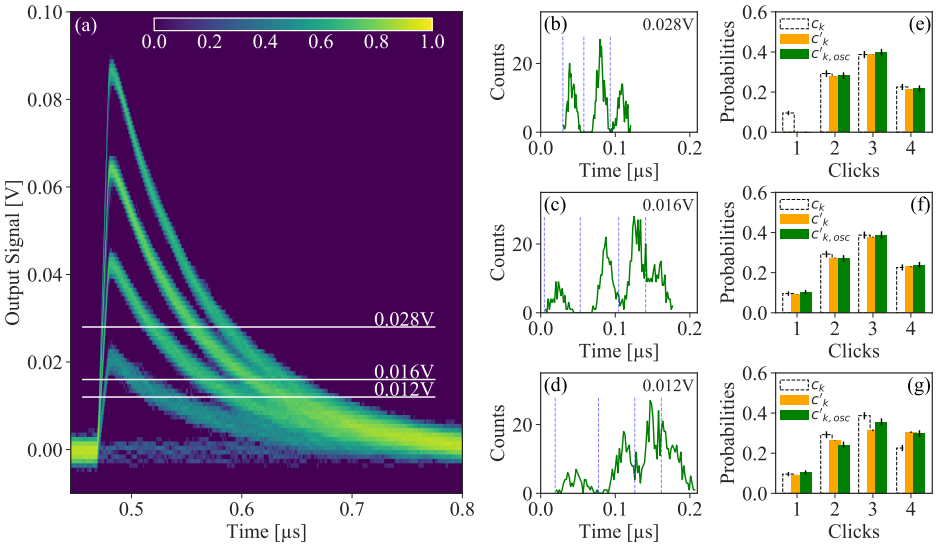

Figure 3.21 – Evaluating click probabilities using the time-over-threshold value. A heatmap showing 770 oscilloscope traces (a) is cut at three voltage levels (b-d). The resulting histograms are integrated to calculate the click probability and compared with time tagger measurements and a reference value derived from the voltage maximum of the oscilloscope trace (e-f). See text for further details. Reprinted from [165]. ©2020 Optical Society of America.

the time-over-threshold method from the oscilloscope $c'_{k,\text{osci}}$ with the time-over-threshold value from the time tagger c'_k and the reference value from the oscilloscope derived from the voltage height in the maximum c_k (see subfigures (e) - (g)). An overall correspondence between the values can be seen.

To be more precise about the derivation of the click probabilities, we have to distinguish between ensemble measurements and single-shot evaluation as discussed before.

Ensemble measurement:
For ensemble measurements, we record a histogram of the time-over-threshold value for the oscilloscope $h_{\text{exp, osci}}$ (see Fig. 3.21 (b)-(d)) and time tagger $h_{\text{exp, tagger}}$ (see Fig. 3.22 (b)-(d)). As a next step, Gaussian functions g_k with a mean value μ_k are fitted to the histogram $h_{\text{exp, tagger}}$. Finally, the click probability can be calculated by

$$c'_k = \frac{1}{M} \int dt\, g_k(t) \tag{3.30}$$

where M is the total number of measurements.

Single-shot measurement:
For a single-shot evaluation, we have to estimate for each measurement the number of detectors

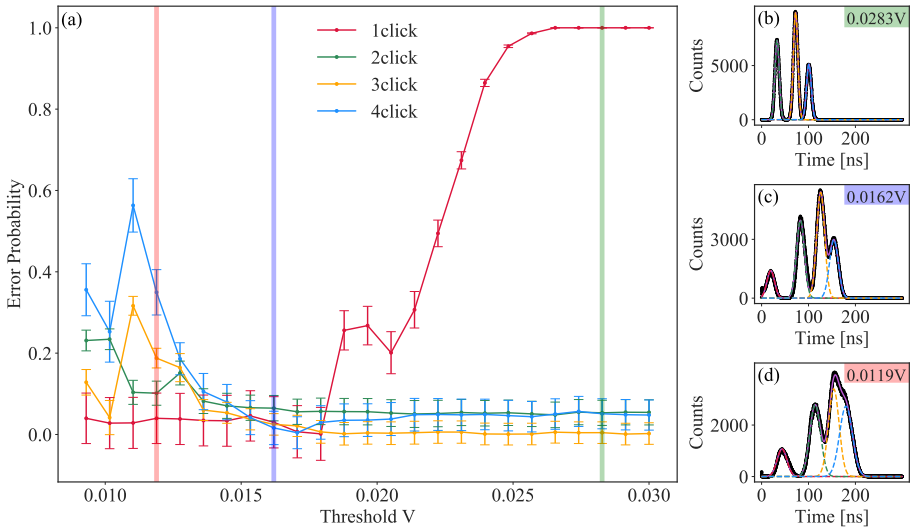

Figure 3.22 – Error probability for ensemble measurements. See text for further details. Reprinted from [165]. ©2020 Optical Society of America.

that detected a photon simultaneously k. We also record the time-over-threshold value in this case. In the next step, we divide this time duration into k sections based on the mean value of the fitted Gaussian functions μ_k. The upper boundaries u_k of these sections are given by

$$u_k = \begin{cases} \frac{\mu_{k+1}+\mu_k}{2} & k < k_{\max} \\ \infty & k_{\max} \end{cases} . \tag{3.31}$$

Note that an optimal position of these boundaries will depend on the optical input state, and an initial ensemble characterization step is required. Here we chose the center position between the Gaussian maxima, which is optimal for a constant click probability c_k or no a priori information about the input state. Depending on the actual measurement scenario, this value can be modified. The lower boundaries are given by $l_k = u_{k-1}$ with the special case of $l_1 = 0$.

With these time-sections, every measurement can be connected with a specific event with k clicks. The total click probability for single-shot experiments c''_k is given by

$$c''_k = \sum_{l_k}^{u_k} h_{\text{exp, tagger}} . \tag{3.32}$$

3.6.4 Error analysis

As shown for the derivation of click-probabilities, we will split the error analysis into ensemble measurements and single-shot experiments.

Ensemble measurement:
For the ensemble measurements, we will compare the measured click probabilities c'_k with the oscilloscope reference measurement c_k to quantify the relative error

$$p_{\text{error},k} = \frac{|c_k - c'_k|}{c_k} \,. \tag{3.33}$$

The relative error $p_{\text{error},k}$ is shown in Fig. 3.22 (a) for 25 different threshold values. For low threshold values the error probability, especially for the three and four click event, is significant due to highly overlapping Gaussian functions (see Fig. 3.22 (d)). With an increasing threshold, this error decreases as the overlap of the Gaussian functions is reduced. For high thresholds ($> 18\,\mathrm{mV}$), the error bar of the single-click component starts to increase because the threshold starts to exceed the voltage response of the single-click event. For even higher values (not shown in the figures) also the errors for the two, three and four-fold events would increase. Therefore an optimal threshold can be found around $16.2\,\mathrm{mV}$. Further information about the error bars can be found in [165].

Single-shot measurement:
The situation for single-shot measurements is slightly more complicated. To start with, we have to compare our single-shot results to ensemble measurements to determine the errors because the photon number of each measurement run is fundamentally unknown for a characterizing coherent state. In addition, we have to differentiate two situations; entirely analogous to errors of type I and II in hypothesis testing. Firstly, we can miss an event with k detected photons. Secondly, we can accidentally identify an event with $j \neq k$ photons as an event with k detected photons. This means that the first error will decrease and the second error will increase the probability c_k. Depending on the actual application, these errors can have very different implications. As an example, we will consider heralding of higher-order Fock states (for more information see See. 2.3). Here a missed click will reduce the heralding probability whereas a misidentified click-probability will lower the fidelity of the heralded Fock-state. In order to quantify both relative errors, we can define both values as

$$p_{\text{missing click, }k} = 1 - \frac{1}{M'_k} \int_{l_k}^{u_k} dt\, g_k(t) \tag{3.34}$$

and

$$p_{\text{misidentified click, }k} = \frac{1}{N'_k} \sum_{i \neq k} \int_{l_k}^{u_k} dt\, g_i(t) \,. \tag{3.35}$$

Strictly speaking, the missing click value is not an error probability as the definition allows for negative values (probability of an event is higher than expected). We therefore refer to this value as a missing-click factor. Both errors are shown in Fig. 3.23. The dependency for the missing-click factor is analogous to the ensemble measurement. Low thresholds suffer from overlapping Gaussian functions, whereas high thresholds miss the single-click component. The situation is

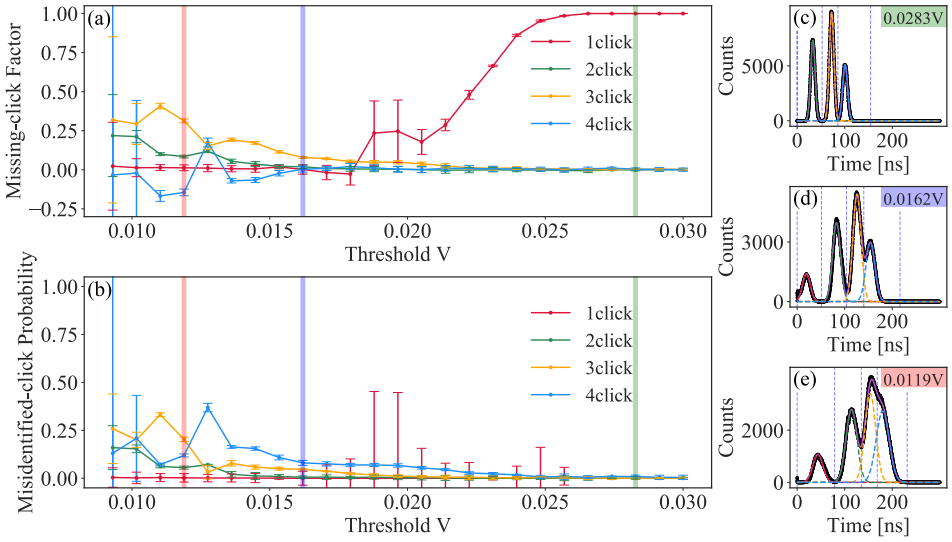

Figure 3.23 – Missing click factor and misidentified click probability for single-shot measurements. See text for further details. Reprinted from [165]. ©2020 Optical Society of America.

slightly different for the misidentified click probability. Here the error simply decreases with an increasing threshold because the Gaussian functions have a lower overlap. For thresholds above 25.7 mV the error for the single-click counts can not be calculated because no clicks were recorded.

3.6.5 Scaling

An important factor that should be considered for any scheme is scalability. Here scalibility means increasing the number of pixels in order to achieve better photon-number resolution. For a given threshold a_0 the difference in the time-over-threshold $t_{\text{over thres}}(n)$ for two neighboring events n and $n+1$ will decrease logarithmically in n (see Eq. 3.29). This becomes problematic in the presence of noise, which we want to investigate further. We will assume that all noise sources have a Gaussian distribution. The timing noise σ_t arises from a time tagger detection jitter, SNSPD rise time jitter, and an electric noise component σ_{v} on the falling slope of the detector response that is measured as an additional timing jitter. We can neglect the time tagger jitter and the SNSPD rise time jitter as they are much smaller compared to the jitter from the electric noise. Following a simple error propagation, we can relate both values via

$$\sigma_t = \sigma_v \left| \frac{\mathrm{d}}{\mathrm{d}t} nAe^{-t/\tau} \Big|_{t=t_{\text{over thres}}(n)} \right| = \frac{\sigma_v a_0}{\tau} \,. \tag{3.36}$$

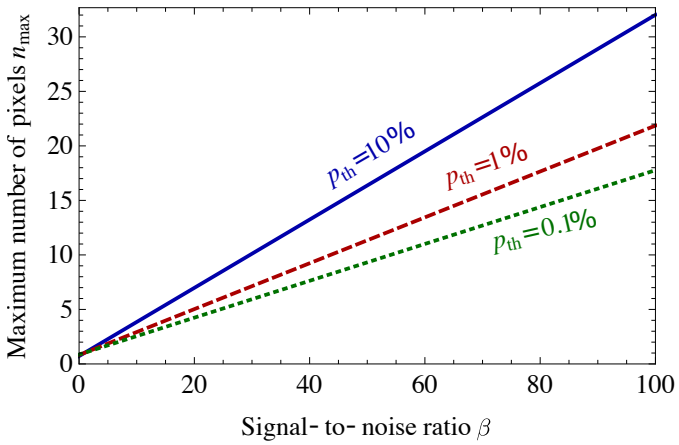

Figure 3.24 – Maximum pixel number as a function of the signal-to-noise value β. See text for further details. Reprinted from [165]. ©2020 Optical Society of America.

This expression does not depend on n due to the exponential decay of the voltage response. If we consider a detector with n_{max} bins, we will consider the misidentified click probability of the second last event $n_{\text{max}-1}$ as a worst-case scenario (clicks from n_{max} and $n_{\text{max}-2}$ contribute). We will evaluate the outcome at a threshold $A_0 = A - \sigma_v$, which has shown to be a suitable value. In addition, we will define a signal to noise value β as

$$\beta = A/\sigma_v \, . \tag{3.37}$$

If we assume that the click probability of having n simultaneous detection events is constant and that the error from all other events $n_{\text{max}-3,4,\ldots}$ does not contribute, we can find a solution using error functions (see [165]). More importantly, we can approximate the solution with a Gaussian distribution

$$p_{\text{misidentified click},n_{\text{max}-1}} \approx \frac{2}{3} e^{-\frac{(\beta-1)^2}{2\varsigma^2}} \, , \tag{3.38}$$

where the width $\varsigma = a + b n_{\text{max}}$, and $a = -1.69$ and $b = 1.64$ are numerically determined constants. If we allow for a specific error value p_{th} we can calculate the maximum bin number n_{max} in dependence on the signal to noise value

$$n_{\text{max}} \approx \frac{1}{b} \left(\frac{\beta - 1}{\sqrt{2 \ln \left[\frac{2}{3 p_{\text{th}}} \right]}} - a \right) \, , \tag{3.39}$$

which is shown in Fig. 3.24 for three threshold values. This means that for current signal-to-noise ratios of up to 55 [166] this readout method can handle up to twelve pixels with a 1% error. Slight modifications in our readout scheme, such as a box-car averaging unit, can increase this number further.

3.7 Conclusion

In this chapter, we have seen how photon-number resolved measurements can be realized. The established idea of multiplexing to achieve photon-number-resolved measurements was discussed in detail and extended to measure very bright states. We have reported on a large 2x128-bin TMD unit that still features very high transmission values of over 81% and no intrinsic cross-talk between detection bins. We have investigated non-classical signatures of up to ten photons spread over up to 64 modes with correlation functions. To investigate even brighter optical states, a high dynamic range detector was described that utilizes the saturation regime in order to extend the dynamic range to 123 dB from 10^{-7} photons/s to $2.5 \cdot 10^{5}$ photons/s. At the upper end of the dynamic range, this detector can withstand a few nW of average power, making it directly comparable to typical power meters. We have shown that this enables a direct calibration procedure of single-photon detectors. Finally, we discussed a single-channel electrical readout scheme for multi-pixel SNSPD detectors, which can enable direct (pseudo) photon-number-resolved measurements in the future.

The shown extension of the dynamic range makes it possible to characterize quantum states in a new parameter regime. These very bright states are highly interesting for sensing applications. In addition, we have shown that new methods, such as the direct calibration of single-photon detectors, go hand in hand with the extended dynamic range. In the same sense, our methods also enable us to quantify very bright classical light beams, if a future quantum standard for optical intensities is available. In the next chapter, we will use the discussed photon-number-resolved measurements for quantum state characterization.

CHAPTER 4

Quantum state tomography

Contents

In this chapter, we will finally combine previously presented techniques on source engineering and photon counting to investigate quantum states. In contrast to classical state characterizations, reconstructing a quantum state from a single measurement is fundamentally prohibited. Therefore, we have to investigate a set of identical states (ensemble) from different 'directions' to determine the whole state. This approach is also widely used in the classical domain, although not fundamentally required. For example, in image tomography, the shape of a 3D object is calculated from its 2D projections. Analogous to this method, the process of quantum state reconstruction is known as quantum state tomography.

If we have characterized our quantum state, it is common to either describe it as a density matrix in the Fock basis or as a quasi-probability distribution. These approaches can be directly connected to the DV or CV picture, respectively, and a link between both worlds is for example given in [11]. Interestingly, interpreting photon-number-resolved measurements is often more intuitive with respect to the phase-space picture (especially if phases need to be determined), establishing a natural connection between both interpretations. In the following, we will describe three main projects and show how the CV-DV synergy effects help to measure quantum states with single-photon detectors. We will start with two new methods that are based on overlap variations and incomplete phase-space measurements. In the second part of this chapter, we will focus on a new scheme that uses a dedicated laser for the characterization and revisit ultrafast laser properties that are relevant in this context. Before introducing new methods, we will briefly revisit some basics on phase-space functions.

4.1 Background

4.1.1 Theoretical considerations of phase-space distributions

Phase-space distributions are very helpful to describe a quantum state with all its properties. Many interesting features, such as non-classicality, can be directly identified in this description. To derive the first phase-space representation, we can decompose an arbitrary state ρ in the overcomplete basis of coherent states $|\alpha\rangle$

$$\rho = \int d^2\alpha \, P(\alpha) \, |\alpha\rangle\langle\alpha| \ . \tag{4.1}$$

This function $P(\alpha)$ is one example of a phase-space distribution and known as the Glauber-Sudarshan P representation of a quantum state. Representing quantum states in this way has a direct link to classical probability theory and helps for example to compute expectation values of operators [11]

$$\mathrm{tr}\left[\rho(\hat{a}^\dagger)^n(\hat{a})^m\right] = \int d^2\alpha\, P(\alpha)(\alpha^*)^n\alpha^m \,. \tag{4.2}$$

In contrast to a classical theory, the probability function can have negative values (and is therefore called a quasiprobability distribution). Equation 4.2 also reveals a major difficulty associated with this approach. On the left side of the equation, we cannot change the ordering of the operators $\hat{a}^\dagger$ and $\hat{a}$ due to their commutation relation $[\hat{a}, \hat{a}^\dagger] = 1$. On the right side of the equation, however, the complex numbers α and α^* can commute. In order to account for this problem and to expand previous works with different orderings, *Cahill and Glauber* introduced a generalized phase-space function $\mathcal{W}(\alpha, s)$ of a state ρ in 1969 [11, 167]

$$\mathcal{W}(\alpha, s) = \mathrm{tr}\left[\rho\frac{2}{\pi(1-s)}\hat{D}(\alpha)\left(\frac{s+1}{s-1}\right)^{\hat{n}}\hat{D}^\dagger(\alpha)\right] \,, \tag{4.3}$$

with an additional factor of $\frac{1}{\pi}$ for normalization compared to the original equation e.g. [168]. Here the parameter $s \in [-1, 1]$ can account for different operator orderings. For the case $s = 1$, we find the already discussed Glauber-Sudarshan P-function $P(\alpha) = \mathcal{W}(\alpha, 1)$, where the operators are in normal ordering (all $\hat{a}^\dagger$ to the left). We can also arrange the operators in symmetric ordering or anti-normal ordering. These special cases $s = 0$ and $s = -1$ are known as the Wigner function and Husimi Q-function, respectively.

First, we want to discuss some properties of the Glauber-Sudarshan P-function $P(\alpha)$. Unfortunately, this function is highly singular. We can see from Eq. 4.1 that coherent states have the form of delta distributions. Fock states are even 'sharper' as they can be expressed as derivatives of delta distributions. Despite the lack of intuition, the Glauber-Shudershan P representation is perfectly suited to define non-classicality formally: All states that are positive in all representations (as $|\alpha\rangle\langle\alpha|$ is an overcomplete basis the representation is not unique) are classical states. Non-classical states, on the other hand, have a negative value somewhere.

As a second example, we want to highlight the Wigner function, which was the first phase-space function discussed in the literature [29, 169]. The Wigner function is of practical interest, as it can be directly addressed with homodyne measurements (see Sec. 4.1.2). For example, if we modify Eq. 4.3, we can link the Wigner function to the photon number parity (even photon number contributions minus odd photon number contributions) of the displaced state as

$$W(\alpha) = \frac{2}{\pi}\sum_{n=0}^{\infty}(-1)^n \langle n|\, D(-\alpha)\rho D(\alpha)\, |n\rangle \,. \tag{4.4}$$

Compared to the Glauber-Shudershan P representation, the Wigner function is better 'behaving' as no delta distributions for physical states can occur. We can therefore visualize the Wigner function in a 3D-plot, as shown in Fig. 4.1 for the vacuum state (a) and a squeezed state (b). The squeezed state also shows another discrepancy between the two distributions: Squeezed states

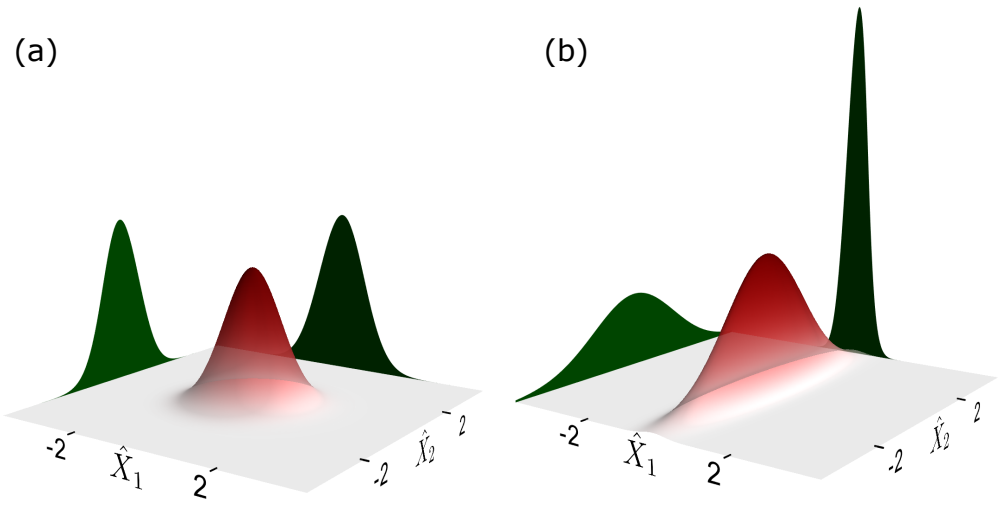

Figure 4.1 – Wigner function of the vacuum (a) and a squeezed state (b). The marginals of the $\hat{X}_1$ and $\hat{X}_2$ quadrature axes are shown in dark-green.

are non-classical but have positive values everywhere. This means that having a negativity is still a sufficient criterion for having a non-classical state, but it is not necessary anymore. Illustrating squeezing, we can also directly see the link to phasor diagrams, as discussed in Sec. 2.4.1. The Wigner function can be understood as a more formal version of these phasor diagrams. We refer to these states as Gaussian states if we can express our quantum state with a double Gaussian function. It has been shown that Gaussian states with Gaussian operations (all operations that map Gaussian states on Gaussian states), are not sufficient for many important applications, such as entanglement distillation [170] and universal quantum computation [171–173]. This can be understood intuitively as Gaussian states can be characterized efficiently in a covariance matrix and a mean value. Therefore these states and operations are easy to simulate classically. For this reason, non-Gaussian states are highly relevant for quantum optical applications. As an example, a single-photon and a two-photon Fock state can be seen in Fig. 4.2.

4.1.2 Measuring phase-space distributions

We have seen that phase-space distributions are a great tool to describe quantum states and investigate their properties. Maybe even more important: These distributions can be accessed experimentally. To achieve this, we always require a second field (local oscillator, LO), which is combined with our state under test (SUT). This LO acts as a reference and enables us to consider our SUT from different 'directions'. A more detailed discussion about the LO can be found in Appendix D. We want to distinguish two measurement schemes depending on the LO mean photon number and detector characteristic, which are known as strong-field homodyning and weak-field homodyning. We will see that these measurements very distinct, as they either produce CV or DV outputs.

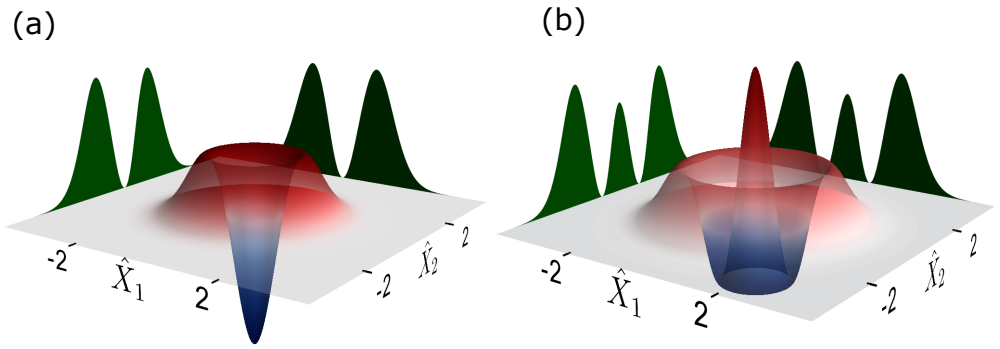

Figure 4.2 – Wigner function of a single-photon (a) and a two-photon state (b). Negative values are shown in blue whereas positive values are indicated in red. The marginals of the $\hat{X}_1$ and $\hat{X}_2$ quadrature axes are shown in dark-green.

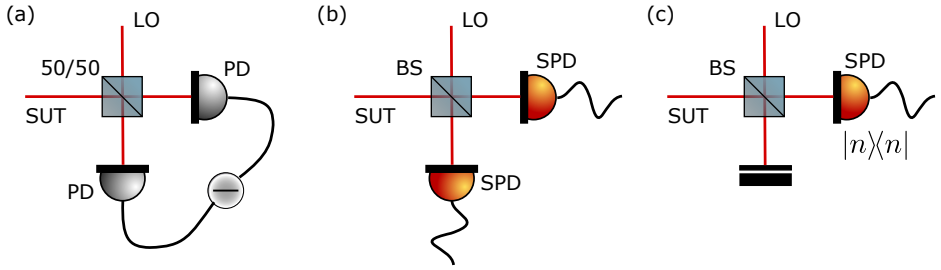

Figure 4.3 – Comparison between strong-field homodyning (a) weak-field homodyning (b) and direct probing (special case of direct probing) (c). A local oscillator (LO) is combined with a state under test (SUT) on a beam splitter. The outgoing field is either detected with pin-photodiodes (PD) or single-photon detectors (SPD). In the direct probing case, a beam splitter with high transmission is used in combination with photon number resolving single photon detectors. See text for further details.

Strong-field homodyning

Strong-field homodyning (SFH), or simply homodyning, is one of the most established techniques for quantum state characterization. In this thesis, we will use the full term strong-field homodyning (SFH) to distinguish it from quantum state characterization with a weak local oscillator and single-photon detectors. SFH consists of a 50/50 beam splitter, where SUT and LO are combined (see Fig. 4.3 (a)). Both output ports from the beam splitter are detected with photodiodes. The resulting photocurrents are finally subtracted, amplified and recorded. To understand the working principle of SFH, we will revisit phasor diagrams introduced in Sec. 2.4.1. These phasor diagrams are intuitively linked to a semi-classical approach, where we split the optical state α into a classical amplitude α_0 with additional quantum fluctuation along the quadrature axes δX

$$\alpha(t) = (\alpha_0 + \delta X_1(t) + \delta X_2(t))\, \mathrm{e}^{i\omega t} \,. \tag{4.5}$$

With this approach and the assumption of a strong local oscillator (neglecting all terms that are not linear in α), we can calculate the photocurrent difference ι_-,which is given by [174]

$$\iota_-(t) \approx 2\alpha_{\mathrm{LO}} \left(\delta X_{1,\mathrm{SUT}}(t)\cos(\phi) + i\delta X_{2,\mathrm{SUT}}\sin(\phi)\right) \ , \tag{4.6}$$

with a relative phase ϕ between SUT and LO. Equation 4.6 reveals some interesting findings:

Firstly, we can see that the photocurrent difference is independent of LO quantum fluctuation. This means that the measured photocurrent variance will only depend on quantum fluctuations resulting from δX_{SUT}. We therefore have a tool to investigate the quantum noise properties of the SUT. Historically, showing the reduced noise characteristics of a squeezed state was the first application for SFH in the quantum regime [175].

Secondly, Eq. 4.6 shows that the measured quantum fluctuations δX_{SUT} scale linearly with the LO amplitude. Here another reason why SFH requires a bright LO becomes apparent. All photodiodes will produce a so-called dark current, which can be interpreted as a constant noise level. In order to see any quantum fluctuations, they need to be 'amplified' by the LO to surpass the photodiode noise floor.

Finally, we can see that the photocurrent difference can be interpreted as a projective measurement of the SUT on the quadrature axes. By changing the relative phase ϕ we can perform a full scan of all quadrature projections[1]. This scan is sufficient for a full quantum state characterization, which has been shown in 1989 [176], four years after the demonstration of squeezed light. The transformation which is required to convert the SFH results to a Wigner function is known as a Radon transformation. Four years after this theoretical finding, quantum state tomography was shown experimentally [177]. SFH is of special interest because the projection along the quadrature axes is a natural measurement basis for squeezed states. This means that squeezed light can be directly identified with SFH without any further processing [175, 178]. Therefore, SFH is also the primary example of a CV measurement as it can measure quadrature values introduced in Sec. 2.4.1.

Weak-field homodyning

A more natural choice of quantum state characterization from the DV perspective is homodyning with a weak coherent state $|\alpha| \sim 1$ as a local oscillator and single-photon detectors (see Fig. 4.3 (b)). We will refer to this characterization scheme as weak-field homodyning (WFH). In contrast to SFH, WFH is a non-Gaussian measure due to the single-photon detection. This means, for example, that we can directly measure negativities of the Wigner function without applying any reconstruction algorithm. WFH characterization techniques were proposed in the 1990s after the development of SFH [168, 179, 180], although some basic ideas can be found earlier [181, 182]. One major challenge of WFH was the lack of high efficiency single-photon detectors, despite the fact that additional losses can be incorporated in the detection scheme [168]. Nowadays, with the advent of TES detectors, highly efficient photon-number-resolving detectors are available. Compared to photodiodes, superconducting detectors still face some additional challenges due to their cryogenic cooling and single-mode fiber coupling, which makes SFH for the moment more attractive from the application side (especially if squeezed light is involved [162]). However, a wide class of important problems cannot be solved in the Gaussian

[1] Strictly speaking, these are the marginal distributions $p(x) = \int dy\, p(x,y)$.

framework [170], leaving WFH as an interesting ingredient.

One specific configuration of WFH should be highlighted because it can link photon-number measurements and the Wigner function in a very intuitive way. We have seen in Eq. 4.4 that the photon-number parity is directly linked to the value of the Wigner function at the origin of the phase space distribution. As the photon-number parity needs to be evaluated, photon-number-resolving detectors are required. Obviously, it is not sufficient to only characterize the Wigner function at a single point. However, with a displacement operation, we can pointwise address the full Wigner function, as suggested by *Banaszek and Wodkiewicz* in 1996 [180]. Fortunately, a displacement operation can be easily implemented with a highly transmissive beam splitter, as shown in Fig. 4.3 (c). Due to this pointwise sampling of the Wigner function, this technique is called direct probing (DP). Arguably the first implementation of DP has been shown in [183], but without photon number resolution and with classical states (also used in [184]). With the development of time-multiplexing [23, 25] (also see Sec. 3.2), measuring the photon number distribution was possible, which led to the first complete quantum experimental realization by *Laiho et al.* [185]. We will show measurements for both, the DP and the balanced WFH configuration in the next sections. To start with, we will introduce a new method for quantum tomography, which is based on overlap variations that reveal a major difference between SFH and WFH.

4.2 Tomography by the overlap

Tomography schemes, as discussed before, always require a set of non-identical measurements to gain knowledge about the full quantum state, i.e. we have to vary at least one parameter between measurements. On the one hand, we have SFH, where the phase of the LO is changed to perform a full quantum state reconstruction. On the other hand, we can consider WFH to determine the SUT. For WFH different approaches including the variation of losses [186–190], amplitude [168, 179, 180, 183, 185] and thermal states [191] have been shown.

Here we show a new WFH scheme based on varying the overlap between the SUT and LO modes. The effect of overlap variations are very different for SFH and WFH approaches. In SFH non-overlapping parts are not 'amplified' by the LO and therefore not detected, which can be considered as loss. To prevent these effective measurement losses, it is critical to match the LO to the SUT [192] in all degrees of freedom (polarization, time and frequency spectrum, spatial mode). In WFH, however, all optical fields, whether overlapping or not, will be detected, which simplifies the characterization of multi-mode states [183]. Without loss of generality, we can always decompose our SUT and LO modes into an overlapping part and a non-overlapping part [193]. The single-photon detector therefore sees a convolution of the overlapping (and therefore interfering) and the non-interfering part. We will use this result as a new tool for quantum state reconstruction.

Measuring non-overlapping fields is not only a new method for investigating the quantum state but also a tool for characterizing the mode structure. Knowing the mode shape of a quantum state in addition to the photon number characteristics is an important factor [194, 195] that can, for example, limit the complexity of boson sampling [196, 197]. Still, single-mode states are often an implicit assumption in quantum tomography although the generation of quantum

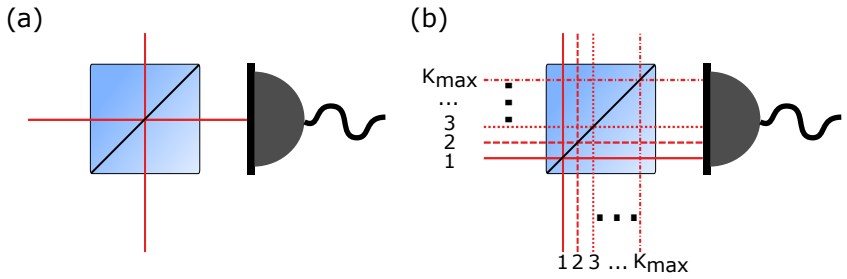

Figure 4.4 – Measurement scheme for the simplest single-mode case (a) of tomography by the overlap. LO and SUT are combined on a beam splitter. One of the outgoing modes is detected with a binary detector. The scheme can be extended to the multimode regime, where $K_{\max}$ modes are entering the beam splitter (b). Reprinted from [214]. ©2018 IOP Publishing.

states in various mode shapes has been shown [198–211]. SFH reconstruction techniques have been shown e.g. in [212]; however, we will show that the intrinsic mode insensitivity of WFH is an advantage. Overlap variations have previously been used for characterizing single-photon states [213]. We will generalize this idea and demonstrate, for example, that the overlap modulus of an arbitrary state can be determined, in combination with a detector efficiency variation [194], beyond the scope of SFH. In addition, we will also demonstrate a trade-off between investigating the underlying mode structure and the quantum state itself. The experiment is done in a resource-efficient way by employing only a single binary detector. The content of this section was published in [214].

4.2.1 Measurement scheme

The simplest overlap measurement scheme can be realized with a beam splitter to combine the SUT and LO and a binary detector, as shown in Fig. 4.4. To start with, we will consider a measurement where the SUT and LO can be treated as single-mode fields. In this case, we can write the quantum state as a function of broadband creation $a_x^\dagger$ and annihilation operators a_x, as described in Sec. 2.1.3

$$a_x = \int_0^\infty d\omega \, f_x(\omega) a_x(\omega) \, , \tag{4.7}$$

where x denotes either the SUT (s), or the LO[2]. We will always refer to these broadband operators if no explicit frequency dependence is written. In general these two broadband modes will

[2]Single-mode state does not mean that the quantum state consists of a single monochromatic frequency. Rather, it implies that the mode can be written as a coherent superposition of these monochromatic frequencies.

be non-identical, so we can define an overlap ϕ between both states

$$\phi = \int_0^\infty d\omega \, f_s(\omega) f_{\mathrm{LO}}^*(\omega) \, . \tag{4.8}$$

We will assume that both the beam splitter with transmission T and the detector will act frequency-independently such that we can write the "no-click" probability c_0 as

$$c_0 = \mathrm{tr}\left[: \exp(-T^2\eta(a_s^\dagger a_s + \mu^2 a_{\mathrm{LO}}^\dagger a_{\mathrm{LO}} + \mu\phi a_s^\dagger a_{\mathrm{LO}} + \mu\phi^* a_{\mathrm{LO}}^\dagger a_s)) : \rho_{\mathrm{LO}}\rho_s \right] \, , \tag{4.9}$$

where η is the detection efficiency, $\mu = \sqrt{(1-T)/T}$ and :: denotes operator normal ordering. For the extreme case of no overlap $\phi = 0$ we can directly see that Eq. 4.9 simplifies to the product of having no counts from the LO and the SUT, $c_0 = c_{0,s}c_{0,\mathrm{LO}}$. In general ($\phi \neq 0$), however, both fields will interfere and c_0 will also depend on the relative phase between SUT and LO.

To simplify Eq. 4.9 further we will decompose both states in the coherent state basis as shown in Eq. 4.1. However, here we will approximate the state with a discrete set as common in data pattern tomography schemes [215–219]

$$\rho_x = \sum_j c_{j,x} |\alpha_j\rangle\langle\alpha_j| . \tag{4.10}$$

Therefore we can rewrite the no-click probability c_0 as

$$c_0 = \sum_{ij} c_{j,s}c_{i,\mathrm{LO}} \exp\left(-T^2\eta(|\alpha_j|^2 + \mu^2|\beta_i|^2 + \mu\phi\alpha_j^*\beta_i + \mu\phi^*\beta_i^*\alpha_j)\right) \, . \tag{4.11}$$

This equation shows the general idea behind overlap tomography: We can either infer the overlap if both input states are known, or we can characterize the SUT with a controlled variation of the overlap ϕ. We will discuss these options in the following.

4.2.1.1 Inferring the overlap

As common for WFH, we will assume that the LO is a coherent state $|\beta\rangle$. We can therefore simplify Eq. 4.11 as

$$c_0 = \langle\bar{\beta}|\bar{\rho}_s|\bar{\beta}\rangle \exp\left(-(1-T^2)\eta|\beta|^2(1-|\phi|^2)\right) , \tag{4.12}$$

with the density matrix of the damped signal $\bar{\rho}_s$ defined as

$$\bar{\rho}_s = \sum_j c_{j,s} |\sqrt{\eta}T\alpha_j\rangle\langle\sqrt{\eta}T\alpha_j| \, , \tag{4.13}$$

and a damped amplitude of the LO $\bar{\beta} = -\sqrt{\eta(1-T^2)}\phi^*\beta$. If the phase between LO and SUT is varied during the measurement, we will calculate the phase averaged version instead

$$c_0 = \sum_{n=0}^{\infty} p_n \frac{\eta^n |\phi\beta|^{2n}(1-T^2)^n}{n!} \exp\left(-(1-T^2)\eta|\beta|^2\right) , \tag{4.14}$$

where p_n is the probability of having n photons in the SUT. Most importantly, the zero-click probability c_0 is monotonous in the overlap modulus, which means that we can invert the function. We can therefore measure the overlap modulus for an arbitrary state with a known photon number distribution p_n in a single measurement. In addition, we can also determine the photon number distribution by simply changing the detector efficiency to extract p_n and overlap, as proposed in [194]. This remarkable result is not possible for SFH as both the overlapping and the non-overlapping parts are required for these combined measurements.

4.2.1.2 Inferring the mode profile

We can also use the same considerations to determine the SUT mode profile. To do so, the LO is prepared in various known shapes, and the overlap value is measured. For example, we can introduce a simple time-delay between LO and SUT. The resulting overlap is then connected to the mode profiles via a Fourier transformation

$$\phi(\delta t) = \int d\omega f_s(\omega) f^*_{\mathrm{LO}}(\omega) \exp\{-i\omega\delta t\}, \tag{4.15}$$

with a time delay δt. Interestingly we can also extract information about the SUT mode, even though we only measure the overlap modulus. In this case, the equation can be directly linked to the phase-retrieval problem, a well-studied task in image reconstruction (phase is extracted from an intensity measurement) [220]. To perform the mode reconstruction, it is often advantageous to decompose the modes into a superposition of basis states, e.g. Hermite-Gaussian functions in the case of SPDC [211].

4.2.1.3 Inferring the signal state

Complementing the modal analysis, we can also characterize the quantum state itself. We can rewrite Eq. 4.12 in terms of the Husimi Q-function $Q(\alpha, \alpha^*)$ for the SUT

$$c_0 = \frac{\exp\left(-(1-T^2)\eta|\beta|^2(1-|\phi|^2)\right)}{1-\eta T^2} \int d^2\alpha \; e^{-\sigma|\alpha-\bar{\beta}|^2} Q(\alpha, \alpha^*) , \tag{4.16}$$

with $\sigma = \frac{\eta T^2}{1-\eta T^2}$. This equation generalizes the results shown in [168] for non-ideal overlap values and has the shape of a Weierstrass transformation. In order to perform state tomography Eq. 4.16 needs to be invertible. We have proven this property in Appendix A in [214].

Still, performing the full inversion can be a complex task, especially with respect to error propagation. Therefore, we will follow an alternative approach by investigating the Q-function

in the Fock basis

$$Q(\alpha,\alpha^*) = \frac{1}{\pi} e^{-|\alpha|^2} \sum_{n,m\geq 0} \rho_{n,m} \frac{(\alpha^*)^n \alpha^m}{\sqrt{n!m!}} \,, \tag{4.17}$$

where $\rho_{n,m}$ defines the matrix elements of the SUT in the Fock basis. Therefore the no-click probability is given by

$$c_0 = \exp\left(-\eta(1-T^2)|\beta|^2\right) \underbrace{\sum_{n,m\geq 0} \frac{\rho_{n,m}}{\sqrt{n!m!}} \exp\left(-\frac{|y|^2}{1+\sigma}\right) \partial_y^n \partial_{y^*}^m \exp\left(\frac{|y|^2}{1+\sigma}\right)\Big|_{y=\sigma\bar{\beta}}}_{f(\bar{\beta},\bar{\beta}^*)} \,. \tag{4.18}$$

Again, we will assume the SUT occupies a finite-dimensional subspace such that we can truncate the Fock space. In this case, a finite number of $\bar{\beta}$ is sufficient for state reconstruction, as we can always approximate $f(\bar{\beta},\bar{\beta}^*)$ with Lagrange polynomials and therefore determine the Q-function.

Finally we can directly extract the matrix coefficients $\rho_{n,m}$ with established techniques involving least-square [216, 219] or maximium-likelihood methods [194].

4.2.1.4 Comparison to amplitude variation

As a summary of the theoretical discussion, we want to compare our tomography overlap scheme with amplitude-modulated WFH. As an example, we can consider a case where both SUT $|\alpha\rangle$ and LO $|\beta\rangle$ are coherent states. Therefore we can rewrite Eq. 4.11 in a logarithmic form

$$\ln c_0 = -T^2\eta\left(|\alpha|^2 + \mu^2|\beta|^2 + \mu\phi\alpha^*\beta + \mu\phi^*\beta^*\alpha\right) \,. \tag{4.19}$$

We can directly see that the logarithmic no-click probability $\ln c_0$ scales linearly with overlap ϕ and quadratically with coherent state strength β. Therefore we cannot find a set $\{\beta\}$ that reproduces an overlap variation without knowing α. This shows that amplitude variations and overlap variations are fundamenntally different. In addition, it can be shown that the Fisher information between these two measurements is indeed different [214].

4.2.2 Experimental setup

In the following, we want to compare our theoretical findings with experimental data. The measurement setup is shown in Fig. 4.5. Light from an OPO system is frequency doubled, spectrally shaped with a 4f setup and used for pumping a type-II PDC process in a periodically poled KTP waveguide. Both PDC polarizations are spectrally filtered with a bandpass filter. In combination with the 4f line, this enables the generation of a spectrally decorrelated state at 1550 nm. The idler beam (bottom beam path) is split on a 50/50 beam splitter for spatial multiplexing. A tap-off from the OPO system is used to generate the LO. In order to match frequency shape and spectral phase of the LO to the signal (from fiber dispersion), we use a commercial programmable frequency shaper (Finisar Waveshaper). After frequency shaping, the LO is attenuated. The order of frequency shaping and attenuation cannot be interchanged as

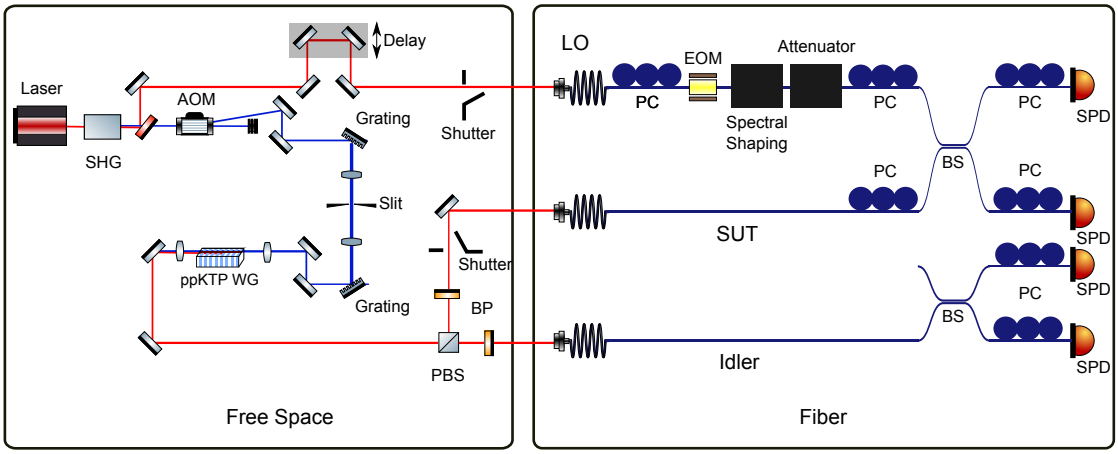

Figure 4.5 – Setup for performing state tomography by the overlap. Light from a 1550 nm OPO is frequency doubled (SHG) and used for pumping a type-II PDC process in a periodically poled KTP waveguide (PPKTP). The PDC modes are separated with a polarizing beam splitter (PBS) and spectrally filtered (BP) before fiber coupling. A tap-off from the OPO is used as a LO and spectrally shaped with a Finisar Waveshaper before attenuation. The LO and SUT/signal are combined on a fiber 50/50 beam splitter (BS). The idler polarization is also split on a 50/50 beam splitter for spatial multiplexing. Polarization controllers (PC) are used to optimize efficiencies, while an acousto-optic modulator (AOM) and an electro-optic modulator (EOM) are used to lower the laser repetition rate. Finally, all fields are measured with single-photon detectors (SPD).

the Finisar Waveshaper emits light from a calibration lamp through the output fiber. Signal and LO are combined on a second 50/50 beam splitter. Finally, all beam splitter output modes are detected with SNSPDs. To account for the detector dead time, the laser repetition rate is reduced with an acousto-optic modulator (AOM) and an electro-optic modulator (EOM) to 1 MHz. The timing offset between the LO and the signal can be controlled with a free-space optical delay.

For the measurement 81 delay settings with an acquisition time of 150 s each were recorded. Between the measurements, we used automated shutters for calibration purposes and to account for drifts between different delay settings. For example, by blocking the LO beam path (top shutter), we investigate the detection efficiency with the Klyshko method [221]. If the PDC beam is blocked instead, we can characterize the beam path with the calibrated LO, revealing a slight beam splitter asymmetry of 43.6/56.4. We can also investigate the maximal mode overlap by interfering a heralded single photon with a coherent state similar to a Hong-Ou-Mandel interference [45] [3]. For all measurements the LO coherent state had a mean photon number of 0.19.

[3] Note that even for perfect overlap non-unit visibility can be seen due to the coherent state photon number distribution [193]

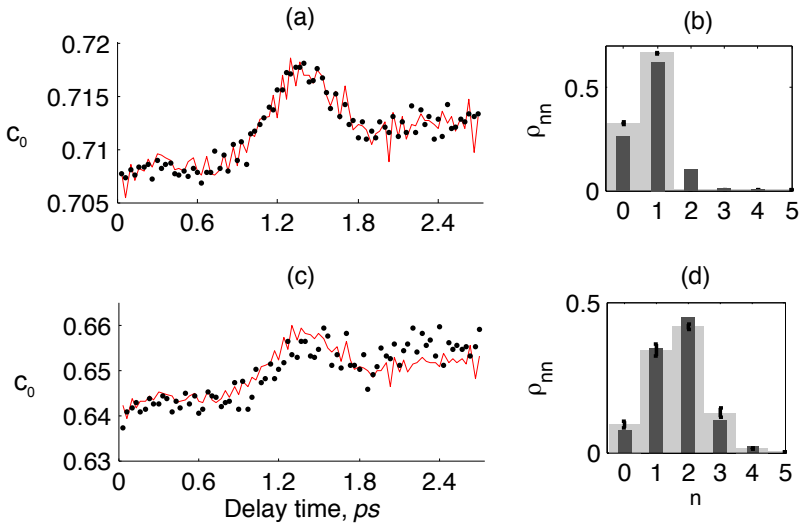

Figure 4.6 – Experimental data for measuring the photon number distribution by varying the overlap. Zero-click probability as a function of the LO time delay for a heralded one-click (a) and two-click (c) event. Black dots show experimental data, whereas the red line represents the theoretical fit. The reconstructed photon number distribution ρ_{nn} can be seen in (b) and (d) in light grey. Narrow dark grey bars show the expected photon number distribution calculated from measured experimental parameters. All measurements are phase averaged. Reprinted from [214]. ©2018 IOP Publishing.

4.2.3 Results

As a first step, we want to determine the photon number distribution of a heralded one- and two-click state. Figure 4.6 (a,c) shows the zero-click probability c_0 as a function of the LO time delay. The probability peak around 1.4 ps, where SUT and LO are interfering, can be seen clearly in the raw data. During the data acquisition, the zero-click probability increased due to coupling drifts, which were probably caused by temperature variations in the lab. These drifts were monitored, using the reference measurements, and accounted for in the data analysis. Based on a least squares method with linear constraints the photon number distributions were reconstructed using Eq. 4.11 and Eq. 4.14 (see Fig. 4.6 (b,d) in light grey). Error bars are based on a data bootstrapping technique. The reconstructed photon number probabilities are compared to the expected photon number probabilities (smaller, black bars) based on the measured experimental parameters (efficiency after the combining beam splitter $\eta = 0.59$ and a squeezing value of $r = 0.382$). Both measurements show good agreement between the overlap tomography and the expected values. Higher-order photon numbers are caused by rather strong squeezing values in combination with optical losses in the heralding arm.

We can also determine the state overlap from a known SUT, as shown in Sec. 4.2.1.1. Figure 4.7 shows the inferred overlap modulus for different LO delays. The expected overlap is

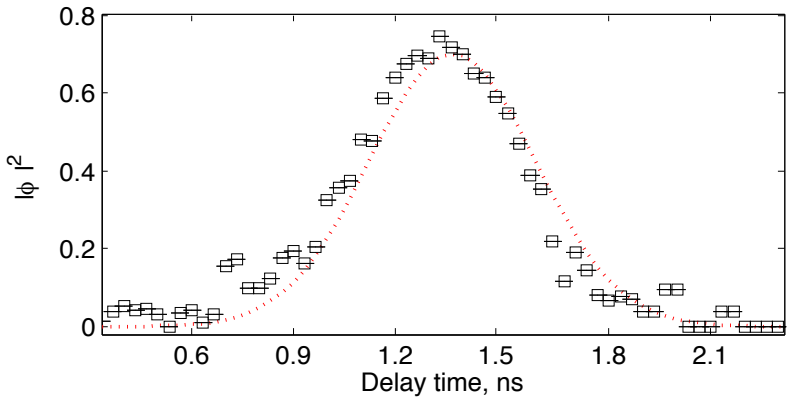

Figure 4.7 – Measured overlap values for a known quantum state (squares) as a function of the LO time delay. In comparison, the expected overlap is shown as a red dotted line. Statistical measurement uncertainties are small compared to the size of the data symbols. Reprinted from [214]. ©2018 IOP Publishing.

shown as a red dotted line, which is in good agreement with the estimated overlap. Using overlap tomography, we have therefore shown that we can either determine the SUT or the overlap modulus.

4.2.4 Multimode description

Up to now, we have only considered single-mode fields for the SUT and the LO that have an overlap ϕ. In the following, we want to generalize our results to multimode fields. We consider the broadband operators before ($a^\dagger_{l,k}$) and after ($b^\dagger_{l,k}$) the combining beam splitter, where $l = 1, 2$ labels the two input (output) modes and $k = 1, \ldots, K_{\text{max}}$ the spectral modes. The input-output relation is given by a unitary matrix U

$$b^\dagger_{l,k} = \sum_{j=1,2} U_{l,j} a^\dagger_{j,k} \,, \tag{4.20}$$

or in matrix notation $\mathbf{b}^\dagger = (U \otimes I)\mathbf{a}^\dagger$ with the K_{max}-dimensional identity matrix I and $\mathbf{a} = (\mathbf{a}_1, \mathbf{a}_2)$ with $\mathbf{a}_l = (a_{l,1}, \ldots, a_{l,K_{\text{max}}})$. We can write the two states $\rho^{(l)}$ that enter the beam splitter in the Fock basis as

$$\rho^{(l)} = \sum_{\mathbf{n},\mathbf{m}\geq 0} \rho^{(l)}_{\mathbf{n},\mathbf{m}} |\mathbf{n}\rangle\langle\mathbf{m}|, \quad |\mathbf{n}\rangle \equiv \prod_{k=1}^{K_{\text{max}}} \frac{\left(a^\dagger_{lk}\right)^{n_k}}{\sqrt{n_k!}} |0\rangle \,. \tag{4.21}$$

In this notation, the combined zero-click probability for the two output ports with detection efficiencies η_l is given by

$$\begin{aligned} c_0(\eta_1,\eta_2) &= \mathrm{tr}\left[\rho^{(1)}\otimes\rho^{(2)} : \exp\left(-\sum_{l=1,2}\eta_l\sum_{k=1}^{K_{\max}} b_{l,k}^\dagger b_{l,k}\right) :\right] \\ &= \mathrm{tr}\left[\rho^{(1)}\otimes\rho^{(2)} : \exp\left(-\mathbf{b}\left[\begin{pmatrix}\eta_1 & 0\\ 0 & \eta_2\end{pmatrix}\otimes I\right]\mathbf{b}^\dagger\right) :\right] \\ &= \mathrm{tr}\left[\rho^{(1)}\otimes\rho^{(2)} : \exp\left(-\mathbf{a}\left[U^\dagger\begin{pmatrix}\eta_1 & 0\\ 0 & \eta_2\end{pmatrix}U\otimes I\right]\mathbf{a}^\dagger\right) :\right] . \end{aligned} \tag{4.22}$$

Following the considerations as for the single-mode theory, i.e. writing the SUT as a multimode Husimi Q-function $Q^{(1)}(\boldsymbol{\alpha},\boldsymbol{\alpha}^*)$ and assuming a coherent LO, we can simplify this equation to

$$\begin{aligned} c_0(\eta_1,\eta_2) = \varkappa^{-K_{\max}}\exp\left(-\frac{\eta_1\eta_2}{1-\varkappa}|\boldsymbol{\beta}|^2\right) \\ \int d\mu(\boldsymbol{\alpha})\exp\left(-\frac{1-\varkappa}{\varkappa}\left|\boldsymbol{\alpha}+\frac{(\eta_1-\eta_2)U_{11}U_{21}^*}{1-\varkappa}\boldsymbol{\beta}\right|^2\right)Q^{(1)}(\boldsymbol{\alpha},\boldsymbol{\alpha}^*) , \end{aligned} \tag{4.23}$$

where $\varkappa = 1-\eta_1|U_{11}|^2-\eta_2|U_{21}|^2$, $d\mu(\boldsymbol{\alpha}) = \prod_{k=1}^{K_{\max}} d^2\alpha_k$ and $\boldsymbol{\alpha} = (\alpha_1,\ldots,\alpha_{K_{\max}})$. Equivalent to the single-mode case we can characterize a given SUT $\rho^{(1)}$ with a coherent LO $\rho^{(2)} = |\boldsymbol{\beta}\rangle\langle\boldsymbol{\beta}|$ with only one detector $c_0(\eta_1,0)$ (second detector is treated with zero efficiency). To be more precise Eq. 4.23 is proportional to a multi-dimensional Weierstrass transformation, which allows to perform the inverse transformation.

4.2.5 Conclusion

In summary, we have seen in this section how state tomography can be performed by varying the SUT and LO overlap. We have seen that we can either characterize the quantum state (known overlap) or determine the overlap value (known state) in a single measurement configuration. A simple experimental setup, using an optical delay line and a single binary detector, was built and showed high agreement with our theoretical predictions. This work not only demonstrates a new tool to perform state characterization, it also highlights the difference between SFH and WFH. Because non-overlapping modes of the LO are still visible in a WFH, the overlap modulus can be found for an unknown quantum state. This advantage of WFH is useful for characterizing multimode quantum states or ruling out side-channel attacks in quantum communication [222].

4.3 Incomplete detection of generalized phase-space functions

The verification of non-classicality is one of the main goals for quantum tomography. In this context, generalized phase-space functions, as discussed in Sec. 4.1.1, are very helpful, as non-classicality is connected to negative regions in the quasi-probability distribution. In general, however, specific phase-space representations such as the Wigner function are very susceptible

to experimental imperfections such as loss. For example, the Wigner-negativity of a single-photon state is erased after 50% loss [46]. Therefore investigating the Wigner function of a quantum state under realistic conditions often requires inversion algorithms that account for imperfections [185, 219, 223–225]. Surprisingly, a specific experimental restriction, namely the number of available binary detectors N, can be an advantage for verifying non-classicality. Here we want to investigate the generalized phase-space functions experimentally in the context of detector multiplexing as theoretically proposed by *Luis et al.* [226]. In general, this technique requires phase stability between the SUT and LO. However, as we will investigate phase-symmetric single-photon states, we can lift this constraint. In addition, we will also link the generalized phase-space parameter s with the detection loss η to allow for direct, loss-robust state characterization without the need for inversion algorithms. The content of this section was published in [112].

4.3.1 Theoretical considerations

We have already introduced the generalized phase-space function in Eq. 4.3. This work was further investigated in the context of pseudo-photon number resolution with N binary detectors by *Luis et al.* [226]. The modified generalized phase-space function for N detectors can be expressed as

$$\mathcal{W}_N(\alpha, s) = \frac{2}{\pi(1-s)} \sum_{k=0}^{N} \left(\frac{\eta(1-s)-2}{\eta(1-s)} \right)^k c_k(\alpha) \tag{4.24}$$

with the probability of $c_k(\alpha)$ simultanous detection events at a displacement α and a detection efficiency η [226]. That approximates the generalized phase-space function $\mathcal{W}$ for sufficiently high N. For even numbers of N, a negative value is also a sufficient criterion for having non-classicality. We combine the detection efficiency η and the s-parameter in a new x-parameter [112], to highlight the connection between both values

$$\mathcal{W}_N(\alpha, x) = A \sum_{k=0}^{N} \left(\frac{x-2}{x} \right)^k c_k(\alpha) \, , \tag{4.25}$$

with $x = \eta(1-s)$ and a numerical constant A. This shows that, to some extent, losses can be counteracted by simply increasing the s-parameter, similar to the results shown in [183]. In practice, we will see that efficiency drifts and noise counts during the measurement can significantly increase the uncertainty, which is given by

$$(\Delta\mathcal{W}_N(\alpha, x))^2 = A \sum_{k=0}^{N} \left(\frac{x-2}{x} \right)^{2k} \frac{c_k(\alpha)(1-c_k(\alpha))}{M} \tag{4.26}$$

with a total number of M recorded measurements per recorded displacement α [226]. We can also define the statistical significance of our measured data as [112, 226]

$$\Sigma = \frac{\mathcal{W}_N(\alpha, x)}{\Delta\mathcal{W}_N(\alpha, x)} \, . \tag{4.27}$$

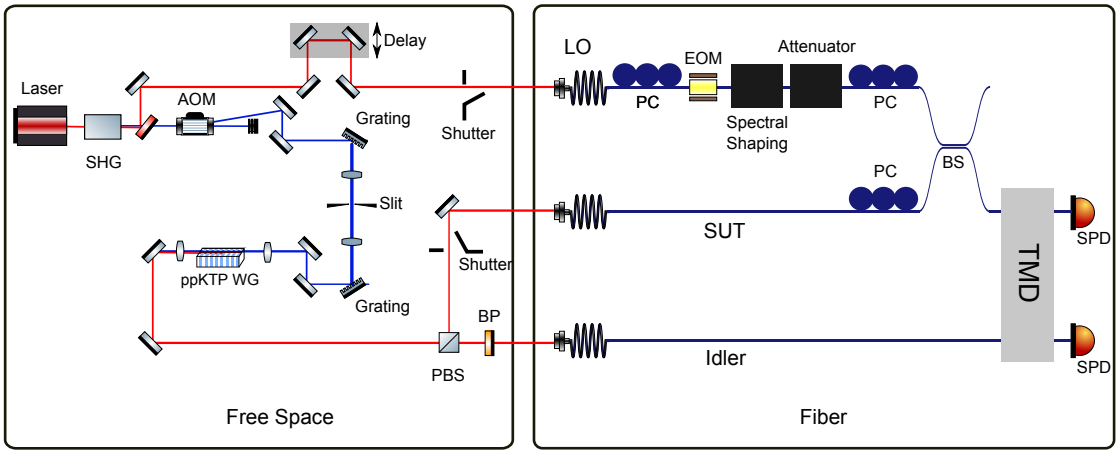

Figure 4.8 – Setup for measuring generalized phase-space functions. Light from a 1550 nm OPO is frequency doubled (SHG) and used for pumping a type-II PDC process in a periodically poled KTP waveguide (PPKTP). Both PDC modes are separated with a polarizing beam splitter (PBS) before fiber coupling. The idler mode is spectrally filtered (BP). A tap-off from the OPO is used as a LO and spectrally shaped with a Finisar Waveshaper before attenuation. The LO and signal/SUT are combined on a highly transmissive fiber beam splitter (BS). The idler polarization and the beam splitter output are coupled to a TMD unit (2x8bins). Polarization controllers (PC) are used to optimize efficiencies, while an acousto-optic modulator (AOM) and an electro-optic modulator (EOM) are used to lower the laser repetition rate. Finally, both TMD output modes are measured with single-photon detectors (SPD).

As a next step, we will now investigate the interplay of the number of detectors N and the generalized x parameter in an experiment.

4.3.2 Experimental results

To experimentally investigate the generalized phase-space function, we perform an experiment similar to the setup we have shown for the overlap tomography. Therefore, we will only describe the modifications between these setups (see Sec. 4.2.2 for further details). A schematic is shown in Fig. 4.8. In contrast to the overlap measurement, we only record data for the maximal overlap value of around 70% between SUT and LO, determined with an interference measurement. Furthermore, both modes are combined on a highly transmissive beam splitter to displace the SUT and to allow for direct sampling of the Wigner function. Using a calibrated variable attenuator, we can change the LO mean photon number. The bandpass filter (BP) in the signal arm is removed to maximize the tomography efficiency. Finally, the light fields are temporally separated in a TMD unit (two inputs with eight time bins each) to allow for pseudo-photon-number resolution. We can combine individual time bins in post-processing to effectively measure with a two-, four- or eight-bin TMD. We calculated a detection efficiency of 21%.

Using the idler mode, we can prepare heralded single-photon states that can be investigated

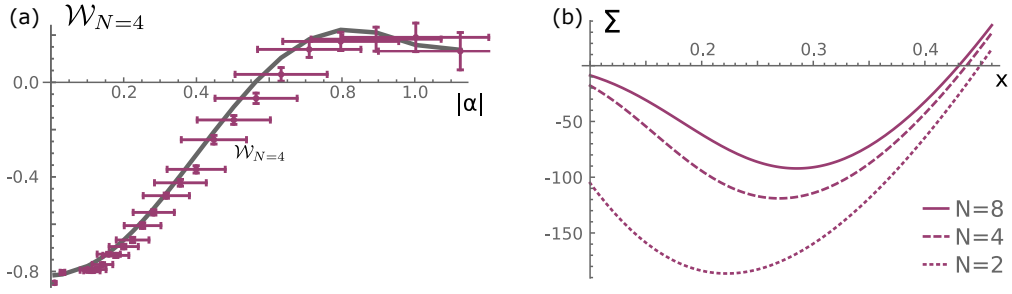

Figure 4.9 – Generalized phase-space function as a function of the LO strength with $x = 0.21$ (a). Calculated significance Σ of the generalized phase-space function as a function of x (b) without any displacements ($\alpha = 0$), as defined in Eq. 4.27. For both figures a heralded single-photon state was investigated. Reprinted from [112]. ©2018 American Physics Society.

with the phase-averaged LO. Figure 4.9 (a) shows such a measured generalized phase-space function as a function of the displacement α and an x value of 0.21. Like the Wigner function of a single-photon Fock state, the maximal negativity is found at the origin. Another important factor for the displaced single-photon state is that the phase-space function also shows positive values for higher α. Without a sufficient overlap between SUT and LO, these positive values for a single-photon state cannot be reached.

In addition we evaluate the significance Σ of the phase-space function in Fig. 4.9 (b) (see Eq. 4.27). Here, we restrict ourselves to the point of the strongest negativity (origin, no displacement $\alpha = 0$). We can see the surprising result that fewer detectors can actually increase the detected significance, in accordance with the predictions from [226]. Besides, for all detector values N an optimal phase-space function x can be found to maximize the significance Σ. This can be understood more intuitively, as low x values show a weak negativity of the phase-space function $\mathcal{W}$, while high x values significantly increase the measurement uncertainty.

4.3.3 Conclusion

In summary, we have shown that the link between pseudo-photon-number-resolved measurements and phase-space functions can be fruitful to determine the quantum state. This link allows us to show a loss-robust method that is able to directly investigate state properties without any state inversion algorithms. In addition, experimental restrictions, such as the number of available binary detectors, can actually be an advantage for measuring non-classicality. This work, therefore, provides a useful new measurement tool to determine non-classical properties under realistic conditions.

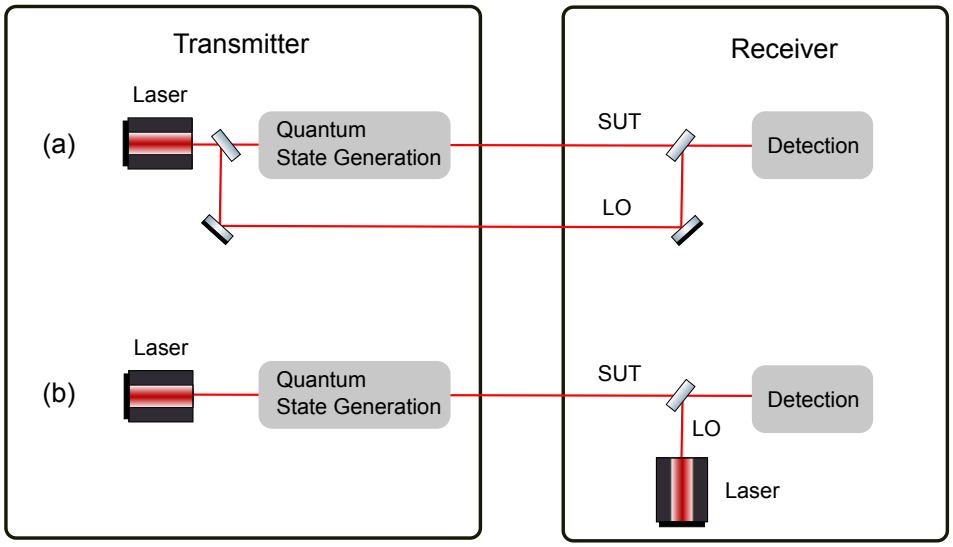

Figure 4.10 – Schematic illustrating the 'truly local' LO generation. (a) Common single-laser tomography scheme where SUT and LO are transmitted to the detection side. (b) New two-laser approach, where the LO is generated at the receiver side.

4.4 Generating a 'truly local' local oscillator

In contrast to the previously shown detection schemes, we will now use a second, dedicated laser for generating the LO. In this section, we will discuss technical details connected to this approach before we apply our new tool for quantum state characterization in Sec. 4.5. The technical difficulties we encountered fostered a strong collaboration with the electrical engineering group of Professor Scheytt from Paderborn University, which resulted in further projects involving the generation of low-noise electrical signals and a proposal for reducing timing jitter measurements with squeezed light. These projects are briefly described in Sec. 4.4.5 and Sec. 4.4.6.

To the best of our knowledge, all described quantum tomography schemes in the literature have in common that the generated quantum state and the local oscillator are derived from the same laser source. This is a huge constraint that we want to address with our new 'truly local' LO approach (see Fig. 4.10). Firstly, a 'truly local' Lo is an important ingredient for CV communication. CV communication is an interesting research topic with increasing attention in recent years [227–230]. One of the advantages is that nowadays classical information is already transmitted using similar tools (quadrature amplitude modulation, QAM e.g. [231]) and therefore promises a rather easy implementation of quantum communication based on existing technologies. Crucial to extract the encoded information in CV communication is an LO that provides a phase reference. In existing CV quantum communication schemes, the LO is transmitted together with the quantum state. However, this reduces the security of the communication, as the LO can be manipulated while being sent to the transmitter. Secondly, sending the LO requires a significant part of the transmission bandwidth, which can be avoided with our approach. Finally,

having a 'truly local' LO implies that more power is available for the quantum state generation, as no tap-off is required. In previous measurement schemes, power constraints were often a limiting factor (e.g. [96, 112])

4.4.1 Why pulsed quantum optics?

Pulsed light emission from a laser system is a key resource for many quantum optical applications. However, it poses severe difficulties for overlapping pulses from spatially separate lasers (especially for femtosecond pulses) compared to continous-wave experiments. We will discuss in the following why these benefits are crucial and justify additional stabilization efforts. Firstly, the peak power of a pulsed laser is much higher than CW light with the same average power. Therefore the resulting non-linearity is higher and, for example, higher squeezing values can be reached (whithout additional restrictions such as thermal induced heatings). Secondly, pulsed light has an intrinsic timing reference that can be used for synchronization. If probabilistic operations have to be carried out, high repetition rate experiments can increase the overall data rate. Successful events will still occur randomly but can only happen in predefined time-windows. Finally, generating high-quality (and single-mode) quantum optical states can be easier with pulsed light, especially for type-II PDC. We have seen in Sec. 2.2.1 that the phase-matching bandwidth of a group-velocity matched type-II process should correspond to the laser pump bandwidth. The phase-matching width is directly connected to the inverse of the crystal length. A narrow phase matching, therefore, corresponds to a long nonlinear crystal. High-quality single-photons from a KTP crystal have been shown up to the picosecond regime, with a crystal length of 2.5 cm [135]. However, with increasing crystal length, fabrication errors become more pronounced [232]. For this reason, we will follow the standard approach in this thesis of using femtosecond pulses with a broad spectral bandwidth to generate high-quality, decorrelated PDC states. Typical laser parameters used for the following tomography experiments are shown in Table 4.1. Before we discuss these experiments further, we will briefly revisit the generation of ultra-short pulses because a profound understanding of the involved parameters is essential for the manipulation.

4.4.2 Passively mode-locked lasers

Just a few years after the demonstration of the first laser [8], the first ideas of generating short laser pulses were discussed [233]. In general, the laser resonator cavity allows a discrete set of frequency modes in the laser cavity. In combination with the optical gain from the laser medium, some subset of these laser modes will be populated. An example laser spectrum, which is often referred to as a frequency comb, can be seen in Fig. 4.11 (a). In order to start pulsed laser operation, all populated frequency modes need to have a specific and fixed phase relation. This process is known as mode-locking and has been shown with active [234] and passive elements [235]. Here we will focus on passive mode-locking as it enables the formation of ultrafast fs pulses. The basic idea of passive mode-locking is that the laser cavity loss is reduced if all laser modes are constructively interfering. In other words, we have an intensity-dependent cavity loss, which favors pulsed operation with high intensities over all other lasing regimes. The formation

Frequency Property	Typical Value	Time Property	Typical Value	Additional Information
f_{rep}: frequency-comb separation	76 MHz	T_{rep}: pulse separation	13.2 ns	$f_{\text{rep}} = \frac{1}{T_{\text{rep}}}$. Defined by the cavity length of the laser
σ_f: comb width	2.5 THz	σ_t: pulse duration	177 fs	Defined mainly by the gain medium and dispersion properties in the cavity
δ: frequency linewidth of a comb tooth	$< 500\,\text{kHz}$	T_c: coherence time	$>2\,\mu$s	The very long time duration T_c is not shown in Fig. 4.11
f_0: center frequency	387 THz (775 nm)	T_0: carrier period	2.6 fs	
f_{CEO}: carrier envelop frequency	$0 \leq f_{\text{CEO}} < f_{\text{rep}}$	ϕ_{CEO}: carrier envelop phase		uncontrolled in this experiment

Table 4.1 – Frequency and corresponding time properties of a mode-locked laser system are compared in this table. Compare Fig. 4.11 for an illustration of these parameters.

of pulses is only possible for a very short time as many frequency modes are involved. To be more specific, the number of frequency modes (spectral width of the laser) is inversely linked to the pulse duration. Similarly, a variety of laser parameters such as laser repetition rate f_{rep}, comb center frequency f_0 or comb linewidth δ can be defined in the spectral domain or the corresponding temporal domain. Figure 4.11 and Table 4.1 show the links between these two sides. It is important to understand these parameters if multiple ultrafast lasers are connected.

One parameter that is of particular interest is called the carrier-envelope offset (CEO) f_{CEO}. We can extrapolate the frequency comb down to lower frequencies, as shown in Fig. 4.11 (a). In general, there will be a non-vanishing offset of the first frequency component, which defines the carrier-envelope offset frequency f_{CEO}. Applying a Fourier transformation of the frequency comb, we can see that a non-zero CEO frequency will cause a varying phase between the pulse envelope and the carrier field (carrier-envelope phase, Fig. 4.11 (b)). CEO properties have been discussed in great detail in classical optics [236–241], especially for very short few-cycle pulses [240]. In this extreme regime, the electric field amplitude depends strongly on the CEO. In order to control the CEO, different techniques have been shown [237, 239]. One common method to extract the CEO phase for stabilization is called an f-2f interferometer. Here one part of the comb at frequency f is frequency doubled using SHG and interfered with an additional frequency component from the comb at $2f$. Obviously, this requires an octave-spanning spectrum of the frequency comb that includes both frequencies f and $2f$. For the lasers here, this condition is not fulfilled. Although frequency broadening techniques such as self-phase modulation have been explored to broaden the spectrum [242], we will not implement CEO stabilization

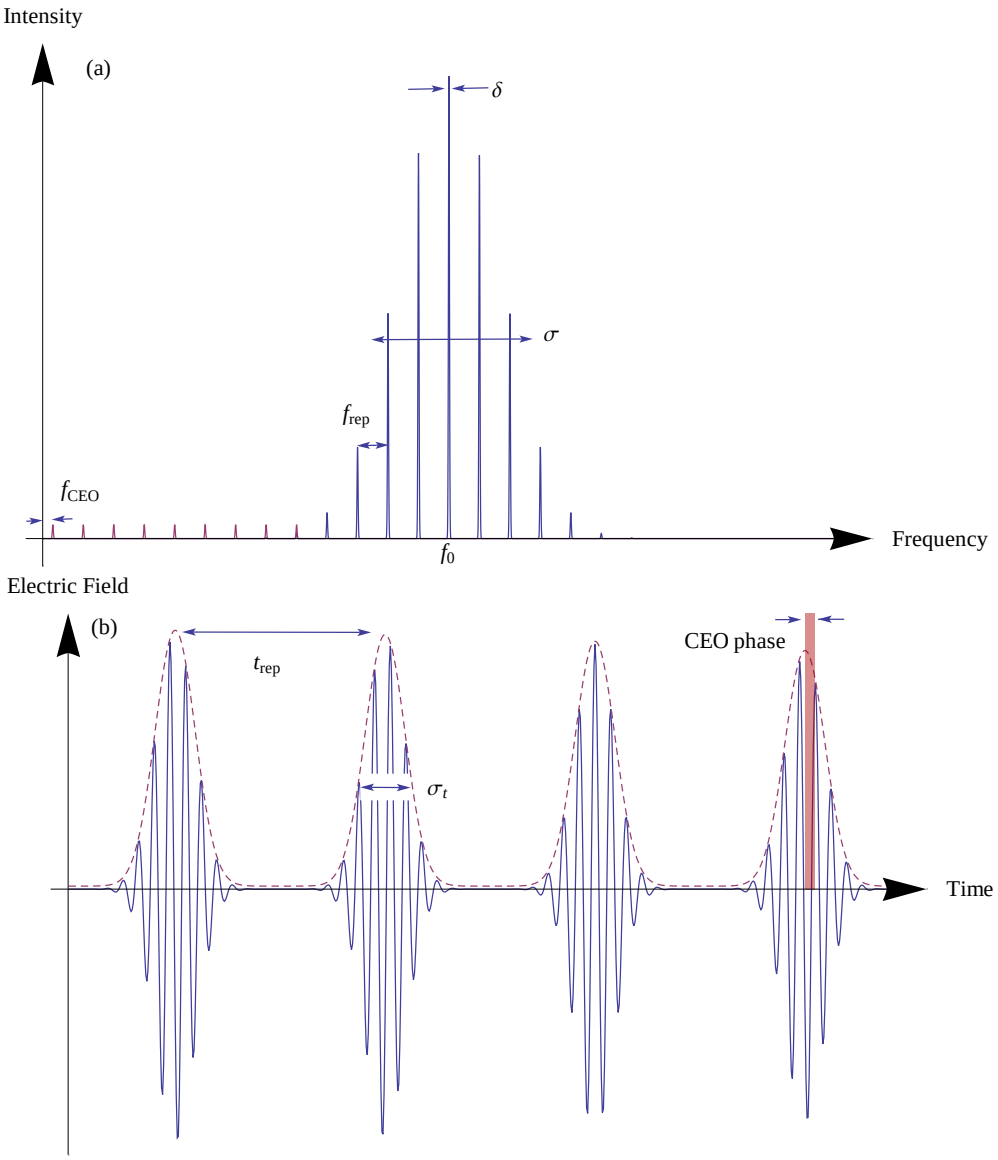

Figure 4.11 – The output light field of a mode-locked laser system can be either described in the frequency domain (a) or in the time domain (b). The frequency spectrum has comb structure with a center frequency f_0, a comb separation f_{rep} and an overall envelop function with a width σ. If the comb is theoretically extended to DC frequency (red) there is, in general, an offset between zero frequency and the first extended comb line. This offset is called f_{CEO}. The electric field is defined by a fast oscillating electric carrier field which is amplitude modulated with a pulsed envelope function (red-dashed). Pulses have a distance of t_{rep} and a width of σ_t. It can be seen that the phase between the carrier field and the envelope function changes from pulse to pulse. This phase drift from one pulse to the next is called the CEO phase. See text and Table 4.1 for further details.

techniques in this thesis due to the additional experimental requirements. Instead, we will discuss a tracking technique to monitor the CEO to compensate for this effect (see Sec. 4.5.2). In our final experiment, we will interfere two passively mode-locked lasers for quantum tomography. Therefore, recording the phase value in combination with the detected photon numbers is important, as the relative phase between LO and SUT will vary from pulse to pulse due to the CEO offset between both lasers. In addition to these fluctuating phases, already achieving a constant overlap between both pulse-envelope functions is challenging. Therefore, we will define noise parameters that are relevant for the characterization as a next step.

4.4.3 Defining noise properties for mode-locked lasers

It is important to characterize the described laser parameters carefully, especially if multiple lasers are combined, as shown in Sec. 4.5. For this purpose we will define some important terms as follows:

- **Phase noise and timing jitter:** For this definition we will only consider the temporal pulse envelope function. This function can have a phase that shifts the absolute position of the pulse train with respect to a global timing reference. Any noise terms that shift the pulse train are referred to a phase noise which cause a timing jitter of individual pulses compared to the timing reference. Timing fluctuations will decrease the overall overlap between two light field and therefore decrease the interference visibility.

- **Optical phase noise:** Phase fluctuations of the optical carrier field will be named optical phase noise. These noise terms, for example, influence the interference pattern of two light field (destructive or constructive interference).

- **Sideband phase noise:** If the pulse train is measured with a fast photodiode, the generated electrical signal in the frequency domain will show a series of peaks spaced by the laser repetition rate. For an ideal configuration these peaks are a series of delta functions. However, noise processes such as phase noise or amplitude noise of the pulse train will broaden these peaks. The shape around these peaks will be referred to as sideband phase noise. We will use the sideband phase noise to find an upper bound of the phase noise value.

After discussing the basics of mode-locked lasers, we are able move forward to the area of laser locking.

4.4.4 Laser locking

As we have seen, laser locking can imply the control of a variety of parameters. We focus here on stabilizing the envelope function of the pulsed laser system. In other words, the repetition rate of two laser systems is stabilized, such that the pulse trains from the lasers have the same spacing. We characterize the individual RMS timing jitter value from each laser system with the help of a signal source analyzer and evaluate the overall jitter performance of the two laser systems based on pulse resolved optical interference measurement.

4.4.4.1 Stabilising the repetition rate

In order to have a high mode overlap between the SUT and the LO, we have to exactly match the pulse spacing (in the time domain) from both lasers. Therefore the cavity length of the mode-locked laser needs to be changed to adjust the repetition rate of the laser system. We use two commercially available stabilization options from Coherent and NKT-Photonics (previously OneFive) for this task. Both systems use different actuators in order to change the cavity length. The Synchrolock-option from Coherent uses a very slow stepper motor for pre-adjusting the cavity length. Then two faster actuators enable tuning of the cavity with a bandwidth of up to 10 kHz. These modulations are fast enough as the main noise contributions result from temperature fluctuations and mirror vibrations. The NKT-Photonics system uses temperature tuning to adjust the cavity length for slow drifts and a piezo element for fast tuning, enabling a stabilization bandwidth of up to 10 kHz. In order to stabilize the repetition rate, a feedback signal is needed for the locking electronics. Therefore some part of the laser beam is sent to a fast photodiode. The resulting electrical signal is compared with a stable reference signal and an error signal is derived, which is fed back to the laser actuators. The working principle is completely analogous to well-known electrical phase locked loops (PLL), which are used to lock to a reference frequency.

Unfortunately, two effects (amplitude noise and repetition rate jitter) can affect the locking mechanism. This problem has been studied in the past and it has been shown that both effects scale differently while going to higher harmonics of the electrical signal [243]. If the amplitude noise is slowly varying compared to the laser repetition rate (which is a valid assumption for passively mode-locked lasers), the amplitude noise is constant for all harmonics. The repetition rate jitter, however, scales quadratically with the harmonics. Therefore the effect of amplitude noise can be suppressed by selecting higher harmonics. The NKT-Photonics origami laser locks on the 40th harmonic at 3.04 GHz, while the Coherent Mira laser locks either on the fundamental frequency at 76 MHz or the 9th harmonic at 684 MHz. Although higher harmonic locking is required to achieve low jitter values, the absolute time position of the pulse train cannot be recovered anymore. In other words, locking to the n-th harmonic randomly selects one of n positions with respect to the fundamental pulse train. Only the Coherent Mira laser can resolve this problem with an additional fundamental lock. Here the laser system initially locks on the fundamental frequency before the harmonic locking is enabled (and finally, the fundamental lock is turned off). This enables locking the pulse train to an absolute position.

4.4.4.2 Direct jitter measurements

Measuring the jitter of the laser pulse envelope function down to the fs level is a non-trivial task. Here we want to convert the optical signal to an electrical signal where measurement equipment is available to determine the phase noise. A perfect optical pulse train in combination with a perfect photodiode would result in a series of delta peaks in the frequecy domain (of the photodiode signal). However, imperfections such as intensity fluctuations or repetition rate variations will broaden these peaks. With the so-called Von der Linde method we can relate this sideband phase noise to a timing fluctuation [243]. The measurement setup is shown in Fig. 4.12. Either a Coherent Mira laser or an NKT Photonics Origami laser is investigated.

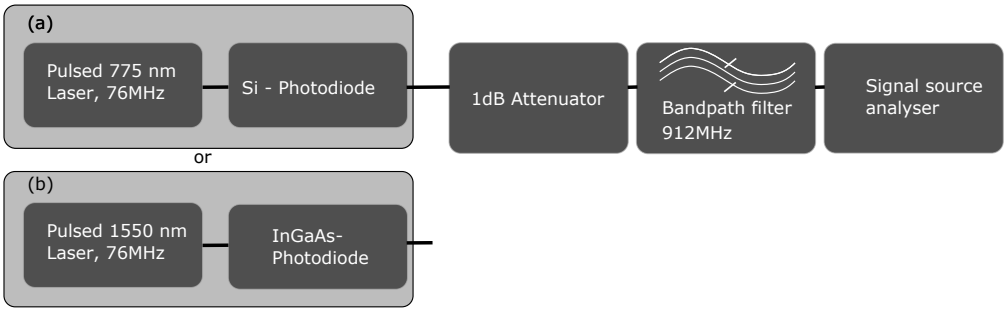

Figure 4.12 – Schematic illustrating jitter measurements of the laser repetition rate. Light from a Coherent Mira laser is detected by a Thorlabs DET02AFC photodiode (a) or light from an NKT photonics Origami 1550 laser is detected by a Thorlabs DET01CFC photodiode (b). Appropriate impedance matching is guaranteed with a 1dB attenuator followed by a ceramic bandpass filter (Mini-Circuits ZX75BP-915-S), which is selecting the 12th harmonic of the electrical signal. The jitter is finally measured by an AnaPico APPH20G Signal Source Analyzer.

The optical pulse train from these laser systems is converted to an electrical signal with fast photodiodes ($\sim$ 1 GHz), which are used in combination with a 1 dB attenuator to provide $50\,\Omega$ termination. The Fourier transformation of the electrical signal is a flat frequency comb with a peak separation of the laser repetition rate 76 MHz[4]. The maximal comb frequency is given by the photodiode bandwidth, which is in this case around 1 GHz for the 3 dB roll-off. In order to suppress the effect from amplitude noise in the measurement, we use a ceramic bandpass filter (Mini-Circuits ZX75BP-915-S) to select the 12th harmonic of the electrical signal (c.f. Sec. 4.4.4.1). The sideband phase noise is finally measured with a signal source analyzer. This device is able to measure very low noise values that correspond to a temporal jitter on the order of fs. To achieve such low sideband phase noise measurements, the incoming signal can be analyzed with cross-correlation techniques to lower the internal device noise floor.

The resulting sideband phase noise measurements for the Coherent Mira Laser are shown in Fig. 4.13. The upper plot shows the measured sideband phase noise from 1 Hz to 100 MHz around the 12th harmonic at 912 MHz. The lower plot shows the integrated RMS jitter value resulting from this phase noise. The jitter value is the integrated sideband phase noise from the given frequency to 100 MHz. For example the green curve shows a jitter value of around 2 ps at 10 Hz. This means that the integrated sideband phase noise from 10 Hz to 100 MHz corresponds to 2 ps. Four different locking configurations where investigated. Blue: open loop, Green: fundamental locking, where the laser only locks to the fundamental repetition rate, red and purple: harmonic locking where the laser locks to the 9th harmonic of the repetition rate. More information about the laser repetition rate locking can be found in Sec. 4.4.4.1. It can be seen that harmonic stabilization is required for low jitter values. Especially a noise source around 100 Hz can be seen in the sideband phase noise measurement, which could result from cavity

[4]Note this frequency comb is fundamentally different than the optical frequency comb centered in the THz regime

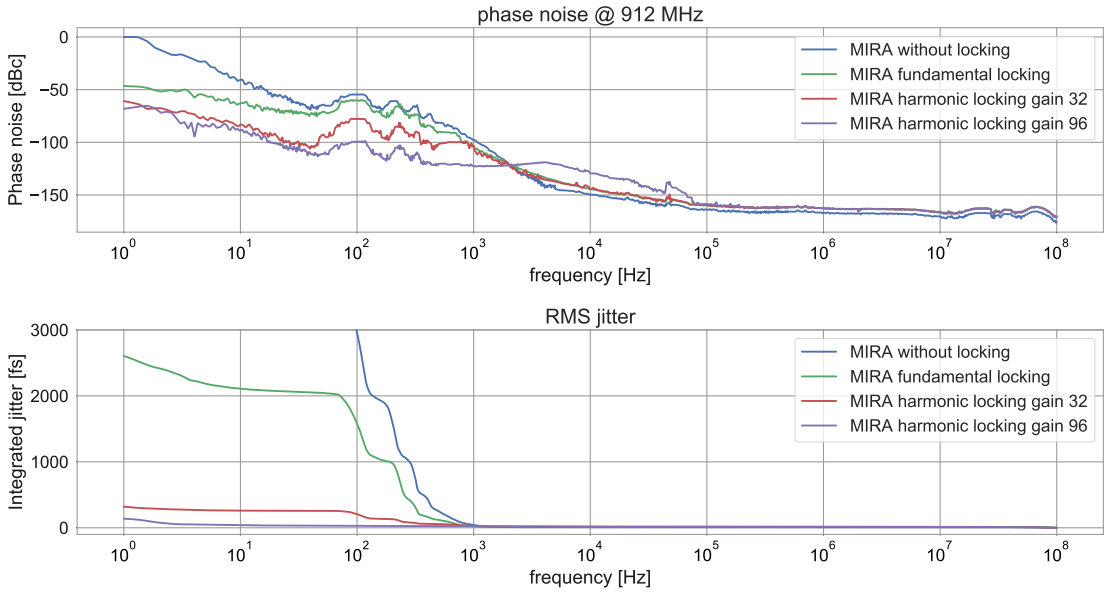

Figure 4.13 – Sideband phase noise measurement from a Coherent Mira laser system. The upper plot shows the sideband phase noise value with respect to the carrier from 1 Hz to 100 MHz sideband frequency. The lower plot shows the RMS jitter value resulting from phase noise integration. The system jitter was measured at the 12th harmonic of the laser repetition frequency. Four different synchronization methods are investigated. See text for further details.

mirror resonances or pump laser fluctuations. These noise sources can be strongly reduced with appropriate locking parameters, as seen in the purple trace. Jitter values down to 140 fs from 1 Hz to 100 MHz can be observed for this configuration.

Fig. 4.14 shows the corresponding jitter measurement for the NKT-photonics Origami laser. Jitter values down to 360 fs from 1 Hz to 100 MHz can be observed for this configuration. It can be seen that this laser experiences lower jitter values in the open-loop (unlocked) configuration than the Coherent Mira laser. If locking is enabled, jitter values are comparable. The difference can mainly be explained by the RF generators used to lock the laser. The Origami laser requires a signal at 3.04 GHz, whereas the Mira laser locks to a 76 MHz signal. The jitter values from these RF-sources are measured and show a timing jitter of 350 fs from 1 Hz to 100 MHz for the 3.04 GHz signal and a value of 140 fs from 1 Hz to 100 MHz for the 76 MHz oscillator. Details about the RF- source measurement can be found in App. E. The measured jitter values for both laser systems are therefore mainly limited by the phase noise from the RF sources.

4.4.4.3 Interference measurement

In addition to the discussed jitter characterization method based on the Von der Linde method, we will also characterize the jitter with an optical interference measurement. In principle, optical

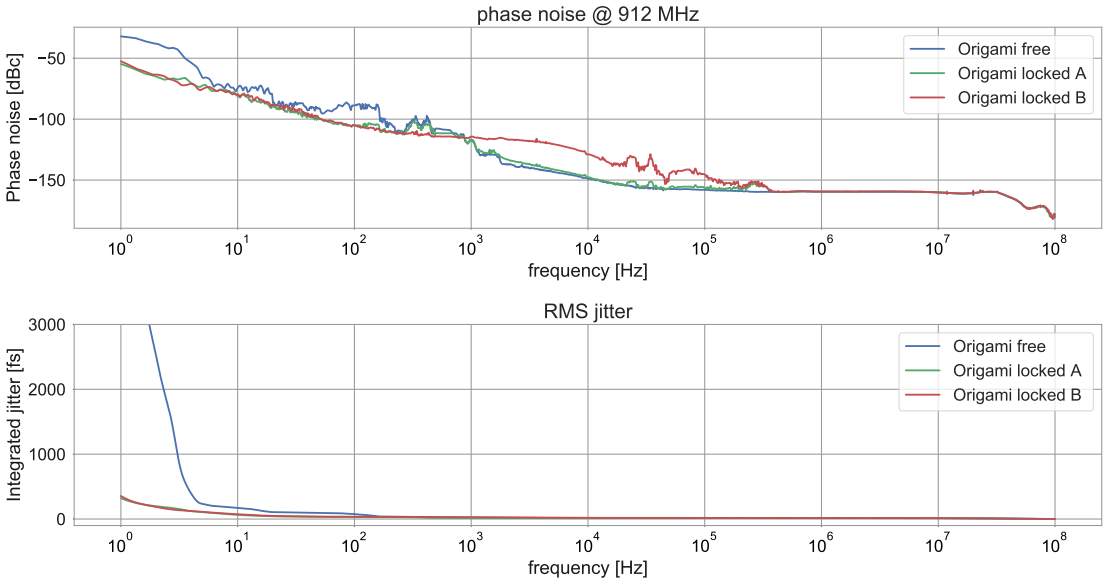

Figure 4.14 – Sideband phase noise measurement from a NKT-photonics Origami laser system. The upper plot shows the sideband phase noise value with respect to the carrier from 1 Hz to 100 MHz sideband frequency. The lower plot shows the RMS jitter value resulting from phase noise integration. The system jitter was measured at the 12th harmonic of the laser repetition frequency. Three different synchronization methods are investigated. See text for further details.

methods are better suited to determine very small noise values [244, 245], but often require the combination of two lasers. Here we will investigate the performance of the 775 nm Mira laser with the frequency-doubled 1550 nm Origami laser. Figure 4.15 shows the schematic setup, where both laser fields are combined on a beam splitter and measured with a fast photodiode. The generated electrical signal is, in this case, measured in the time domain with an oscilloscope. An example time trace can be seen in Fig. 4.16, where interference is only happening on rather short time scales of 150 μs (regions with higher voltage values due to constructive interference). This plot is an often encountered example, where the laser locking is not sufficiently correcting for the environmental noise sources.

In combination with the signal-source analyzer, we have found a set of settings enabling low jitter values (see Fig. 4.17). We have found that we either have to pre-stabilize the master laser on a low jitter external oscillator, similar to the results in [246], or, as a second approach, we can also lock both laser systems to a common shared clock. In any case, the reference signal must be generated carefully. It should have the appropriate power level at the desired locking frequency and low phase-noise values, especially below 10 kHz, where the laser actuators can follow the reference signal.

We still observed some long term drifts on the order of seconds. These could result from varying path length between the laser systems due to temperature fluctuations in the lab (lasers

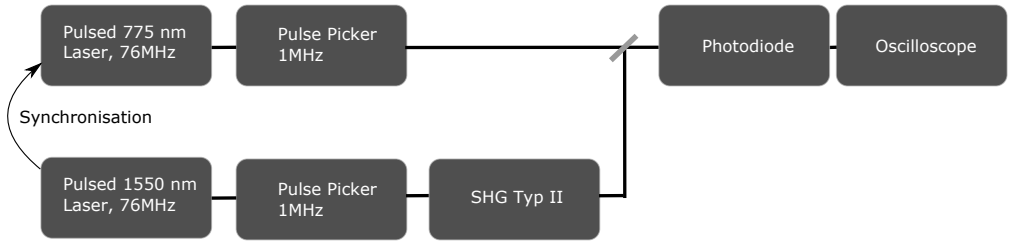

Figure 4.15 – Schematic illustrating the optical interference measurement.

have a separation of 4 m). However, these drifts do not prevent our final measurement as we have to post-select on high interference value for phase reconstruction anyway (see Sec. 4.5.2).

With this, we have proven that repetition-rate locking of two-laser systems can be achieved. Before we apply our work to quantum tomography, we will briefly describe two side projects that were realized in collaboration with the electrical engineering group of Professor Scheytt from Paderborn University, while investigating the laser noise-properties.

4.4.5 Generating low phase-noise electrical signals

Our results have shown, that mode-locked laser systems can be considered as a very precise timing reference. Exact timing references are a crucial ingredient for many electrical devices, from satellite navigation systems, to analog to digital converters, to our communication systems. In many applications, surface acoustic wave or quartz oscillators are the workhorse to generate low noise timing signals. However, if we are searching for stable timing references on very short time scales, passively mode-locked lasers have shown outstanding performance [247–249]. For these lasers, the mode-locking mechanism itself and the associated coherence length sets an upper bound for variations. We will discuss the fundamental limits for high-frequency noise term in the next section. In collaboration with the group of Professor Scheytt we utilized these properties to derive a low-noise electrical signal. Different approaches have been suggested to convert the low noise optical pulse train to an electrical signal with low phase-noise values [250–255]. We implemented a new approach based on a Mach-Zehnder modulator [256] similar to the work in [257] but with a wide tuning range of the electrical output signal (5 GHz to 10 GHz in 76 MHz steps). With this configuration we have shown jitter values down to 13.8 fs at a carrier frequency of 10.032 GHz integrated from 1 kHz to 100 MHz (better than previous works with this method [257]) and a rather compact device suitable to generate low noise electrical signals.

4.4.6 Squeezing for ultra low timing jitter measurements

We have already discussed that mode-locked lasers have superior noise performance in specific frequency ranges. This poses the question about the fundamental limits with classical and non-classical light for these noise values. To study this question, we want to focus on time scales shorter than 1 μs, where laser cavity fluctuations from thermal drifts and mirror vibrations can be neglected (e.g. [258, 259]). A detailed analysis of noise sources has been reported based

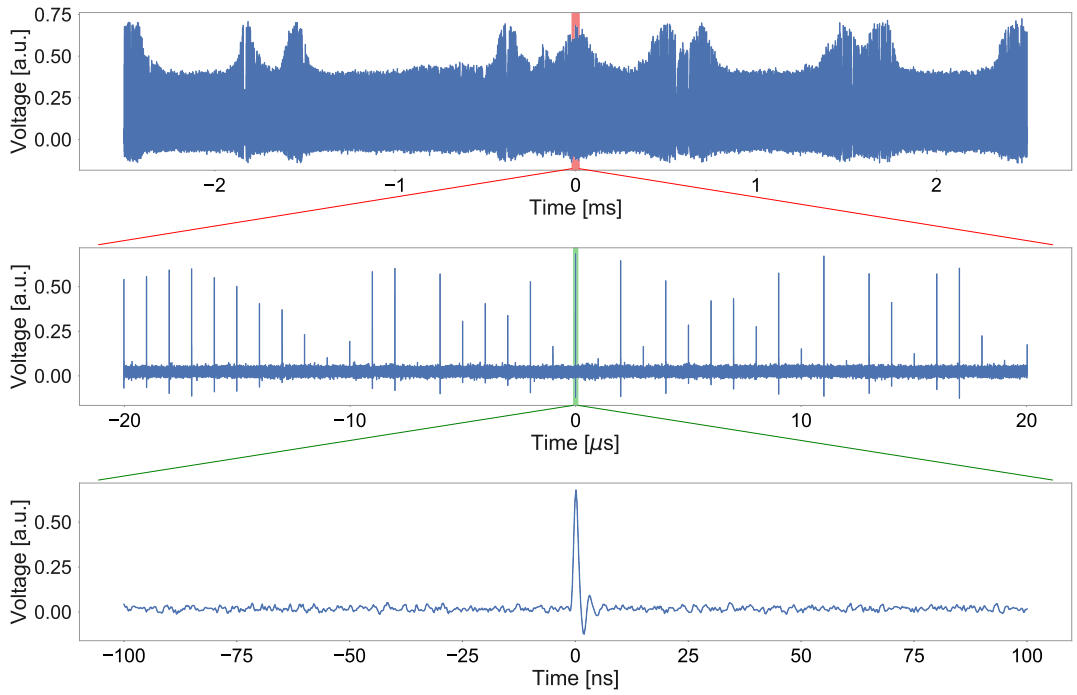

Figure 4.16 – Interference signal between a Ti:Sapph and a frequency-doubled erbium laser. (Top) full oscilloscope trace. Areas with high values are given when pulses from both lasers are (constructively) interfering. Due to a rather high jitter, most of the time, no interference is happening. (Middle) 40 μs section of the oscilloscope trace showing a time area where interference is happening. (Bottom) 200 ns section of the oscilloscope trace showing an individual pulse from the photodiode. The recorded oscilloscope trace contains 25 MSamples recorded with 5 GSamples/s. See text for further details.

on classical and semi-classical models [260–264]. On the quantum optical side, the idea of using squeezed light to improve timings in the context of time transfer between different parties has been proposed [265] and recently demonstrated [266]. Here we want to suggest amplitude squeezed light to reduce the phase noise level of a single laser to improve the derived clock stability.

To do so, we have to differentiate two noise sources in pulsed lasers. On the one side, we can identify a noise process that decreases quadratically as $1/f^2$ in frequency f. A laser following this noise behavior is called quantum limited. This noise results from different quantum effects such as spontaneous emission from the gain medium that occurs inside the laser cavity. Therefore the laser characteristics perform a random walk. Most importantly is that this noise appears inside the laser cavity and cannot be compensated by amplitude squeezing after the laser. On the other side, we have the so-called shot-noise limit (SNL) with a frequency-independent noise

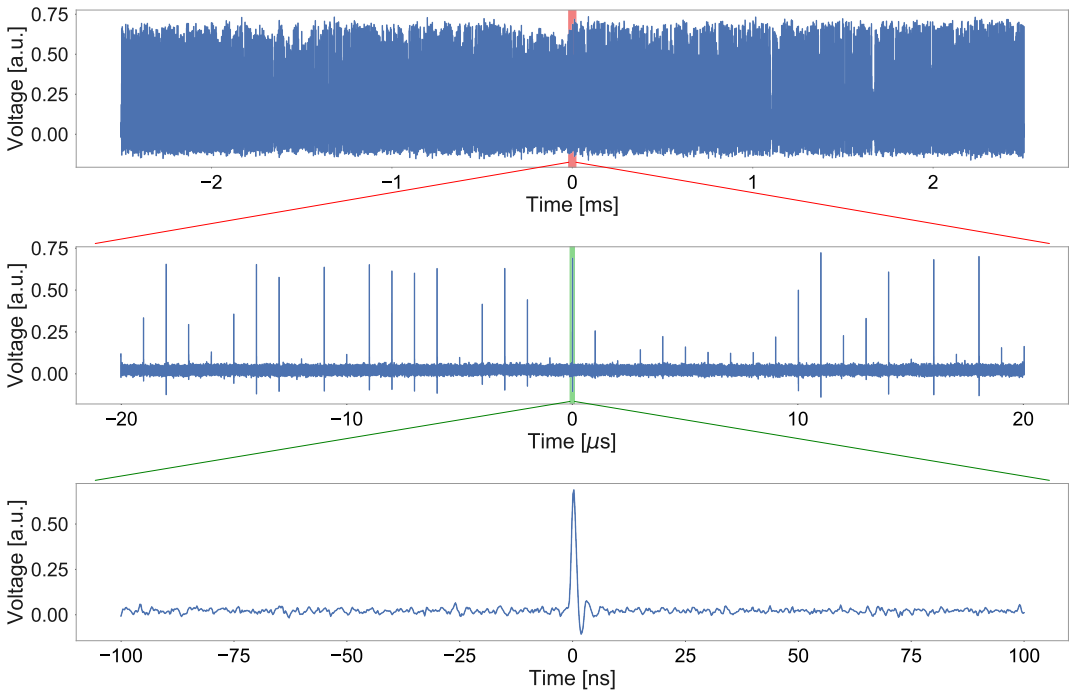

Figure 4.17 – Interference signal between a Ti:Sapph and a frequency-doubled erbium laser. (Top) full oscilloscope trace. Due to a very low timing jitter, interference can be seen over the full oscilloscope trace. (Middle) 40 μs section of the oscilloscope trace showing a time area where interference is happening. (Bottom) 200 ns section of the oscilloscope trace showing an individual pulse from the photodiode. The recorded oscilloscope trace contains 25 MSamples recorded with 5 GSamples/s. See text for further details.

spectrum (white) from the amplitude uncertainty of a coherent state. This noise level will affect the timing error (phase noise) and amplitude noise of the optical pulse train [267]. Interestingly, the optical timing jitter can still be detected, even though the pulse response from the photodiode might be orders of magnitude slower than the optical pulse duration [267].

From now on, we will only concentrate on the SNL, which will be the leading contribution at higher frequencies. We suggest amplitude squeezed light to reduce this noise level. This squeezed light, for example, could be generated in an optical fiber inside an asymmetric Sagnac-interferometer (e.g. [268]). However, the major technical challenge will not only be to generate the non-classical light but also to detect the extremely low noise level, which is already extremely low for SNL lasers.

Based on Eq. 9 in [262] we can estimate the noise level of a shot-noise limited laser. For the given parameters of our NKT-photonics Origami laser ($\tau_{\text{pulse}} = 200$ fs, $\lambda = 1550$ nm,

P_{avg} =10 mW) we can estimate a noise floor of 0.3 zs^2/Hz from

$$S(f) = 0.2647 \frac{h\nu}{P_{\text{avg}}} \tau_{\text{pulse}}^2 \tag{4.28}$$

for the two-sided spectral power density of the pulse timing error for sech^2 shaped pulses [262]. This low noise value poses a major challenge for the detection method. We can see from Eq. 4.28 that the timing jitter caused by shot noise scales quadratically with the pulse duration. Therefore the detection is rather easy for actively mode-locked laser systems with long pulse durations. For passively mode-locked lasers with pulse durations in the fs range the detection becomes a major challenge. To achieve ultra-low noise measurements a method based on optical cross-correlations has been demonstrated (e.g. [269]). Here the noise floor of the measurement is below the shot noise level. Another approach can be found in [267] where in-house-fabricated photodetectors with electrical cross-correlation were used to achieve a very low noise level (-182 dBc/Hz).

In summary, we propose that the timing jitter from mode-locked lasers can be improved with optical squeezing if the laser pulse train is already shot-noise limited. We clarify that a 'quantum-limited' laser output is not sufficient. For the simple case where the pulse train is investigated without an optical LO, amplitude squeezing of the optical carrier field is required to achieve lower timing jitters. Currently, the detection of the ultra-low phase noise values present in SNL passively mode-locked lasers is a major technical challenge. However, the SNL will eventually limit the timing jitter derived from mode-locked lasers. The suggested squeezing approach can overcome this classical barrier.

4.4.7 Conclusion

In this section, we have discussed that a 'truly local' LO is beneficial for quantum characterization because it avoids power constraints, as the full power of the transmitter laser can be used for the quantum state generation. In addition, our approach can be beneficial for CV quantum communication, where the local aspect of our LO improves security aspects and avoids bandwidth limitations. We have experimentally shown that the pulse trains from both laser systems can be stabilized with femtosecond precision. In collaboration with the group of Professor Scheytt, we developed new projects involving the generation of low-noise electrical signals and a proposal for reducing timing jitter measurements with squeezed light. In the following, we will show how two repetition-rate-locked lasers can be used to perform quantum tomography.

4.5 Two-laser tomography

As a next step, we want to use the presented two-laser approach for quantum tomography and profit from its advantages. To demonstrate a prove-of-concept experiment, we have to show a phase stable experimental setup. Even for a single-laser case (LO and quantum state are derived from the same laser), phase stability poses a major challenge, especially for WFH schemes due to an intrinsically low signal to noise ratio. For this reason, only a few experiments have

shown phase-sensitive measurements for non-classical states [270–272] with single-photon detectors. These papers have recorded up to two simultaneous events per displaced mode and shown phase-dependent correlations between individual events. Instead, we want to investigate larger quantum states and show phase stability for the full correlation distribution. In addition, we will demonstrate that overcoming the phase-stability challenge for WFH opens the door for new detection methods such as an improved squeezing measurement with respect to SFH.

4.5.1 Measurement scheme

Measuring squeezed light is a primary application for SFH because reduced noise variances can be directly seen from the measurement output, as discussed in Sec. 4.1.2. Two main mechanisms limit the amount of detectable squeezing, namely optical loss and phase fluctuations between SUT and LO (optical phase jitter). We will focus on the latter, which has been described in detail in the literature [273–276]. In this section, we want to discuss a new approach to measure squeezing with a weak local oscillator in the direct probing (DP) configuration (see Sec. 4.1.2).

The fundamental reason behind the jitter-induced squeezing limit is illustrated in Fig. 4.18. SFH performs a projection of the squeezing ellipse on a quadrature axis. The phase θ that defines the rotation of the ellipse is directly connected with the relative phase between LO and SUT. Depending θ, either squeezing or anti-squeezing values can be observed, as shown in Fig. 4.18 (b) (green, dashed). It can be seen that quadrature variances with an uncertainty smaller than the vacuum can only be seen for a rather small phase range (area I). Any optical phase fluctuations during the measurement will limit the minimal detectable amount of quadrature variance as areas with higher variance are coupled to the measurement. This effect becomes more pronounced for higher squeezing values (area I becomes narrower) [275]. We have already seen in Sec. 4.1.2 that DP can perform a cut of the Wigner function instead of a projection. Here we want to use this feature to perform phase jitter robust squeezing measurements, as we suggest in [165]. By cutting an ellipse, sub-shotnoise variances can be seen over a wide phase range (blue curve and area II in Fig. 4.18 (b)). This directly implies that an optical phase jitter does not affect the measured squeezing value as strongly as in SFH. In some sense, SFH is rather optimized for measuring anti-squeezing as opposed to measuring squeezing. Our new method, instead, is optimized for measuring squeezing. In our experimental realization we will investigate a two-mode squeezed vacuum (TMSV) state because in quantum communication schemes the entanglement between signal and idler mode can be directly used.

Measuring two-mode squeezing

Our newly suggested method can be extended for a TMSV state, as described in Eq. 2.15. In this case the Wigner function is a 4D function of the two complex parameters β_1 and β_2 [277]

$$W(\beta_1,\beta_2) = \frac{4}{\pi^2}\exp\left(-\mathrm{e}^{2r}\left|\beta_1+\beta_2^*\mathrm{e}^{-i\varphi}\right|^2 - \mathrm{e}^{-2r}\left|\beta_1-\beta_2^*\mathrm{e}^{-i\varphi}\right|^2\right), \tag{4.29}$$

and a phase φ resulting from the pump. *Harder et al.* suggested an interesting method to measure squeezing without any phase stability that is restricted to this two-mode squeezing case [277]. In their work, they only vary one parameter β_1 in a phase-averaged way while the other is kept at zero $\beta_2 = 0$ and show that a reduced quadrature variance can still be seen. We have already

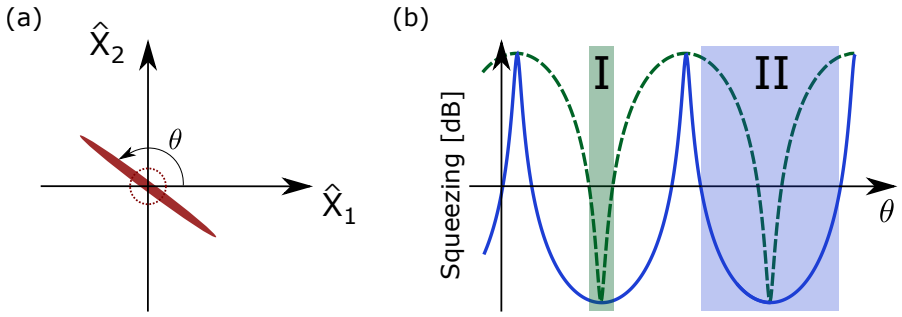

Figure 4.18 – Single-mode squeezed vacuum state rotated with a phase θ. Vacuum variance is indicated as a red dotted circle (a). Measured squeezing values as a function of θ are shown for SFH (green, dashed curve) and DP (blue curve). Areas I and II indicate the phase range where non-classicality can be observed. See text for further details.

discussed in Sec. 4.1.2 that different points in the Wigner function can be addressed in the DP scheme with displacements. This means for two-mode squeezing that we have two LOs in the signal and idler polarization for displacements ($\beta_s = \beta_1$ and $\beta_i = \beta_2$). However, the suggested special cut of the 4D Wigner by *Harder et al.* is non-optimal to detect squeezing. For a fixed LO strength $|\beta_i| + |\beta_s|$ we can see from Eq. 4.29 that the case of $\beta_i = \beta_s$ is better suited to uncover squeezing. For illustration purposes, we can link this to the single-mode case: *Harder et al.* is cutting the squeezing ellipse under a $45°$ axis, whereas a cut parallel to the semi-minor axis of the ellipse would be optimal. We will demonstrate this optimal cut $\beta_i = \beta_s$ in the next section, which still features the suggested optical phase noise robustness as the discussed single-mode case. This means that our suggested method is able to uncover squeezing for a single- and two-mode squeezing case.

4.5.2 Experimental setup

In this section, we will show experimental results for our new method on measuring squeezing with a weak local oscillator in combination with a 'truly local' LO. The experimental setup is shown in Fig. 4.19. On the transmitter side, a Ti:Sapph Coherent Mira laser is used to generate light at 775 nm. The light field is then frequency shaped with a 4f setup and used for pumping a type-II degenerate PDC process inside a periodically poled KTP waveguide. The remaining pump field and the two-mode squeezed vacuum (TMSV) field are sent to the receiver[5]. The LO light field at the receiver side is produced by an NKT-Photonics Origami erbium based fiber laser. The LO is frequency doubled inside a second bulk KTP crystal (in-house fabrication). This second crystal accomplishes two tasks at once. Firstly, the produced second-harmonic field at 775 nm is interfered with the remaining pump from the transmitter side to extract the relative phase between the processes. Secondly, the crystal also delays the horizontal and the vertical polarization with respect to each other to compensate for the birefringence delay of the first

[5]Note: In general, sending the pump field is not required if both laser systems are CEO stabilized. For our proof of concept experiment, we will use the pump field to substitute CEO stabilization.

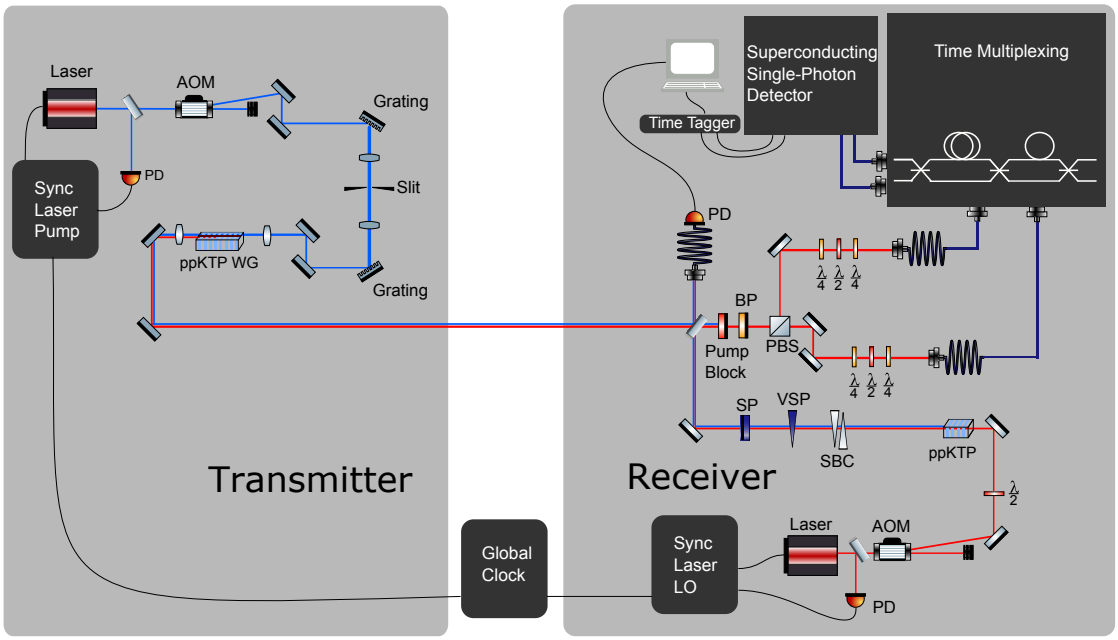

Figure 4.19 – Experimental setup for performing two-laser tomography. AOM: acousto-optic modulator, PD: photodiode, ppKTP WG: waveguided periodically poled potassium titanyl phosphate, (V)SP: (variable) short pass filter, SBC: Soleil-Babinet Compensator, BS: beam splitter, BP: bandpass filter, $\frac{\lambda}{2}$: half-wave plate, $\frac{\lambda}{4}$: quarter-wave plate. See text for further details.

crystal (second crystal has half the length of the first crystal). The 1550 nm light that will be used for the displacement is then attenuated with shortpass filters to the single-photon level and adjusted with an in-house-built variable short pass filter. The relative phase between horizontal and vertical polarization is adjusted with a Soleil-Babinet Compensator (SBC). As a next step, the light fields from both lasers are combined on a broadband, highly transmissive beam splitter. The top output from this beam splitter is directly measured with a fast silicon photodiode that measures the interference pattern between LO and transmitter 775 nm light. The second output port is filtered with a 10 nm bandpass filter around 1550 nm. Signal and idler modes are then separated with a polarizing beam splitter and polarization adjusted with wave plates. Finally a 2x8-bin time multiplexing unit with SNSPDs is detecting both modes. To account for the detector dead time both laser systems use pulse pickers to lower the pulse repetition rate to 500 kHz. Both laser systems are also repetition-rate stabilized and locked to a global clock (see Sec. 4.4.4.1 for more details about the repetition rate locking). To perform full state tomography, the displacements of both signal and idler fields (β_s, β_i) and their phases need to be controlled. To show the working principle, we will restrict ourselves to the optimal cases of measuring two-mode squeezing with equal displacement ($\beta_i = \beta_s$).

The phase sensitivity of the experiment is a critical factor that requires some discussion. If

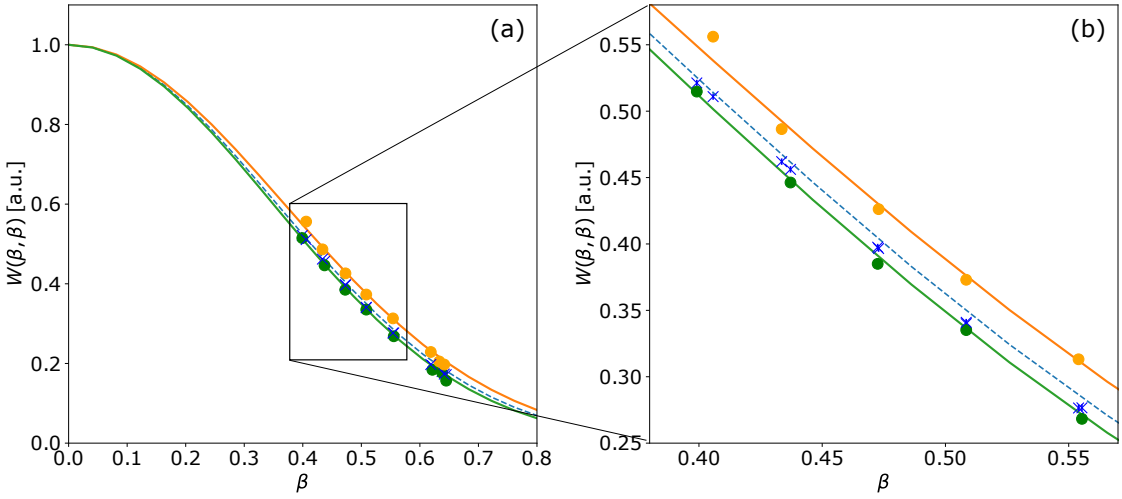

Figure 4.20 – Cut of the 4D-Wigner function where both LOs are equal $\beta = \beta_i = \beta_s$. Yellow dots show anti-squeezing, blue x mark the shot noise level and green dots show squeezing. These points show the raw data (no correction for losses is performed). From the data, an initial squeezing value of 6 dB, a detection efficiency of 16% and an LO to TSVM overlap value of 20% can be inferred. Solid lines show the theoretically expected values assuming these parameters. Error bars based on the measured binomial click statistics are smaller than the data symbols.

no phase stability is achieved, we will measure a phase-averaged state that does not show any non-classical correlations. We will use the interference from the 775 nm fields to infer the phase of the 1550 nm field in post-processing. It is therefore important to note that the 1550 nm and 775 nm light fields from both lasers follow a common path. A subtle point is that the interference patterns have some ambiguity with respect to the underlying phase. We therefore only post-select on maximal interference events, where this ambiguity is avoided. Still, there is a π phase uncertainty at 1550 nm because the phase is retrieved at the second harmonic frequency. However, this poses no additional problems for the final measurement due to the π symmetry of the squeezed state. We can finally scan the relative phase between signal and idler LO with an SBC. Note that only one phase needs to be scanned for this experiment as the phase of the second displacement can be treated as a global phase that does not affect the measurement[6].

4.5.3 Results

Figure 4.20 shows first results on the two-mode squeezing measurement. Scanning the relative phase with an SBC, two positions for seeing squeezing and anti-squeezing can be identified. For these two settings, we performed a scan of the LO strength $\beta = \beta_i = \beta_s$ with an in-house-fabricated position-dependent short-pass filter. Squeezing and anti-squeezing showing a rather

[6]The pump phase φ can be combined with the β_2 phase in Eq. 4.29. Therefore only a relative phase between both LO polarizations needs to be changed.

weak significance due to the detection efficiency of 16%. In addition, we faced some major problems when preparing the LO in the appropriate spectrum. All three fiber couplings (signal, idler, pump) were aligned on the waveguided PDC crystal. However, as the waveguide is only single-mode for the 1550 nm light, we found that the pump wavelength was exiting this crystal in a different spatial mode (waveguide is not single-mode for the pump wavelength). However, the three LO fields (SHG field, displacement for signal, displacement for idler) do not show this slight deviation. Therefore, we could not perfectly match the LO beam to the three fibers due to a limited number of free parameters (common path geometry for 775 nm and 1550 nm is required). Unfortunately, we found spatial-spectral correlations in the outside regions of the Gaussian LO beam. These features were visible directly after the laser output and degraded the overlap between SUT and LO to 20%.

4.5.4 Discussion

We showed that phase stability can be achieved with a two-laser approach and investigated joined photon-number statistics beyond the analysis of previous WFH experiments. Up to now, our generated squeezing values are comparable with single-laser tomography schemes [96]. However, a more powerful transmitter laser can easily solve this constraint.

Also, if we focus on world record squeezing measurements [278], our demonstrated scheme requires improvements. One crucial point is that losses in WFH are too high to compete with SFH experimental demonstrations. In SFH, a total detection efficiency of 97.5% has been realized [278], way above experimental values with photon counting, which are around 80% for bulk sources [18, 279] and below 70% for waveguided sources [89]. Nevertheless, huge improvements have been made in this field over the last years. For example, the development of highly efficient SNSPDs [102, 159] and the possibility for (pseudo) photon-number resolution [153, 154] might pave the way for new photon-number resolved detection schemes.

Besides, optical phase jitter values have been extensively optimized for SFH squeezing measurements. State of the art experiments feature optical phase jitters values smaller than 2 mrad, which do not degrade modern squeezing measurements [278]. Nevertheless, as optical phase jitter values become more important for stronger squeezing values, these might limit future measurements. More importantly is that these stability values have only been shown for well-controlled lab environments. For CV quantum communication purposes, optical phase jitter values are highly relevant. Here photon-number resolved schemes, as we suggested, can be beneficial.

4.5.5 Conclusion

In summary, we have shown a new scheme for measuring squeezed light with a weak local oscillator that can handle higher optical phase jitter values compared to standard SFH. We therefore overcome a fundamental limit for the detection of squeezing that allows for communication channels with higher (phase) noise levels. In addition, we also demonstrate a 'truly local' LO approach generated at the receiver side. This special LO improves the security aspect in CV communication scenarios and reduces the communication bandwidth requirements, as the LO is

not transmitted in combination with the quantum state. By measuring a TMSV state, we demonstrate that we can achieve phase-stability (via post-processing), which is a crucial ingredient for CV quantum communication. Therefore, this work opens the route for highly efficient quantum communication schemes and shows how hybrid CV-DV approaches can enable new detection methods.

CHAPTER 5

Conclusion and Outlook

In this thesis, a variety of new methods for quantum state generation, detection, and characterization were discussed. Finally, we want to summarize the results and give a brief outlook for the individual topics.

Chapter 2 - Quantum state generation: In this chapter, we focused on the PDC process, which is one of the most widely used processes to generate quantum states. We discussed existing schemes to generate interesting, non-classical states in the CV and DV picture with this process. Theoretically and experimentally we focused on the generation of heralded higher-order Fock states. We have shown heralded states of up to $n = 7$ and a high generation rate of at least 1000 count/s. To reach these rates, high squeezing values above 11 dB are required. Typically, these high squeezing values are mainly interesting in the context of CV computation as they decrease the fidelity for heralded single-photon sources. However, here we show that high squeezing values also become important for DV experiments to achieve sufficient heralding rates for higher-order Fock states. Single-pass waveguide sources are ideal for this purpose as they feature low loss and high confinement to achieve high effective non-linearities.

In addition, we have identified fundamental limits for the Fock state generation due to the probabilistic nature of the PDC process and imperfections such as loss and multimodeness. A new approach, based on the connection to discrete phase-type distributions, enables these calculations. With our work, it is straight forward to analyze the feasibility of new experiments requiring higher-order Fock states, e.g. quantum non-gaussianity tests [280]. Moreover, our work also stresses that novel generation schemes [80, 81, 97] for generating these states, especially with feed-forward capabilities, need to be explored further.

Our work is a first step towards generating larger quantum states, which are rare at the moment. Large in this context should mean that the 'quantum' aspect is large (beyond a displaced single-photon state, which also can have a high mean photon number, e.g. [281, 282]). Even more challenging are bright states, which are genuinely non-Gaussian. This problem was investigated and precisely defined last year by *Lachman et al.* [280]. However, only quantum non-Gaussian states for $n = 1$ have been demonstrated so far. This highlights the need for new generation methods.

Chapter 3 - Photon number detection: We have seen in this chapter that detector multiplexing is a crucial tool, as many detectors do not have intrinsic photon number resolution. With our new high dynamic range detection scheme, we have shown that we can measure optical energies from 10^{-7} to $2.5 \cdot 10^{5}$ photons per pulse with the same detection configuration and no experimental modifications. Our detector, therefore, spans a dynamic range of 123 dB (orders of magnitude larger than previously shown multiplexing schemes) and keeps its ability for identifying non-classicality. However, for this presented detection scheme, single-shot evaluations lose precision with increasing light intensities (although the exact transition remains an open research problem). Therefore, we also designed a second TMD unit with equal bin probabili-

ties. The TMD has 2x128 time-bins, which makes it the largest TMD device demonstrated so far. Still, it shows very high transmission values (above 81%), making it attractive for various applications, especially as this design does not show any form of detection cross-talk. With this device, we have investigated non-classical signatures of up to ten photons spread over up to 64 modes with correlation functions. Finally, we also investigated the upcoming topic of multi-pixel SNSPDs with intrinsic pseudo photon number resolution due to spatial multiplexing. We show a new readout scheme that is able to determine the number of detection events. Our scheme does not require additional readout wires and therefore does not pose additional heat loads on the cryostat. With increasing pixel size [154], this will become more important and our method can help to read out detectors or subpixel-regions. In summary, we have shown new multiplexing designs in combination with improved detector multiplexing strategies to extend photon number measurements for mesoscopic states. These states are of general interest because they allow to study the crossing from the quantum to the classical world. In addition, large quantum states are also interesting for applications such as sensing, but more research is necessary in this area.

For future studies, a variety of new challenges need to be overcome. For example, efficient readout schemes will become more important for increasing bin size. With our new 2x128-bin TMD, we are already in a regime where storing all click patterns between all bins is impossible (2^{256} possibilities, similar to the number of atoms in the universe). Extracting the relevant information will become more important for higher bin numbers, as megapixel SNSPDs will become feasible in the next years. This poses technical challenges for detector readout as well as a need for characterization techniques that can handle the data. Our presented work is a first step in this direction.

Chapter 4 - Quantum state tomography: We finally combined the discussed strategies of state generation and detection for quantum state characterization. We showed three new methods to investigate quantum states at the single-photon level. Firstly, we have shown a new tomography approach that utilizes overlap variations to determine the quantum state. In this scheme, only the discrete outcomes from a single click-detector is sufficient to reconstruct the full Husimi-Q function. Likewise, we have shown that we can characterize the mode profile or the overlap if the state is known. This work highlights the need for quantum state characterizations that also involve modal properties. Knowing the shape of the mode structure is often an implicit assumption in quantum tomography, while we are able to address both properties with our scheme directly. As a next step, performing multimode quantum tomography and a comparison to other approaches such as the quantum pulse gate [208] is an interesting direction and would highlight the full potential for quantum characterization with a weak LO.

Secondly, we implemented a proposed scheme [226] for measuring the generalized phase-space function with multiplexed detectors. We confirmed the surprising finding that sometimes non-classicality can be measured with higher significance if fewer detectors are used. Besides, our theory combines the effect of optical losses and the phase-space parameter s, making our approach robust to experimental imperfections. In addition, no inversion process is required to characterize the quantum state. Therefore, our work is an easy to use new measurement tool for future quantum state tomography that shows a link between the phase-space picture and the discrete outcome of multiplexed detectors. Especially for bright states, tomographically complete measurements can be demanding (states might be more susceptible to losses and the

overall parameter space is larger). Future measurements will require efficient indicators for non-classicality, such as the negativity of the generalized phase-space function. Incomplete multiplexing schemes, as shown in our work, are a first step in this direction.

Thirdly, we present a new tomography scheme with a truly local LO that is useful for remote characterization and CV communication. In this scheme the LO is generated at the receiver side by a second laser. Therefore, our scheme reduces bandwidth constraints on the communication channel, as the LO is not transmitted in combination with the quantum state. Moreover, the local aspect of the LO generation provides security advantages and helps to overcome previous pump power constraints. Apart from our truly local LO we also show a new method for characterizing squeezing values in an optical-phase-jitter robust way by performing a cut through the squeezing ellipse with photon-counting measurements. We compared our theory to experimental data and investigated a two-mode squeezed state with this direct probing technique. For this detection, the integration of a DV measurement in an otherwise CV-inspired context was a crucial factor. This work is important for future measurements with increased optical phase stability requirements that can result from a noisy communication channel or high squeezing values. As a next step, the shown overlap values between the SUT and LO need to be improved as well as the generated squeezing value. Here for example an amplifier system such as the Coherent RegA could be used to increase the available pump power. In addition, using CEP stabilized lasers and improved locking electronics (to account for long term drifts) could significantly increase the overall data rate. This could even enable locking without a global clock if a reference sequence is encoded in the signal. Finally, the experiment should be tested under realistic assumptions by investigating a noisy fiber link. In this context, violating a Bell-type inequality would prove the capabilities of our scheme (e.g. [272]). Finally, showing our two-laser approach for SFH is an interesting research direction that would allow a direct comparison between both schemes.

Furthermore, technical challenges encountered in laser locking stimulated discussions with the system and circuit technology group led by Prof. Dr. Christoph Scheytt. Resulting from these discussions we propose a new idea to reduce high-frequency timing jitters with amplitude squeezing. The research field of highly stable optical clocks in combination with quantum optical tools is very interesting as it promises easy to implement solutions to a well-known problem. This research field has the potential to link quantum optics with our daily life because timing references are so important in our world.

In summary, DV measurements, in combination with CV interpretations, helped us to derive new detection methods. Future work can profit from new DV tools, such as the recently proposed scheme that combines the generalized phase-space description in combination with correlation measurements to show improved non-classicality measures [283]. The interplay between CV and DV is also a promising field for quantum communication purposes as it can combine existing telecommunication infrastructures with non-Gaussian DV measurements.

So from a modern perspective, who was right in the end: Newton with his particle picture, Huygens with the wave interpretation or both? The answer is neither of them was correct [70] as both classical theories fail to describe quantum optical states sufficiently. Modern CV and DV approaches can handle these quantum properties. Still, we have shown that changing the perspective from time to time can be a useful tool for exploring new methods.

References

[1] C. Huygens. *Traité de la lumière*. Chez Pierre vander Aa, 1690.

[2] M. Planck. "On the law of the energy distribution in the normal spectrum". *Annalen der Physik* 4 (1901), pp. 553–564.

[3] A. Einstein. "Über einen die Erzeugung und Verwandlung des Lichtes betreffenden heuristischen Gesichtspunkt". *Annalen der Physik* 4.17 (1905), pp. 132–148.

[4] A. Einstein, B. Podolsky, and N. Rosen. "Can quantum-mechanical description of physical reality be considered correct?" *Physical review* 47.10 (1935), p. 777.

[5] E. Schrödinger. "Discussion of probability relations between separated systems". *Mathematical Proceedings of the Cambridge Philosophical Society* 31.4 (1935), pp. 555–563.

[6] E. Schrödinger. "Probability relations between separated systems". *Mathematical Proceedings of the Cambridge Philosophical Society* 32.3 (1936), pp. 446–452.

[7] J. P. Gordon, H. J. Zeiger, and C. H. Townes. "The maser-new type of microwave amplifier, frequency standard, and spectrometer". *Physical Review* 99.4 (1955), pp. 1264–1274.

[8] T. H. Maiman. "Stimulated optical radiation in Ruby". *Nature* 187.4736 (1960), pp. 493–494.

[9] D. C. Burnham and D. L. Weinberg. "Observation of simultaneity in parametric production of optical photon pairs". *Physical Review Letters* 25.2 (1970), pp. 84–87.

[10] R. J. Glauber. "The quantum theory of optical coherence". *Physical Review* 130.6 (1963), pp. 2529–2539.

[11] K. E. Cahill and R. J. Glauber. "Density operators and quasiprobability distributions". *Physical Review* 177.5 (1969), pp. 1882–1902.

[12] P. G. Kwiat, S. Barraza-Lopez, A. Stefanov, and N. Gisin. "Experimental entanglement distillation and 'hidden' non-locality". *Nature* 409.6823 (2001), pp. 1014–1017.

[13] J. W. Pan, C. Simon, Č. Brukner, and A. Zeilinger. "Entanglement purification for quantum communication". *Nature* 410.6832 (2001), pp. 1067–1070.

[14] H. Takahashi, K. Wakui, S. Suzuki, et al. "Generation of large-amplitude coherent-state superposition via ancilla-assisted photon subtraction". *Physical Review Letters* 101.23 (2008), p. 233605.

[15] V. D. Vaidya, B. Morrison, L. G. Helt, et al. "Broadband quadrature-squeezed vacuum and nonclassical photon number correlations from a nanophotonic device". *arXiv:1904.07833* (2019).

[16] G. S. Thekkadath, D. S. Phillips, J. F. Bulmer, et al. "Tuning between photon-number and quadrature measurements with weak-field homodyne detection". *Physical Review A* 101.3 (2020), p. 031801.

[17] S. Aaronson and A. Arkhipov. “The computational complexity of linear optics”. *Proceedings of the Annual ACM Symposium on Theory of Computing* (2011), pp. 333–342.

[18] S. Slussarenko, M. M. Weston, H. M. Chrzanowski, et al. “Unconditional violation of the shot-noise limit in photonic quantum metrology”. *Nature Photonics* 11.11 (2017), pp. 700–703.

[19] S. P. Walborn, D. S. Lemelle, M. P. Almeida, and P. H. Ribeiro. “Quantum key distribution with higher-order alphabets using spatially encoded qudits”. *Physical Review Letters* 96.9 (2006), p. 090501.

[20] H. Paul, P. Törmä, T. Kiss, and I. Jex. “Photon chopping: New way to measure the quantum state of light”. *Physical Review Letters* 76.14 (1996), pp. 2464–2467.

[21] J. Kim, S. Takeuchi, Y. Yamamoto, and H. H. Hogue. “Multiphoton detection using visible light photon counter”. *Applied Physics Letters* 74.7 (1999), pp. 902–904.

[22] K. Banaszek and I. A. Walmsley. “Photon counting with a loop detector”. *Optics Letters* 28.1 (2003), pp. 52–54.

[23] D. Achilles, C. Silberhorn, C. Śliwa, K. Banaszek, and I. A. Walmsley. “Fiber-assisted detection with photon number resolution”. *Optics Letters* 28.23 (2003), pp. 2387–2389.

[24] J. Řeháček, Z. Hradil, O. Haderka, J. Peřina, and M. Hamar. “Multiple-photon resolving fiber-loop detector”. *Physical Review A* 67.6 (2003), p. 061801.

[25] M. J. Fitch, B. C. Jacobs, T. B. Pittman, and J. D. Franson. “Photon-number resolution using time-multiplexed single-photon detectors”. *Physical Review A* 68.4 (2003), p. 43814.

[26] P. A. Franken, A. E. Hill, C. W. Peters, and G. Weinreich. “Generation of optical harmonics”. *Physical Review Letters* 7.4 (1961), pp. 118–119.

[27] J. D. Jackson. “Classical electrodynamics 3rd”. Wiley, 1999.

[28] P. A. M. Dirac. *The principles of quantum mechanics*. Oxford university press, 1981.

[29] H. Weyl. “Quantenmechanik und Gruppentheorie”. *Zeitschrift für Physik* 46.1-2 (1927), pp. 1–46.

[30] R. P. Feynman, A. R. Hibbs, and D. F. Styer. *Quantum mechanics and path integrals*. Courier Corporation, 2010.

[31] C. C. Gerry and P. L. Night. *Introductory quantum optics*. 2005.

[32] C. K. Hong and L. Mandel. “Theory of parametric frequency down conversion of light”. *Physical Review A* 31.4 (1985), pp. 2409–2418.

[33] A. Christ, B. Brecht, W. Mauerer, and C. Silberhorn. “Theory of quantum frequency conversion and type-II parametric down-conversion in the high-gain regime”. *New Journal of Physics* 15.5 (2013), p. 053038.

[34] N. Quesada and J. E. Sipe. “Time-ordering effects in the generation of entangled photons using nonlinear optical processes”. *Physical Review Letters* 114.9 (2015), p. 093903.

[35] A. Christ, K. Laiho, A. Eckstein, et al. “Spatial modes in waveguided parametric down-conversion”. *Physical Review A* 80.3 (2009), p. 033829.

[36] A. Christ, K. Laiho, A. Eckstein, K. N. Cassemiro, and C. Silberhorn. “Probing multimode squeezing with correlation functions”. *New Journal of Physics* 13.3 (2011), p. 33027.

[37] S. Barnett and P. Radmore. *Methods in theoretical quantum optics*. 2010.

[38] M. G. Raymer and I. A. Walmsley. “Temporal modes in quantum optics: Then and now”. *Physica Scripta* 95.6 (2020), p. 064002.

[39] U. M. Titulaer and R. J. Glauber. “Density operators for coherent fields”. *Physical Review* 145.4 (1966), pp. 1041–1050.

[40] P. P. Rohde, W. Mauerer, and C. Silberhorn. “Spectral structure and decompositions of optical states, and their applications”. *New Journal of Physics* 9.4 (2007), p. 91.

[41] W. Mauerer. “On Colours, Keys, and Correlations: Multimode Parametric Downconversion in the Photon Number Basis”. PhD thesis. Universität Erlangen-Nürnberg, 2009.

[42] M. Giustina, M. A. Versteegh, S. Wengerowsky, et al. “Significant-loophole-free test of Bell’s theorem with entangled photons”. *Physical Review Letters* 115.25 (2015), pp. 1–7.

[43] L. K. Shalm, E. Meyer-Scott, B. G. Christensen, et al. “Strong loophole-free test of local realism”. *Physical Review Letters* 115.25 (2015), p. 250402.

[44] V. Giovannetti, S. Lloyd, and L. MacCone. “Advances in quantum metrology”. *Nature Photonics* 5.4 (2011), pp. 222–229.

[45] C. K. Hong, Z. Y. Ou, and L. Mandel. “Measurement of subpicosecond time intervals between two photons by interference”. *Physical Review Letters* 59.18 (1987), pp. 2044–2046.

[46] A. I. Lvovsky, H. Hansen, T. Aichele, et al. “Quantum state reconstruction of the single-photon fock state”. *Physical Review Letters* 87.5 (2001), p. 050402.

[47] A. B. U’Ren, C. Silberhorn, K. Banaszek, and I. A. Walmsley. “Efficient conditional preparation of high-fidelity single photon states for fiber-optic quantum networks”. *Physical Review Letters* 93.9 (2004), p. 093601.

[48] T. B. Pittman, B. C. Jacobs, and J. D. Franson. “Heralding single photons from pulsed parametric down-conversion”. *Optics Communications* 246.4-6 (2005), pp. 545–550.

[49] S. Castelletto, I. P. Degiovanni, V. Schettini, and A. Migdall. “Optimizing single-photon-source heralding efficiency and detection efficiency metrology at 1550 nm using periodically poled lithium niobate”. *Metrologia*. Vol. 43. 2. IOP Publishing, 2006, S56.

[50] A. Christ and C. Silberhorn. “Limits on the deterministic creation of pure single-photon states using parametric down-conversion”. *Physical Review A* 85.2 (2012), p. 023829.

[51] W. P. Grice and I. A. Walmsley. “Spectral information and distinguishability in type-II down-conversion with a broadband pump”. *Physical Review A* 56.2 (1997), pp. 1627–1634.

[52] C. K. Law, I. A. Walmsley, and J. H. Eberly. "Continuous frequency entanglement: Effective finite hilbert space and entropy control". *Physical Review Letters* 84.23 (2000), pp. 5304–5307.

[53] J. H. Eberly. "Schmidt analysis of pure-state entanglement". *Laser Physics* 16.6 (2006), pp. 921–926.

[54] A. B. U'Ren, K. Banaszek, and I. A. Walmsley. "Photon engineering for quantum information processing". *Quantum Information and Computation* 3 (2003), pp. 480–502.

[55] R. W. Boyd. *Nonlinear optics*. Academic press, 2008.

[56] M. Yamada, N. Nada, M. Saitoh, and K. Watanabe. "First-order quasi-phase matched LiNbO3 waveguide periodically poled by applying an external field for efficient blue second-harmonic generation". *Applied Physics Letters* 62.5 (1993), pp. 435–436.

[57] P. Ben Dixon, J. H. Shapiro, and F. N. C. Wong. "Spectral engineering by Gaussian phase-matching for quantum photonics". *Optics Express* 21.5 (2013), pp. 5879–5890.

[58] A. Dosseva, Ł. Cincio, and A. M. Brańczyk. "Shaping the joint spectrum of down-converted photons through optimized custom poling". *Physical Review A* 93.1 (2016), p. 013801.

[59] F. Graffitti, D. Kundys, D. T. Reid, A. M. Brańczyk, and A. Fedrizzi. "Pure down-conversion photons through sub-coherence-length domain engineering". *Quantum Science and Technology* 2.3 (2017), p. 035001.

[60] P. J. Mosley, J. S. Lundeen, B. J. Smith, et al. "Heralded generation of ultrafast single photons in pure quantum states". *Physical Review Letters* 100.13 (2008), p. 133601.

[61] A. Eckstein, A. Christ, P. J. Mosley, and C. Silberhorn. "Highly efficient single-pass source of pulsed single-mode twin beams of light". *Physical Review Letters* 106.1 (2011), p. 013603.

[62] T. Gerrits, M. J. Stevens, B. Baek, et al. "Generation of degenerate, factorizable, pulsed squeezed light at telecom wavelengths". *Optics Express* 19.24 (2011), pp. 24434–24447.

[63] G. Harder, V. Ansari, B. Brecht, et al. "An optimized photon pair source for quantum circuits". *Optics Express* 21.12 (2013), pp. 13975–13985.

[64] E. Meyer-Scott, N. Montaut, J. Tiedau, et al. "Limits on the heralding efficiencies and spectral purities of spectrally filtered single photons from photon-pair sources". *Physical Review A* 95.6 (2017), p. 61803.

[65] E. Meyer-Scott, C. Silberhorn, and A. Migdall. "Single-photon sources: Approaching the ideal through multiplexing". *Review of Scientific Instruments* 91.4 (2020), p. 041101.

[66] A. V. Kuhlmann, J. Houel, A. Ludwig, et al. "Charge noise and spin noise in a semiconductor quantum device". *Nature Physics* 9.9 (2013), pp. 570–575.

[67] A. V. Kuhlmann, J. H. Prechtel, J. Houel, et al. "Transform-limited single photons from a single quantum dot". *Nature Communications* 6.1 (2015), p. 8204.

[68] N. Somaschi, V. Giesz, L. De Santis, et al. "Near-optimal single-photon sources in the solid state". *Nature Photonics* 10.5 (2016), pp. 340–345.

[69] G. Kiršanske, H. Thyrrestrup, R. S. Daveau, et al. “Indistinguishable and efficient single photons from a quantum dot in a planar nanobeam waveguide”. *Physical Review B* 96.16 (2017), p. 165306.

[70] J. Sperling, S. De, T. Nitsche, et al. “Wave-particle duality revisited: Neither wave nor particle”. *arXiv:1907.09836v1* (2019).

[71] A. Ourjoumtsev, H. Jeong, R. Tualle-Brouri, and P. Grangier. “Generation of optical ’Schrödinger cats’ from photon number states”. *Nature* 448.7155 (2007), pp. 784–786.

[72] M. J. Holland and K. Burnett. “Interferometric detection of optical phase shifts at the heisenberg limit”. *Physical Review Letters* 71.9 (1993), pp. 1355–1358.

[73] E. S. Polzik, J. Carri, and H. J. Kimble. “Spectroscopy with squeezed light”. *Physical Review Letters* 68.20 (1992), pp. 3020–3023.

[74] N. P. Georgiades, E. S. Polzik, K. Edamatsu, H. J. Kimble, and A. S. Parkins. “Nonclassical excitation for atoms in a squeezed vacuum”. *Physical Review Letters* 75.19 (1995), pp. 3426–3429.

[75] D. C. Kilper, A. C. Schaefer, J. Erland, and D. G. Steel. “Coherent nonlinear optical spectroscopy using photon-number squeezed light”. *Physical Review A* 54.3 (1996), R1785–R1788.

[76] Y. Yamamoto and H. A. Haus. “Preparation, measurement and information capacity of optical quantum states”. *Reviews of Modern Physics* 58.4 (1986), pp. 1001–1020.

[77] G. M. D’Ariano, L. Maccone, M. G. Paris, and M. F. Sacchi. “Optical Fock-state synthesizer”. *Physical Review A* 61.5 (2000), p. 053817.

[78] K. R. Brown, K. M. Dani, D. M. Stamper-Kurn, and K. B. Whaley. “Deterministic optical Fock-state generation”. *Physical Review A* 67.4 (2003), p. 043818.

[79] K. Sanaka. “Linear optical extraction of photon-number Fock states from coherent states”. *Physical Review A* 71.2 (2005), p. 021801.

[80] K. T. McCusker and P. G. Kwiat. “Efficient optical quantum state engineering”. *Physical Review Letters* 103.16 (2009), p. 163602.

[81] B. L. Glebov, J. Fan, and A. Migdall. “Photon number squeezing in repeated parametric downconversion with ancillary photon-number measurements”. *Optics Express* 22.17 (2014), p. 20358.

[82] A. M. Brańczyk, T. C. Ralph, W. Helwig, and C. Silberhorn. “Optimized generation of heralded Fock states using parametric down-conversion”. *New Journal of Physics* 12.6 (2010), p. 063001.

[83] N. Quesada. “Very Nonlinear Quantum Optics”. PhD thesis. University of Toronto, 2015.

[84] J. Tiedau, T. J. Bartley, G. Harder, et al. “Scalability of parametric down-conversion for generating higher-order Fock states”. *Physical Review A* 100.4 (2019), p. 41802.

[85] A. Ourjoumtsev, R. Tualle-Brouri, and P. Grangier. “Quantum homodyne tomography of a two-photon fock state”. *Physical Review Letters* 96.21 (2006), p. 213601.

[86] E. Waks, E. Diamanti, and Y. Yamamoto. “Generation of photon number states”. *New Journal of Physics* 8.16 (2006), pp. 3534–3537.

[87] A. Zavatta, V. Parigi, and M. Bellini. “Toward quantum frequency combs: Boosting the generation of highly nonclassical light states by cavity-enhanced parametric down-conversion at high repetition rates”. *Physical Review A* 78.3 (2008), p. 033809.

[88] M. Cooper, L. J. Wright, C. Söller, and B. J. Smith. “Experimental generation of multi-photon Fock states”. *Optics Express* 21.5 (2013), pp. 5309–5317.

[89] G. Harder, T. J. Bartley, A. E. Lita, et al. “Single-mode parametric-down-conversion states with 50 photons as a source for mesoscopic quantum optics”. *Physical Review Letters* 116.14 (2016), p. 143601.

[90] T. S. Iskhakov, V. C. Usenko, U. L. Andersen, et al. “Heralded source of bright multi-mode mesoscopic sub-Poissonian light”. *Optics Letters* 41.10 (2016), pp. 2149–2152.

[91] R. Jozsa. “Fidelity for mixed quantum states”. *Journal of Modern Optics* 41.12 (1994), pp. 2315–2323.

[92] D. Rosenberg, S. W. Nam, A. J. Miller, et al. “Near-unity absorption of near-infrared light in tungsten films”. *Nuclear Instruments and Methods in Physics Research, Section A: Accelerators, Spectrometers, Detectors and Associated Equipment*. Vol. 520. 1-3. 2004, pp. 537–540.

[93] W. Mauerer, M. Avenhaus, W. Helwig, and C. Silberhorn. “How colors influence numbers: Photon statistics of parametric down-conversion”. *Physical Review A* 80.5 (2009), p. 053815.

[94] M. F. Neuts. *Matrix-geometric solutions in stochastic models: an algorithmic approach*. Courier Corporation, 1994.

[95] M. Avenhaus, H. B. Coldenstrodt-Ronge, K. Laiho, et al. “Photon number statistics of multimode parametric down-conversion”. *Physical Review Letters* 101.5 (2008), p. 053601.

[96] T. Dirmeier, J. Tiedau, I. Khan, et al. “Distillation of squeezing using an engineered PDC source”. *arXiv:1907.08004v1* (2019).

[97] M. Engelkemeier, L. Lorz, S. De, et al. “Quantum photonics with active feedback loops”. *arXiv:2002.08154v1* (2020).

[98] M. Fox. *Quantum optics: an introduction*. OUP Oxford, 2006.

[99] L. Barsotti, J. Harms, and R. Schnabel. *Squeezed vacuum states of light for gravitational wave detectors*. 2018.

[100] R. Demkowicz-Dobrzański, K. Banaszek, and R. Schnabel. “Fundamental quantum interferometry bound for the squeezed-light-enhanced gravitational wave detector GEO 600”. *Physical Review A* 88.4 (2013), p. 41802.

[101] A. Bassi, K. Lochan, S. Satin, T. P. Singh, and H. Ulbricht. “Models of wave-function collapse, underlying theories, and experimental tests”. *Reviews of Modern Physics* 85.2 (2013), pp. 471–527.

[102] D. V. Reddy, A. E. Lita, S. Nam, R. P. Mirin, and V. B. Verma. "Achieving 98% system efficiency at 1550 nm in superconducting nanowire single photon detectors". *Proceedings Rochester Conference on Coherence and Quantum Optics, CQO 2019*. Optical Society of America (OSA), 2019, W2B.2.

[103] Y. Hochberg, I. Charaev, S. W. Nam, et al. "Detecting sub-GeV dark matter with superconducting nanowires". *Physical Review Letters* 123.15 (2019), p. 151802.

[104] A. Vetter, S. Ferrari, P. Rath, et al. "Cavity-enhanced and ultrafast superconducting single-photon detectors". *Nano Letters* 16.11 (2016), pp. 7085–7092.

[105] B. Korzh, Q. Y. Zhao, J. P. Allmaras, et al. "Demonstration of sub-3 ps temporal resolution with a superconducting nanowire single-photon detector". *Nature Photonics* 14.4 (2020), pp. 250–255.

[106] L. Mandel. "Sub-Poissonian photon statistics in resonance fluorescence". *Optics Letters* 4.7 (1979), pp. 205–207.

[107] F. M. Miatto, A. Safari, and R. W. Boyd. "Explicit formulas for photon number discrimination with on/off detectors". *Applied Optics* 57.23 (2018), p. 6750.

[108] D. Achilles, C. Silberhorn, and I. A. Walmsley. "Direct, loss-tolerant characterization of nonclassical photon statistics". *Physical Review Letters* 97.4 (2006), p. 043602.

[109] D. Achilles, C. Silberhorn, C. Sliwa, et al. "Photon-number-resolving detection using time-multiplexing". *Journal of Modern Optics* 51.9-10 (2004), pp. 1499–1515.

[110] R. Kruse, J. Tiedau, T. J. Bartley, S. Barkhofen, and C. Silberhorn. "Limits of the time-multiplexed photon-counting method". *Physical Review A* 95.2 (2017), p. 023815.

[111] K. Laiho, M. Schmidt, H. Suchomel, et al. "Photon-number parity of heralded single photons from a Bragg-reflection waveguide reconstructed loss-tolerantly via moment generating function". *New Journal of Physics* 21.10 (2019), p. 103025.

[112] M. Bohmann, J. Tiedau, T. Bartley, et al. "Incomplete detection of nonclassical phase-space distributions". *Physical Review Letters* 120.6 (2018), p. 63607.

[113] Swabian Instruments. *https://www.swabianinstruments.com/static/documentation/ TimeTagger/index.html 03.2020*.

[114] J. Sperling, W. Vogel, and G. S. Agarwal. "Sub-binomial light". *Physical Review Letters* 109.9 (2012), p. 093601.

[115] J. Hald, J. Sorensen, C. Schori, and E. Polzik. "Spin squeezed atoms: a macroscopic entangled ensemble created by light". *Physical Review Letters* 83.7 (1999), pp. 1319–1322.

[116] B. Vlastakis, G. Kirchmair, Z. Leghtas, et al. "Deterministically encoding quantum information using 100-photon Schroedinger cat states". *Science* 342.6158 (2013), pp. 607–610.

[117] M. Malik, M. Mirhosseini, M. P. Lavery, et al. "Direct measurement of a 27-dimensional orbital-angular-momentum state vector". *Nature communications* 5.1 (2014), p. 3115.

[118] H. Bernien, S. Schwartz, A. Keesling, et al. “Probing many-body dynamics on a 51-atom quantum simulator”. *Nature* 551.7682 (2017), pp. 579–584.

[119] J. Zhang, G. Pagano, P. W. Hess, et al. “Observation of a many-body dynamical phase transition with a 53-qubit quantum simulator”. *Nature* 551.7682 (2017), pp. 601–604.

[120] M. Yukawa, R. Ukai, P. Van Loock, and A. Furusawa. “Experimental generation of four-mode continuous-variable cluster states”. *Physical Review A* 78.1 (2008), p. 012301.

[121] M. Chen, N. C. Menicucci, and O. Pfister. “Experimental realization of multipartite entanglement of 60 modes of a quantum optical frequency comb”. *Physical Review Letters* 112.12 (2014), p. 120505.

[122] J. Roslund, R. M. De Araujo, S. Jiang, C. Fabre, and N. Treps. “Wavelength-multiplexed quantum networks with ultrafast frequency combs”. *Nature Photonics* 8.2 (2014), pp. 109–112.

[123] S. Gerke, J. Sperling, W. Vogel, et al. “Full multipartite entanglement of frequency-comb Gaussian states”. *Physical Review Letters* 114.5 (2015), p. 050501.

[124] S. Gerke, J. Sperling, W. Vogel, et al. “Multipartite entanglement of a two-separable state”. *Physical Review Letters* 117.11 (2016), p. 110502.

[125] J. Wang, S. Paesani, Y. Ding, et al. “Multidimensional quantum entanglement with large-scale integrated optics”. *Science* 360.6386 (2018), pp. 285–291.

[126] M. Gong, M.-C. Chen, Y. Zheng, et al. “Genuine 12-qubit entanglement on a superconducting quantum processor”. *Physical Review Letters* 122.11 (2019), p. 110501.

[127] S. Takeda, K. Takase, and A. Furusawa. “On-demand photonic entanglement synthesizer”. *Science advances* 5.5 (2019), eaaw4530.

[128] B. Yadin, F. C. Binder, J. Thompson, et al. “Operational resource theory of continuous-variable nonclassicality”. *Physical Review X* 8.4 (2018), p. 041038.

[129] B. J. Metcalf, N. Thomas-Peter, J. B. Spring, et al. “Multiphoton quantum interference in a multiport integrated photonic device”. *Nature communications* 4.1 (2013), p. 1356.

[130] M. Tillmann, S.-H. Tan, S. E. Stoeckl, et al. “Generalized multiphoton quantum interference”. *Physical Review X* 5.4 (2015), p. 041015.

[131] L. Rigovacca, C. Di Franco, B. J. Metcalf, I. A. Walmsley, and M. Kim. “Nonclassicality criteria in multiport interferometry”. *Physical Review Letters* 117.21 (2016), p. 213602.

[132] A. J. Menssen, A. E. Jones, B. J. Metcalf, et al. “Distinguishability and many-particle interference”. *Physical Review Letters* 118.15 (2017), p. 153603.

[133] S. Agne, T. Kauten, J. Jin, et al. “Observation of genuine three-photon interference”. *Physical review letters* 118.15 (2017), p. 153602.

[134] A. Navarrete, W. Wang, F. Xu, and M. Curty. “Characterizing multi-photon quantum interference with practical light sources and threshold single-photon detectors”. *New Journal of Physics* 20.4 (2018), p. 043018.

[135] T. Nitsche, S. De, S. Barkhofen, et al. “Local versus global two-photon interference in quantum networks”. *arXiv:2005.07219* (2020).

[136] M. Bentivegna, N. Spagnolo, C. Vitelli, et al. “Bayesian approach to boson sampling validation”. *International Journal of Quantum Information* 12.07n08 (2015), p. 1560028.

[137] J. Carolan, J. D. Meinecke, P. J. Shadbolt, et al. “On the experimental verification of quantum complexity in linear optics”. *Nature Photonics* 8.8 (2014), pp. 621–626.

[138] L. Aolita, C. Gogolin, M. Kliesch, and J. Eisert. “Reliable quantum certification of photonic state preparations”. *Nature communications* 6.1 (2015), p. 8498.

[139] M. Walschaers, J. Kuipers, J.-D. Urbina, et al. “Statistical benchmark for boson sampling”. *New Journal of Physics* 18.3 (2016), p. 032001.

[140] T. Giordani, F. Flamini, M. Pompili, et al. “Experimental statistical signature of many-body quantum interference”. *Nature Photonics* 12.3 (2018), pp. 173–178.

[141] D. Phillips, M. Walschaers, J. Renema, et al. “Benchmarking of Gaussian boson sampling using two-point correlators”. *Physical Review A* 99.2 (2019), p. 023836.

[142] J. Sperling, W. Vogel, and G. Agarwal. “Correlation measurements with on-off detectors”. *Physical Review A* 88.4 (2103), p. 043821.

[143] J. Sperling, M. Bohmann, W. Vogel, et al. “Uncovering quantum correlations with time-multiplexed click detection”. *Physical Review Letters* 115.2 (2015), p. 023601.

[144] J. Tiedau, E. Meyer-Scott, T. J. Bartley, and C. Silberhorn. *Patent pending DE 10 2017 129 490.2*. 2017.

[145] J. Tiedau, E. Meyer-Scott, T. Nitsche, et al. “A high dynamic range optical detector for measuring single photons and bright light”. *Optics Express* 27.1 (2019), pp. 1–15.

[146] G. A. P. Thé and R. V. Ramos. “Multiple-photon number resolving detector using fibre ring and single-photon detector”. *Journal of Modern Optics* 54.8 (2007), pp. 1187–1202.

[147] S. A. Castelletto, I. P. Degiovanni, V. Schettini, and A. L. Migdall. “Reduced deadtime and higher rate photon-counting detection using a multiplexed detector array”. *Journal of Modern Optics* 54.2-3 (2007), pp. 337–352.

[148] V. Schettini, S. V. Polyakov, I. P. Degiovanni, et al. “Implementing a multiplexed system of detectors for higher photon counting rates”. *IEEE Journal on Selected Topics in Quantum Electronics* 13.4 (2007), pp. 978–983.

[149] A. Divochiy, F. Marsili, D. Bitauld, et al. “Superconducting nanowire photon-number-resolving detector at telecommunication wavelengths”. *Nature Photonics* 2.5 (2008), pp. 302–306.

[150] M. Mičuda, O. Haderka, and M. Ježek. “High-efficiency photon-number-resolving multichannel detector”. *Physical Review A* 78.2 (2008), p. 025804.

[151] G. Brida, I. P. Degiovanni, F. Piacentini, et al. “Scalable multiplexed detector system for high-rate telecom-band single-photon detection”. *Review of Scientific Instruments* 80.11 (2009), p. 116103.

[152] E. Pomarico, B. Sanguinetti, R. Thew, and H. Zbinden. “Room temperature photon number resolving detector for infared wavelengths”. *Optics Express* 18.10 (2010), pp. 10750–10759.

[153] M. S. Allman, V. B. Verma, M. Stevens, et al. “A near-infrared 64-pixel superconducting nanowire single photon detector array with integrated multiplexed readout”. *Applied Physics Letters* 106.19 (2015), p. 192601.

[154] E. E. Wollman, V. B. Verma, A. E. Lita, et al. “Kilopixel array of superconducting nanowire single-photon detectors”. *Optics Express* 27.24 (2019), pp. 35279–35289.

[155] T. Gerrits, B. Calkins, N. Tomlin, et al. “Extending single-photon optimized superconducting transition edge sensors beyond the single-photon counting regime”. *Optics InfoBase Conference Papers* 20.21 (2012), pp. 23798–23810.

[156] J. G. Webb and E. H. Huntington. “Photostatistics reconstruction via loop detector signatures”. *Optics Express* 17.14 (2009), pp. 11799–11812.

[157] C. Lee, S. Ferrari, W. H. Pernice, and C. Rockstuhl. “Sub-Poisson-binomial light”. *Physical Review A* 94.5 (2016), p. 053844.

[158] T. Nitsche, F. Elster, J. Novotný, et al. “Quantum walks with dynamical control: Graph engineering, initial state preparation and state transfer”. *New Journal of Physics* 18.6 (2016), p. 063017.

[159] F. Marsili, V. B. Verma, J. A. Stern, et al. “Detecting single infrared photons with 93% system efficiency”. *Nature Photonics* 7.3 (2013), pp. 210–214.

[160] T. Gerrits, A. Migdall, J. C. Bienfang, et al. “Calibration of free-space and fiber-coupled single-photon detectors”. *Metrologia* 57.1 (2020), p. 015002.

[161] L. Mandel. “Squeezed states and sub-poissonian photon statistics”. *Physical Review Letters* 49.2 (1982), pp. 136–138.

[162] T. Eberle, S. Steinlechner, J. Bauchrowitz, et al. “Quantum enhancement of the zero-area sagnac interferometer topology for gravitational wave detection”. *Physical Review Letters* 104.25 (2010), pp. 251102–251103.

[163] L. Chen, D. Schwarzer, V. B. Verma, et al. “Mid-infrared laser-induced fluorescence with nanosecond time resolution using a superconducting nanowire single-photon detector: new technology for molecular science”. *Accounts of Chemical Research* 50.6 (2017), pp. 1400–1409.

[164] A. N. McCaughan. “Readout architectures for superconducting nanowire single photon detectors”. *Superconductor Science and Technology* 31.4 (2018), pp. 31–35.

[165] J. Tiedau, T. Schapeler, V. Anant, et al. “Single-channel electronic readout of a multipixel superconducting nanowire single photon detector”. *Optics Express* 28.4 (2020), pp. 5528–5537.

[166] L. You, X. Yang, Y. He, et al. “Jitter analysis of a superconducting nanowire single photon detector”. *AIP Advances* 3.7 (2013), p. 072135.

[167] K. E. Cahill and R. J. Glauber. “Ordered expansions in boson amplitude operators”. *Physical Review* 177.5 (1969), pp. 1857–1881.

[168] S. Wallentowitz and W. Vogel. “Unbalanced homodyning for quantum state measurements”. *Physical Review A* 53.6 (1996), pp. 4528–4533.

[169] E. Wigner. “On the quantum correction for thermodynamic equlilbrium”. *Physical Review* 40.5 (1932), pp. 749–759.

[170] J. Eisert, S. Scheel, and M. B. Plenio. “Distilling Gaussian states with Gaussian operations is impossible”. *Physical Review Letters* 89.13 (2002), p. 137903.

[171] D. Gottesman. “The Heisenberg representation of quantum computers”. *International Conference on Group Theoretic Methods in Physics* (1998), p. 9807006.

[172] S. Lloyd and S. L. Braunstein. “Quantum computation over continuous variables”. *Physical Review Letters* 82.8 (1999), pp. 1784–1787.

[173] J. Niset, J. Fiurášek, and N. J. Cerf. “No-go theorem for Gaussian quantum error correction”. *Physical Review Letters* 102.12 (2009), p. 120501.

[174] H.-A. Bachor and T. C. Ralph. *A guide to experiments in quantum optics*. Wiley, 2019.

[175] R. E. Slusher, L. W. Hollberg, B. Yurke, J. C. Mertz, and J. F. Valley. “Observation of squeezed states generated by four-wave mixing in an optical cavity”. *Physical Review Letters* 55.22 (1985), pp. 2409–2412.

[176] K. Vogel and H. Risken. “Determination of quasiprobability distributions in terms of probability distributions for the rotated quadrature phase”. *Physical Review A* 40.5 (1989), pp. 2847–2849.

[177] D. T. Smithey, M. Beck, M. G. Raymer, and A. Faridani. “Measurement of the Wigner distribution and the density matrix of a light mode using optical homodyne tomography: Application to squeezed states and the vacuum”. *Physical Review Letters* 70.9 (1993), pp. 1244–1247.

[178] L. A. Wu, H. J. Kimble, J. L. Hall, and H. Wu. “Generation of squeezed states by parametric down conversion”. *Physical Review Letters* 57.20 (1986), pp. 2520–2523.

[179] W. Vogel. “Homodyne correlation measurements with weak local oscillators”. *Physical Review A* 51.5 (1995), pp. 4160–4171.

[180] K. Banaszek and K. Wódkiewicz. “Direct probing of quantum phase space by photon counting”. *Physical Review Letters* 76.23 (1996), pp. 4344–4347.

[181] A. Royer. “Wigner function as the expectation value of a parity operator”. *Physical Review A* 15.2 (1977), pp. 449–450.

[182] A. Royer. “Measurement of the Wigner function”. *Physical Review Letters* 55.25 (1985), pp. 2745–2748.

[183] K. Banaszek, C. Radzewicz, K. Wódkiewicz, and J. S. Krasiński. “Direct measurement of the Wigner function by photon counting”. *Physical Review A* 60.1 (1999), pp. 674–677.

[184] A. Allevi, A. Andreoni, M. Bondani, et al. “State reconstruction by on/off measurements”. *Physical Review A* 80.2 (2009), p. 022114.

[185] K. Laiho, K. N. Cassemiro, D. Gross, and C. Silberhorn. “Probing the negative wigner function of a pulsed single photon point by point”. *Physical Review Letters* 105.25 (2010), p. 253603.

[186] D. Mogilevtsev. “Diagonal element inference by direct detection”. *Optics Communications* 156.4-6 (1998), pp. 307–310.

[187] D. Mogilevtsev. “Reconstruction of quantum states with binary detectors”. *Acta Physica Slovaca*. Vol. 49. 4. 1999, pp. 743–748.

[188] A. R. Rossi, S. Olivares, and M. G. Paris. “Photon statistics without counting photons”. *Physical Review A* 70.5 (2004), p. 55801.

[189] A. R. Rossi and M. G. Paris. “A two-step MaxLik-MaxEnt strategy to infer photon distribution from on/off measurement at low quantum efficiency”. *European Physical Journal D* 32.2 (2005), pp. 223–226.

[190] G. Zambra, A. Andreoni, M. Bondani, et al. “Experimental reconstruction of photon statistics without photon counting”. *Physical Review Letters* 95.6 (2005), p. 063602.

[191] G. Harder, D. Mogilevtsev, N. Korolkova, and C. Silberhorn. “Tomography by noise”. *Physical Review Letters* 113.7 (2014), p. 070403.

[192] P. Kumar and C. Kim. “Quadrature-squeezed light detection using a self-generated matched local oscillator”. *Optics and Photonics News* 5.12 (1994), pp. 26–27.

[193] K. Laiho, M. Avenhaus, K. N. Cassemiro, and C. Silberhorn. “Direct probing of the Wigner function by time-multiplexed detection of photon statistics”. *New Journal of Physics* 11.4 (2009), p. 043012.

[194] D. Mogilevtsev, J. Řeháček, and Z. Hradil. “Relative tomography of an unknown quantum state”. *Physical Review A* 79.2 (2009), p. 020101.

[195] V. S. Shchesnovich. “Partial indistinguishability theory for multiphoton experiments in multiport devices”. *Physical Review A* 91.1 (2015), p. 13844.

[196] V. S. Shchesnovich. “Sufficient condition for the mode mismatch of single photons for scalability of the boson-sampling computer”. *Physical Review A* 89.2 (2014), p. 022333.

[197] J. J. Renema, A. Menssen, W. R. Clements, et al. “Efficient classical algorithm for boson sampling with partially distinguishable photons”. *Physical Review Letters* 120.22 (2018), p. 220502.

[198] M. Bellini, F. Marin, S. Viciani, A. Zavatta, and F. T. Arecchi. “Nonlocal pulse shaping with entangled photon pairs”. *Physical Review Letters* 90.4 (2003), p. 43602.

[199] A. Pe’er, B. Dayan, A. A. Friesem, and Y. Silberberg. “Temporal shaping of entangled photons”. *Physical Review Letters* 94.7 (2005), p. 073601.

[200] A. Valencia, A. Ceré, X. Shi, G. Molina-Terriza, and J. P. Torres. “Shaping the waveform of entangled photons”. *Physical Review Letters* 99.24 (2007), p. 243601.

[201] A. Eckstein, B. Brecht, and C. Silberhorn. “A quantum pulse gate based on spectrally engineered sum frequency generation”. *Optics Express* 19.15 (2011), pp. 13770–13778.

[202] B. Brecht, A. Eckstein, A. Christ, H. Suche, and C. Silberhorn. “From quantum pulse gate to quantum pulse shaper - Engineered frequency conversion in nonlinear optical waveguides”. *New Journal of Physics* 13.6 (2011), p. 065029.

[203] D. V. Reddy, M. G. Raymer, C. J. McKinstrie, L. Mejling, and K. Rottwitt. “Temporal mode selectivity by frequency conversion in second-order nonlinear optical waveguides”. *Optics Express* 21.11 (2013), pp. 13840–13863.

[204] B. Brecht, A. Eckstein, R. Ricken, et al. “Demonstration of coherent time-frequency Schmidt mode selection using dispersion-engineered frequency conversion”. *Physical Review A* 90.3 (2014), p. 030302.

[205] I. Agha, S. Ates, L. Sapienza, and K. Srinivasan. “Spectral broadening and shaping of nanosecond pulses: toward shaping of single photons from quantum emitters”. *Optics Letters* 39.19 (2014), pp. 5677–5680.

[206] K. E. Dorfman, F. Schlawin, and S. Mukamel. “Stimulated Raman spectroscopy with entangled light: enhanced resolution and pathway selection”. *Journal of Physical Chemistry Letters* 5.16 (2014), pp. 2843–2849.

[207] R. W. Andrews, A. P. Reed, K. Cicak, J. D. Teufel, and K. W. Lehnert. “Quantum-enabled temporal and spectral mode conversion of microwave signals”. *Nature Communications* 6.1 (2015), p. 10021.

[208] B. Brecht, D. V. Reddy, C. Silberhorn, and M. G. Raymer. “Photon temporal modes: a complete framework for quantum information science”. *Physical Review X* 5.4 (2015), p. 41017.

[209] P. Manurkar, N. Jain, M. Silver, et al. “Multidimensional mode-separable frequency conversion for high-speed quantum communication”. *Optica* 3.12 (2016), pp. 1300–1307.

[210] P. Manurkar, N. Jain, P. Kumar, and G. S. Kanter. “Programmable optical waveform reshaping on a picosecond timescale”. *Optics Letters* 42.5 (2017), pp. 951–954.

[211] V. Ansari, J. M. Donohue, M. Allgaier, et al. “Tomography and purification of the temporal-mode structure of quantum light”. *Physical Review Letters* 120.21 (2018), p. 213601.

[212] C. Polycarpou, K. N. Cassemiro, G. Venturi, A. Zavatta, and M. Bellini. “Adaptive detection of arbitrarily shaped ultrashort quantum light states”. *Physical Review Letters* 109.5 (2012), p. 053602.

[213] K. N. Cassemiro, K. Laiho, and C. Silberhorn. “Accessing the purity of a single photon by the width of the Hong-Ou-Mandel interference”. *New Journal of Physics* 12.11 (2010), p. 113052.

[214] J. Tiedau, V. S. Shchesnovich, D. Mogilevtsev, et al. “Quantum state and mode profile tomography by the overlap”. *New Journal of Physics* 20.3 (2018), p. 033003.

[215] J. Řeháček, D. Mogilevtsev, and Z. Hradil. "Operational tomography: Fitting of data patterns". *Physical Review Letters* 105.1 (2010), p. 10402.

[216] D. Mogilevtsev, A. Ignatenko, A. Maloshtan, et al. "Data pattern tomography: reconstruction with an unknown apparatus". *New Journal of Physics* 15.2 (2013), p. 025038.

[217] G. Harder, C. Silberhorn, J. Rehacek, et al. "Time-multiplexed measurements of non-classical light at telecom wavelengths". *Physical Review A* 90.4 (2014), p. 042105.

[218] M. Cooper, M. Karpiński, and B. J. Smith. "Local mapping of detector response for reliable quantum state estimation". *Nature Communications* 5.1 (2014), p. 4332.

[219] L. Motka, B. Stoklasa, J. Rehacek, et al. "Efficient algorithm for optimizing data-pattern tomography". *Physical Review A* 89.5 (2014), pp. 4–8.

[220] Y. Shechtman, Y. C. Eldar, O. Cohen, et al. "Phase retrieval with application to optical imaging". *IEEE signal processing magazine* 32.3 (2015), pp. 87–109.

[221] D. N. Klyshko. "Use of two-photon light for absolute calibration of photoelectric detectors". *Soviet journal of quantum electronics* 7.9 (1980), p. 1112.

[222] V. Makarov. "Controlling passively quenched single photon detectors by bright light". *New Journal of Physics* 11.6 (2009), p. 065003.

[223] D. F. James, P. G. Kwiat, W. J. Munro, and A. G. White. "Measurement of qubits". *Physical Review A* 64.5 (2001), p. 052312.

[224] Z. Hradil, D. Mogilevtsev, and J. Čeháček. "Biased tomography schemes: An objective approach". *Physical Review Letters* 96.23 (2006), p. 230401.

[225] T. Moroder, P. Hyllus, G. Tóth, et al. "Permutationally invariant state reconstruction". *New Journal of Physics* 14.10 (2012), p. 105001.

[226] A. Luis, J. Sperling, and W. Vogel. "Nonclassicality phase-space functions: More insight with fewer detectors". *Physical Review Letters* 114.10 (2015), p. 103602.

[227] S. Pirandola, S. Mancini, S. Lloyd, and S. L. Braunstein. "Continuous-variable quantum cryptography using two-way quantum communication". *Nature Physics* 4.9 (2008), pp. 726–730.

[228] L. S. Madsen, V. C. Usenko, M. Lassen, R. Filip, and U. L. Andersen. "Continuous variable quantum key distribution with modulated entangled states". *Nature Communications* 3.1 (2012), p. 1083.

[229] P. Jouguet, S. Kunz-Jacques, A. Leverrier, P. Grangier, and E. Diamanti. "Experimental demonstration of long-distance continuous-variable quantum key distribution". *Nature Photonics* 7.5 (2013), pp. 378–381.

[230] B. Heim, C. Peuntinger, N. Killoran, et al. "Atmospheric continuous-variable quantum communication". *New Journal of Physics* 16.11 (2014), p. 113018.

[231] W. Idler, F. Buchali, L. Schmalen, et al. "Field demonstration of 1 Tbit/s super-channel network using probabilistically shaped constellations". *European Conference on Optical Communication, ECOC* 35.8 (2016), pp. 1–3.

[232] M. Santandrea, M. Stefszky, V. Ansari, and C. Silberhorn. “Fabrication limits of waveguides in nonlinear crystals and their impact on quantum optics applications”. *New Journal of Physics* 21.3 (2019), p. 033038.

[233] W. E. Lamb Jr. “Theory of an optical maser”. *Physical Review* 134.6A (1964), A1429–A1450.

[234] L. E. Hargrove, R. L. Fork, and M. A. Pollack. “Locking of hene laser modes induced by synchronous intracavity modulation”. *Applied Physics Letters* 5.1 (1964), p. 4.

[235] H. W. Mocker and R. J. Collins. “Mode competition and self-locking effects in a q-switched ruby laser”. *Applied Physics Letters* 7.10 (1965), pp. 270–273.

[236] M. Ivanov, P. B. Corkum, T. Zuo, and A. Bandrauk. “Routes to control of intense-field atomic polarizability”. *Physical Review Letters* 74.15 (1995), pp. 2933–2936.

[237] L. Xu, T. W. Hänsch, C. Spielmann, et al. “Route to phase control of ultrashort light pulses”. *Optics Letters* 21.24 (1996), pp. 2008–2010.

[238] J. Reichert, R. Holzwarth, T. Udem, and T. W. Hänsch. “Measuring the frequency of light with mode-locked lasers”. *Optics Communications* 172.1-6 (1999), pp. 59–68.

[239] H. R. Telle, G. Steinmeyer, A. E. Dunlop, et al. “Carrier-envelope offset phase control: A novel concept for absolute optical frequency measurement and ultrashort pulse generation”. *Applied Physics B* 69.4 (1999), pp. 327–332.

[240] A. Baltuska, T. Udem, M. Uiberacker, et al. “Attosecond control of electronic processes”. *Nature* 421.6923 (2003), pp. 611–615.

[241] F. Krausz and M. Ivanov. “Attosecond physics”. *Reviews of Modern Physics* 81.1 (2009), pp. 163–234.

[242] Alfano R.R. and Shapiro S.L. “Emission in the region 4000 to 7000Å via four-photon coupling in glass”. *Physical Review Letters* 24.11 (1970), pp. 584–588.

[243] D. von der Linde. “Characterization of the noise in countinously operating mode-locked lasers”. *Applied Physics B* 39.4 (1986), pp. 201–217.

[244] J. Kim, J. Chen, J. Cox, and F. X. Kärtner. “Attosecond-resolution timing jitter characterization of free-running mode-locked lasers”. *Optics letters* 32.24 (2007), pp. 3519–3521.

[245] J. Kim and F. X. Kärtner. “Attosecond-precision ultrafast photonics”. *Laser and Photonics Reviews* 4.3 (2010), pp. 432–456.

[246] T. Miura, H. Nagaoka, K. Takasago, et al. “Active synchronization of two mode-locked lasers with optical cross correlation”. *Applied Physics B* 75.1 (2002), pp. 19–23.

[247] T. K. Kim, Y. Song, K. Jung, et al. “Sub-100-as timing jitter optical pulse trains from mode-locked Er-fiber lasers”. *Optics Letters* 36.22 (2011), pp. 4443–4445.

[248] Y. Song, C. Kim, K. Jung, H. Kim, and J. Kim. “Timing jitter optimization of mode-locked Yb-fiber lasers toward the attosecond regime”. *Optics Express* 19.15 (2011), pp. 14518–14525.

[249] A. J. Benedick, U. Demirbas, D. Li, J. G. Fujimoto, and F. X. Kärtner. "Attosecond Ti:sapphire pulse train phase noise". *CLEO: 2011-Laser Science to Photonic Applications*. 2011, pp. 1–2.

[250] J. Millo, R. Boudot, M. Lours, et al. "Ultra-low-noise microwave extraction from fiber-based optical frequency comb". *Optics Letters* 34.23 (2009), pp. 3707–3709.

[251] T. M. Fortier, M. S. Kirchner, F. Quinlan, et al. "Generation of ultrastable microwaves via optical frequency division". *Nature Photonics* 5.7 (2011), pp. 425–429.

[252] F. Quinlan, T. M. Fortier, M. S. Kirchner, et al. "Ultralow phase noise microwave generation with an Er:fiber-based optical frequency divider". *Optics Letters* 36.16 (2011), pp. 3260–3262.

[253] K. Jung and J. Kim. "Subfemtosecond synchronization of microwave oscillators with mode-locked Er-fiber lasers". *Optics Letters* 37.14 (2012), pp. 2958–2960.

[254] W. Zhang, S. Seidelin, A. Joshi, et al. "Dual photo-detector system for low phase noise microwave generation with femtosecond lasers". *Optics Letters* 39.5 (2014), pp. 1204–1207.

[255] M. Y. Peng, A. Kalaydzhyan, and F. X. Kärtner. "Balanced optical-microwave phase detector for sub-femtosecond optical-RF synchronization". *Optics Express* 22.22 (2014), pp. 27102–27111.

[256] M. Bahmanian, J. Tiedau, C. Silberhorn, and J. C. Scheytt. "Octave-band microwave frequency synthesizer using mode-locked laser as a reference". *2019 IEEE International Topical Meeting on Microwave Photonics, MWP 2019*. 2019, pp. 1–4.

[257] A. H. Nejadmalayeri and F. X. Kärtner. "Mach-Zehnder based balanced optical microwave phase detector". *Conference on Lasers and Electro-Optics 2012*. 2012, CTu2A.1.

[258] O. Prochnow, R. Paschotta, E. Benkler, et al. "Quantum-limited noise performance of a femtosecond all-fiber ytterbium laser". *Optics Express* 17.18 (2009), pp. 15525–15533.

[259] E. Portuondo-Campa, R. Paschotta, and S. Lecomte. "Sub-100 attosecond timing jitter from low-noise passively mode-locked solid-state laser at telecom wavelength". *Optics Letters* 38.15 (2013), pp. 2650–2653.

[260] H. A. Haus and A. Mecozzi. "Noise of mode-locked lasers". *IEEE Journal of Quantum Electronics* 29.3 (1993), pp. 983–996.

[261] R. Paschotta. "Noise of mode-locked lasers (Part I): numerical model". *Applied Physics B* 79.2 (2004), pp. 153–162.

[262] R. Paschotta. "Noise of mode-locked lasers (Part II): timing jitter and other fluctuations". *Applied Physics B* 79.2 (2004), pp. 163–173.

[263] R. Paschotta. "Timing jitter and phase noise of mode-locked fiber lasers". *Optics Express* 18.5 (2010), pp. 5041–5054.

[264] F. Quinlan, T. M. Fortier, H. Jiang, and S. A. Diddams. "Analysis of shot noise in the detection of ultrashort optical pulse trains". *JOSA B* 30.6 (2013), pp. 1775–1785.

[265] B. Lamine, C. Fabre, and N. Treps. "Quantum improvement of time transfer between remote clocks". *Physical Review Letters* 101.12 (2008), p. 123601.

[266] S. Wang, X. Xiang, N. Treps, et al. "Sub-shot-noise interferometric timing measurement with a squeezed frequency comb". *Physical Review A* 98.5 (2018), p. 053821.

[267] F. Quinlan, T. M. Fortier, H. Jiang, et al. "Exploiting shot noise correlations in the photodetection of ultrashort optical pulse trains". *Nature Photonics* 7.4 (2013), pp. 290–293.

[268] S. Schmitt, J. Ficker, M. Wolff, et al. "Photon-number squeezed solitons from an asymmetric fiber-optic sagnac interferometer". *Physical Review Letters* 81.12 (1998), pp. 2446–2449.

[269] J. A. Cox, A. H. Nejadmalayeri, J. Kim, and F. X. Kärtner. "Complete characterization of quantum-limited timing jitter in passively mode-locked fiber lasers". *Optics Letters* 35.20 (2010), pp. 3522–3524.

[270] A. Kuzmich, I. A. Walmsley, and L. Mandel. "Violation of Bell's inequality by a generalized Einstein-Podolsky-Rosen state using homodyne detection". *Physical Review Letters* 85.7 (2000), pp. 1349–1353.

[271] K. J. Resch, J. S. Lundeen, and A. M. Steinberg. "Quantum state preparation and conditional coherence". *Physical Review Letters* 88.11 (2002), p. 113601.

[272] G. Donati, T. J. Bartley, X. M. Jin, et al. "Observing optical coherence across Fock layers with weak-field homodyne detectors". *Nature Communications* 5.1 (2014), p. 5584.

[273] K. Wódkiewicz and M. S. Zubairy. "Effect of laser fluctuations on squeezed states in a degenerate parametric amplifier". *Physical Review A* 27.4 (1983), pp. 2003–2007.

[274] D. D. Crouch and S. L. Braunstein. "Limitations to squeezing in a parametric amplifier due to pump quantum fluctuations". *Physical Review A* 38.9 (1988), pp. 4696–4711.

[275] P. K. Lam, T. C. Ralph, B. C. Buchler, et al. "Optimization and transfer of vacuum squeezing from an optical parametric oscillator". *Journal of Optics B* 1.4 (1999), pp. 469–474.

[276] T. Aoki, G. Takahashi, and A. Furusawa. "Squeezing at 946nm with periodically poled KTiOPO 4". *Optics Express* 14.15 (2006), pp. 6930–6935.

[277] G. Harder, C. Silberhorn, J. Rehacek, et al. "Local sampling of the wigner function at telecom wavelength with loss-tolerant detection of photon statistics". *Physical Review Letters* 116.13 (2016), p. 133601.

[278] H. Vahlbruch, M. Mehmet, K. Danzmann, and R. Schnabel. "Detection of 15 dB squeezed states of light and their application for the absolute calibration of photoelectric quantum efficiency". *Physical Review Letters* 117.11 (2016), p. 110801.

[279] P. Bierhorst, E. Knill, S. Glancy, et al. "Experimentally generated randomness certified by the impossibility of superluminal signals". *Nature* 556.7700 (2018), pp. 223–226.

[280] L. Lachman, I. Straka, J. Hloušek, M. Ježek, and R. Filip. "Faithful hierarchy of genuine n -photon quantum non-gaussian light". *Physical Review Letters* 123.4 (2019), p. 043601.

[281] A. I. Lvovsky, R. Ghobadi, A. Chandra, A. S. Prasad, and C. Simon. "Observation of micro-macro entanglement of light". *Nature Physics* 9.9 (2013), pp. 541–544.

[282] N. Bruno, A. Martin, P. Sekatski, et al. "Displacement of entanglement back and forth between the micro and macro domains". *Nature Physics* 9.9 (2013), pp. 545–548.

[283] M. Bohmann and E. Agudelo. "Phase-space inequalities beyond negativities". *Physical Review Letters* 124.13 (2020), p. 133601.

[284] V. Ansari, E. Roccia, M. Santandrea, et al. "Heralded generation of high-purity ultrashort single photons in programmable temporal shapes". *Optics Express* 26.3 (2018), pp. 2764–2774.

Acknowledgements

First and foremost, I would like to thank Professor Dr. Christine Silberhorn for giving me the opportunity to work on this wonderful topic. I really enjoyed working in your group and under your supervision. Thank you for always having an open ear for my questions, great discussions, and for helping me to develop plans beyond my PhD. Your attentive, family-friendly way of managing the group really made a difference for us and the regular group events were a lot of fun for my whole family.

Secondly, I would like to thank J.-Professor Dr. Tim Bartley. I learned a lot from you through many great discussions, your very encouraging way, and your support in my projects.

I also want to thank the European Union for funding my work within the 'QUCUMbER' and 'PhoG' project.

I had the luxury of having many great collaborators outside Paderborn and I would like to thank all of them. Especially: Martin Bohmann, Thomas Dirmeier, Thomas Gerrits, Natalia Korolkova, Christoph Marquardt, and Dmitri Mogilevtsev.

When I arrived in Paderborn, Georg helped me to get into the topic. Thank you Georg for teaching me a lot about quantum physics and preparing many basic steps for my work. Also thanks to Vahid for sharing his amazing lab experience and Victor, Laura, Raimund, and Christof for realizing my weird coatings and crystal wishlists. Thanks also to Kai, Sonja and Jan-Philipp for many chats and Timon for analyzing my detector-readout-scheme data.

For all colleagues, I shared a lab with: Regina, Thomas, Syam, Nidhin, Evan, Melanie (also for sharing an office with me) thanks for the great time and many fun moments (when we figured out after three hours that we should better plug in the power cable).

Moreover, I am grateful to Jan, Michael, and Benni for so many great discussions about physics. It is always so interesting and helpful to talk to you!

Also many thanks to Benni and Evan for reading my thesis and giving me great comments.

Special thanks to Evan for being such a great physics role model for me. I am so happy that I met you, shared an office with you and had the privilege of becoming friends with you.

From the administration, I would like to thank Rita, Petra, Kerstin, and Nadine for helping me to prepare all the important things and helping me to fill out my forms.

I would also like to thank Meysam and Professor Dr. Christoph Scheytt for borrowing the signal source analyzer and many great discussions about noise properties.

Also, thanks to Professor Dr. Uwe Morgner for helping me to understand ultrafast laser systems and Helmut Fedder and Michael Schlagmüller for answering my questions about time taggers.

I also want to thank my family for their support and help.

Last but not least, I want to thank my wonderful wife Miriam for her support and love.

A List of scientific contributions

A.1 Publications

(1) Benchmarking the future-proofedness of photonic quantum systems

Tiedau, Johannes and Engelkemeier, Melanie and Brecht, Benjamin and Sperling, Jan and Silberhorn, Christine
Manuscript in preparation

JT. build the TMD, perfomred the experiment and analyzed the raw data. M.E. build the PDC source. J.S. conceived the idea, performed the calculation and wrote the initial version of the manuscript. B.B. helped to supervise the project. C.S. supervised the work. All authors contributed to the final manuscript.

(2) Identifying ultrafast fs-squeezing with a genuinely local oscillator and photon counting

Tiedau, Johannes and Eigner, Christof and Quiring, Victor and Padberg, Laura and Ricken, Raimund and Sperling, Jan and Brecht, Benjamin and Bartley, Tim J and Silberhorn, Christine
2018 Conference on Lasers and Electro-Optics (CLEO). IEEE (2020)

J.T. conceived the idea of cutting the squeezing ellipse. J.T. build the setup, performed the experiment, analyzed the data and did the theoretical modeling. C.E., L.P and R.R. produced the KTP samples, C.E.,L.P. and V.Q. produced dielectric filters. J.S., B.B. and T.J.B. helped to supervise the project. C.S. supervised the work. J.T. prepared the first version of the manuscript. All authors contributed to the final manuscript.

(3) Single-channel electronic readout of a multipixel superconducting nanowire single photon detector

Tiedau, Johannes and Schapeler, Timon and Anant, Vikas and Fedder, Helmut and Silberhorn, Christine and Bartley, Tim J
Optics Express 28, 5528 (2020)

J.T. conceived the idea in discussions with H.F. and V.A.. J.T. performed the experiment. T.S. and J.T. analyzed the data. C.S. and T.J.B. supervised the work. All authors prepared the manuscript.

(4) Scalability of parametric down-conversion for generating higher-order Fock states

Tiedau, Johannes and Bartley, Tim J and Harder, Georg and Lita, Adriana E and Nam, Sae Woo and Gerrits, Thomas and Silberhorn, Christine
Physical Review A 100, 041802 (2019)

J.T. conceived the idea and found the connection to discrete phase-type distributions. T.J.B., G.H. and T.G. performed the experiment, J.T. analyzed the data and prepared the first version of the

manuscript. T.J.B. helped to supervise the work. C.S. supervised the work. All authors prepared the manuscript.

(5) A high dynamic range optical detector for measuring single photons and bright light

Tiedau, Johannes and Meyer-Scott, Evan and Nitsche, Thomas and Barkhofen, Sonja and Bartley, Tim J and Silberhorn, Christine
Optics express 27, 1 (2019)

J.T., T.J.B. and C.S. conceived the idea. J.T. developed the calibration routine. T.N. build the active setup with supervision help from S.B.. E.M.S. build the passive setup and performed the active measurements. J.T. performed the passive measurements and analyzed all data. T.J.B. and C.S. supervised the work. All authors prepared the manuscript.

(6) Quantum state and mode profile tomography by the overlap

Tiedau, Johannes and Shchesnovich, Valery S and Mogilevtsev, Dmitri and Ansari, Vahid and Harder, Georg and Bartley, Tim J and Korolkova, Natalia and Silberhorn, Christine
New Journal of Physics 20, 033003 (2018)

D.M. and N.K. conceived the idea and performed the calculations. J.T. build the setup and performed the measurement with support from G.H. and V.A. V.A. set up the PDC source. J.T. analyzed the raw data. V.S.S developed the multimode theory. N.K and C.S. supervised the work. All authors prepared the manuscript.

(7) Incomplete detection of nonclassical phase-space distributions

Bohmann, Martin and Tiedau, Johannes and Bartley, Tim J and Sperling, Jan and Silberhorn, Christine and Vogel, Werner
Physical review letters 120, 063607 (2018)

M.B. and J.S. conceived the idea and performed the calculations. J.T. performed the experiment and analyzed the raw data. T.J.B. helped to supervise the work. C.S. and W.V. supervised the work. All authors prepared the manuscript.

A.1.1 Additional publications

(8) Limits of the time-multiplexed photon-counting method

Kruse, Regina and Tiedau, Johannes and Bartley, Tim J and Barkhofen, Sonja and Silberhorn, Christine
Physical Review A 95.2, 023815 (2017)

(9) Discorrelated quantum states

Meyer-Scott, Evan and Tiedau, Johannes and Harder, Georg and Shalm, Lynden K and Bartley, Tim J
Scientific Reports 7, 41622 (2017)

(10) Extracting the physical sector of quantum states

Mogilevtsev, Dmitri and Teo, Yong-Siah and Řeháček, Jaroslav and Hradil, Zdenek and Tiedau, Johannes and Kruse, Regina and Harder, Georg and Silberhorn, Christine and Sanchez-Soto, Luis Lorenzo
New Journal of Physics 19.9, 093008 (2017)

(11) Limits on the heralding efficiencies and spectral purities of spectrally filtered single photons from photon-pair sources

Meyer-Scott, Evan and Montaut, Nicola and Tiedau, Johannes and Sansoni, Linda and Herrmann, Harald and Bartley, Tim J and Silberhorn, Christine
Physical Review A 95.6, 061803 (2017)

(12) Wave-particle duality revisited: Neither wave nor particle

Sperling, Jan and De, Syamsundar and Nitsche, Thomas and Tiedau, Johannes and Barkhofen, Sonja and Brecht, Benjamin and Silberhorn, Christine
arXiv:1907.09836 (2019)

(13) Octave-band microwave frequency synthesizer using mode-locked laser as a reference

Bahmanian, Meysam and Tiedau, Johannes and Silberhorn, Christine and Scheytt, J Christoph
2019 International Topical Meeting on Microwave Photonics, IEEE 083602 (2019)

(14) Distillation of Squeezing using an engineered PDC source

Dirmeier, Thomas and Tiedau, Johannes and Khan, Imran and Ansari, Vahid and Müller, Christian R and Silberhorn, Christine and Marquardt, Christoph and Leuchs, Gerd
arXiv:1907.08004 (2019)

(15) Local versus global two-photon interference in quantum networks

Nitsche, Thomas and De, Syamsundar and Barkhofen, Sonja and Meyer-Scott, Evan and Tiedau, Johannes and Sperling, Jan and Gábris, Aurél and Jex, Igor and Silberhorn, Christine
arXiv:2005.07219 (2020)

A.2 Patents pending

(I) Verfahren zur Messung der Photonenanzahl mittels eines Photonendetektors

Tiedau, Johannes and Meyer-Scott, Evan and Bartley, Tim J and Silberhorn, Christine
Az. DE 10 2017 129 490.2

(II) Verfahren zum Auslesen eines optischen Detektors

Tiedau, Johannes and Bartley, Tim J and Anant, Vikas and Fedder, Helmut and Silberhorn, Christine
Az. DE 10 2019 112 893.5

(III) Gradientenfilter zur strahlversatzfreien, wellenlängenselektiven Modifikation der Lichteigenschaften

Eigner, Christof and Padberg, Laura and Tiedau, Johannes and Quiring, Viktor and Silberhorn, Christine
Az. DE 10 2019 130 532.2

B High-gain measurements

As an application of our multimode theory derived in Sec. 2.3.3, we want to consider multimode effects for measurements in the high-gain regime. In general, measurements that post-select on a specific photon number (e.g. heralding higher-order Fock states) have to be distinguished from experiments that detect light based on the total photon number (e.g. photon subtraction). Both cases have in common that we want to increase events related to a specific mode. For the post-selection, we consider a specific photon number n' and the probability to generate this photon number $p_{n'}$ in our pre-specified mode. As discussed in Sec. 2.3.4 we can see that the heralding probability with respect to a specific mode decreases in general with increasing optical gain. This result is different for the second case, where the total number of photons $\bar{n}_k$ per mode k is relevant. For higher optical gain B the mean photon number $\bar{n}_k$ grows exponentially. As the dominant Schmidt mode grows faster than all other modes, the mean photon number is mainly determined by this mode: $\lim_{B\to\infty} \frac{\bar{n}_{k+1}}{\bar{n}_k} = 0$. This means, for example, that subtracting a photon from the dominant Schmidt mode of a multi-thermal state is advantageous for high optical gain.

These considerations also become apparent for a common measure of the Schmidt number, namely the unheralded $g^{(2)}$ measurement. As already pointed out in [36] the $g^{(2)}$ value is only related to the Schmidt number in the low gain regime because of a $\sinh(r_k) \approx r_k$ assumption in the derivation. In the following, however, we want to discuss the high gain regime further. The unheralded $g^{(2)}$ is defined as

$$g^{(2)}(0) = \frac{\langle n^2 \rangle - \langle n \rangle}{\langle n \rangle^2} \tag{B.1}$$

Figure B.1 illustrates how the $g^{(2)}$ value changes with increasing optical gain. We want to discuss three different aspects of this function.

Dominating mode

The dominating Schmidt mode grows faster than all other modes. For this reason, the measured (total) photon number is dominated by the first Schmidt mode for high optical gain values. Therefore the $g^{(2)}$ value approaches the single-mode case ($g^{(2)}_{\text{single mode}} = 2$) in the high gain regime because photons are mainly detected from the dominating mode (Fig. B.1 orange).

Detector saturation

In most cases, unheralded $g^{(2)}$ values are recorded with binary detectors in a Hanbury-Brown-Twiss configuration as these detectors offer many critical advantages (see Sec. 3.2). For high optical gain values, special care must be taken in order to avoid saturation effects. These effects will overestimate coincidences between the detectors, which results in a decreasing $g^{(2)}$ value (Fig. B.1 green). In order to compensate for saturation effects, additional variable attenuators can be added in front of the detectors in such a way that the count rate is kept constant while changing the optical pump power. This method is able to reproduce the precise $g^{(2)}$ measured

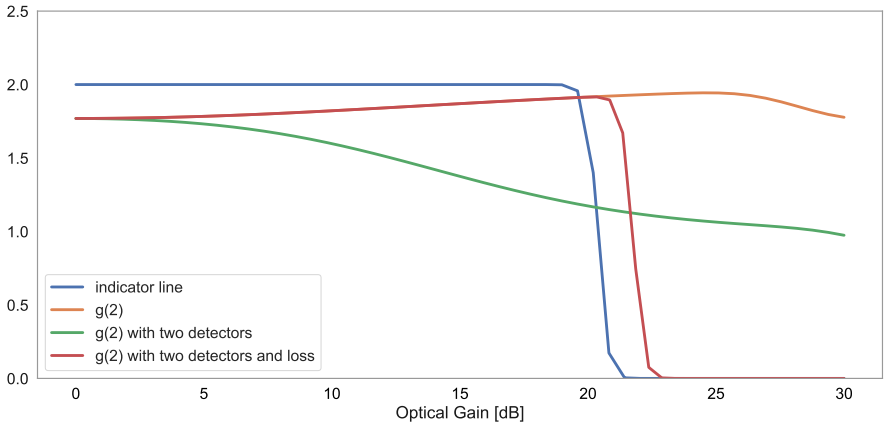

Figure B.1 – Comparison of unheralded $g^{(2)}$ measurements from photon number resolved measurements (orange) and binary click-detectors in a Hanbury-Brown-Twiss configuration (red and green). The photon detection rate is kept constant for the red case by adapting optical losses to the optical gain. Saturation effects will decrease the $g^{(2)}$ value if no additional attenuators are applied (green). The indicator line (blue) should have a constant value of two and shows, where numerical errors become apparent due to Hilbert space truncation ($n_{\max} = 500$). For example, the decrease of the orange line is caused by numerical errors.

with photon number resolving detectors (Fig. B.1 red, please mind the numerical errors in the plot).

Optical losses

Finally, we have shown that optical losses in the high gain regime can act differently on the individual Schmidt modes [84]. This effect can change the convolved photon number distribution (from a detector that cannot distinguish individual modes). However, for all practical situations, this effect is not visible for unheralded $g^{(2)}$ measurements.

In addition, we can also see numerical errors in Fig. B.1 resulting from the Hilbert space truncation at $n_{\max} = 500$. For this reason, values above 20 dB should be treated carefully. Note that we always consider a double Gaussian joint-spectral intensity here. The situation is different for specially designed Schmidt modes [284] with equal weighting, where the $g^{(2)}$ value is independent of the optical gain.

C Example code

C.1 get_gate

Listing C.1 – get_gate function in Python

```
class get_gate(Combiner):
    '''
    This class will generate a gate (virtual) channel.

    Parameters
    ----------
    tagger : tagger
        swabian time tagger
    trig_ch: int
        trigger channel number
    pos : array
        peak positions from histogram (in ps after trigger)
    window : long
        defines the measurement window for all time bins (in ps)

    Returns
    -------
    Gate : virtual_channel
        Gate channel for CountBetweenMarkers

    '''
    def __init__(self, tagger,trig_ch,pos,window):
        self.ch = [None]*(2*len(pos)+1)
        self.ch[0] =  DelayedChannel(tagger,trig_ch,0)
        for i,val in enumerate(pos):
            self.ch[2*(i+1)-1] =  DelayedChannel(tagger,trig_ch,val-window)
            self.ch[2*(i+1)] =  DelayedChannel(tagger,trig_ch,val + window)
        super(get_gate, self).__init__(tagger,[self.ch[k].getChannel()
                for k in range(len(self.ch))])
```

C.2 TMD_eval

Listing C.2 – TMD evaluation function for raw timestamps in C++

```
/** @brief evaluates a 2x8-bin loopy
* this function evaluates data from an AIT timge tagger: 64 bit time stamp,
*   3 bit channel, 1 bit slope
* the last trigger time is stored in a global variable oldTime64
```

```
*/
void loopy_count(DataPacket_t  RawDataPacket)
{
  int TimetagCnt, Channel;
  struct TimetagI64  *TimetagI64;
  uint64_t Time64;
  long timepos;

  long maxpos_det1[8] =  { 1664,2840,3922,5098,6504,7681,8763,9939 };
    //Peaks detector 1
  long maxpos_det2[8] =  { 1716,2893,3975,5150,6556,7733,8815,9990 };
    //Peaks detector 2
  int window = 30; //coincidence Window
  int trig_ch =0;
  int ch1 =1; // channel for detector1
  int ch2 =2; // channel for detecotr2

  TimetagCnt = RawDataPacket.Header.DataSize;
  TimetagI64 = (RawDataPacket).Data.TimetagI64;
  for (int i = 0; i < TimetagCnt; i++)
  {
    Channel = TimetagI64->Channel;
    Time64 = TimetagI64->Time;
    if (Channel == trig_ch)
      oldTime64 = Time64;
    timepos = Time64 - oldTime64;
    if (Channel == ch1)
    {
      for (int k = 0; k < 4; k++) // from input 1
      {
        if ((timepos < maxpos_det1[k] + window)
          && (timepos > maxpos_det1[k] - window))
        {
          count_mode1++;
        }
      }
      for (int k = 4; k < 8; k++) // from input 2
      {
        if ((timepos < maxpos_det1[k] + window)
          && (timepos > maxpos_det1[k] - window))
        {
          count_mode2++;
        }
      }
    }
    if (Channel == ch2)
    {
      for (int k = 0; k < 4; k++) // from input 1
      {
        if ((timepos < maxpos_det2[k] + window)
          && (timepos > maxpos_det2[k] - window))
        {
        count_mode1++;
```

```
        }
      }
      for (int k = 4; k < 8; k++) // from input 2
      {
        if ((timepos < maxpos_det2[k] + window)
          && (timepos > maxpos_det2[k] - window))
        {
          count_mode2++;
        }
      }
    }
    if (timepos == 0) // this was a trigger
    {
      ckmat[count_mode1,count_mode2]++;
      count_mode1 =0;
      count_mode2 =0;
    }
    TimetagI64++;
  }
}
```

D Local Oscillator

We want to briefly discuss the question why we need a local oscillator (LO) for quantum state characterization. In general, we can distinguish two types depending on the SUT and LO frequency; if SUT and LO have the same frequency, the measurement is called homodyning. Otherwise, the beat frequency of both fields is investigated, which is referred to as heterodyning[1]. In this thesis, we want to concentrate on homodyning schemes. In Chap. 3 we have already seen that we can investigate quantum states by measuring the photon number distribution p_n. However, as we point out in Sec. 4.1.2 performing full quantum state tomography requires a local oscillator (LO). This reference field provides three main advantages.

Firstly, and most importantly, knowing the photon number distribution p_n is not sufficient to characterize the full quantum state. The additional correlations between the individual photon numbers n cannot be seen in this projection. Therefore, a crucial resource to perform full quantum state tomography is a phase reference provided by the LO, which allows interrogating the phases between photon numbers.

Secondly, the local oscillator also provides a reference for the mode structure. Only the overlapping part between our SUT and the LO will interfere, and the remaining part stays unchanged. Therefore, with the knowledge of our LO mode structure, we can characterize the modal structure of our SUT. We will investigate this aspect further in Sec. 4.2.

Thirdly, and specific for WFH, is that many characterization scenarios do not require full quantum state tomography. Instead, showing that the SUT is non-classical with respect to a specific property is sufficient. As an example, we can consider the negativity of the Wigner function for uncovering a non-classical SUT. We have seen that even photon number states $|2n\rangle$ do not show any negativity at the origin. Here, it is beneficial to investigate specific points in the phase space, which can be realized with a LO that displaces the SUT.

In common for all state characterizations is that the LO state itself must be known. Typically the LO is a coherent state which is often readily available in the lab and robust against losses. Nevertheless, other types of LO states have been used [191]. In this thesis, however, we will always assume that the LO is a coherent state.

As a final interesting remark, we can note that for the discussed measurement schemes, neither the quadrature uncertainty nor the photon number variation of the LO (coherent state) degrades the measurement. As an example, we can revisit the direct probing case. The amount of noise that couples to the detector is a linear function of the beam splitter reflectivity and independent of the LO amplitude. Therefore, it is easy to reduce this error source by using a highly transmissive beam splitter [179]. Any imperfection can also be modeled with an additional optical loss followed by a perfect displacement operation. In other words, the additional noise contribution from the LO comes from an additional vacuum-noise term.

[1] Note: alternative definitions for homodyning and heterodyning depending on the beam splitter reflectivity used to combine the SUT and the LO can be found. Sometimes measuring a state with two homodyning setups is also called heterodyning.

E Timing jitter from RF source

The jitter values for two commercial RF-sources were investigated to determine the repetition rate fluctuation. The 76 MHz source is an internal oscillator from the Coherent Synchrolock unit. For the 3.04 GHz signal, we used a commercial signal generator Anritsu MG3690C. The jitter measurements for these sources can be seen in Fig. E.1. The phase noise value for the 3.04 GHz source is much higher as the phase noise value scales with the carrier frequency. The RMS jitter value in fs is carrier frequency independent and can be used to compare these sources. It can be seen that the 76 MHz signal has a slightly better performance.

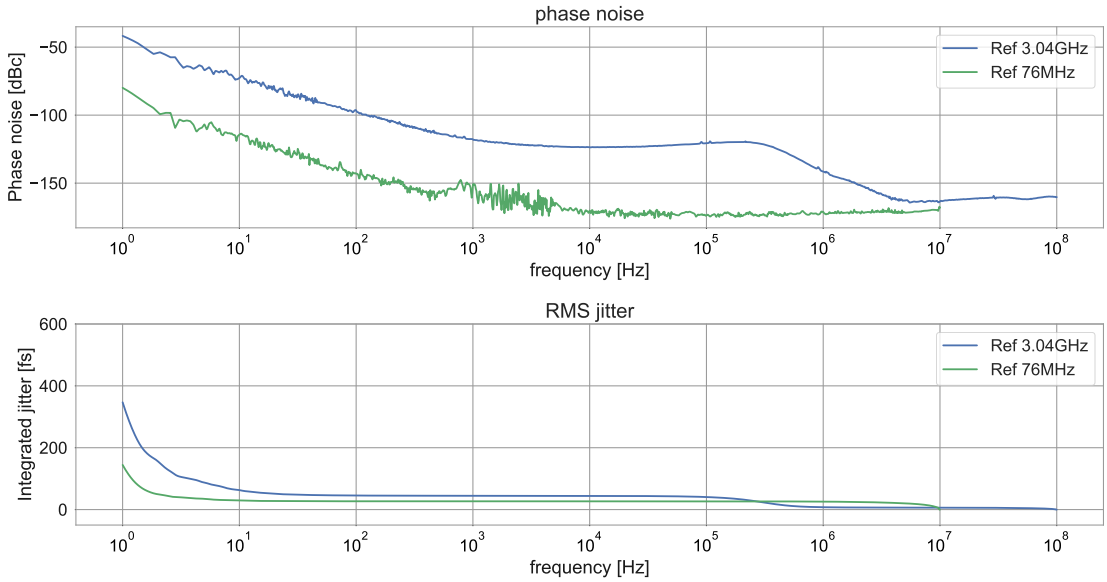

Figure E.1 – Phase noise measurement for two RF-sources. Upper plot shows the phase noise value in respect to the carrier from 1 Hz to 100 MHz sideband frequency. Lower plot shows the RMS jitter value resulting from phase noise integration. See text for further details.

F 128-bin detector

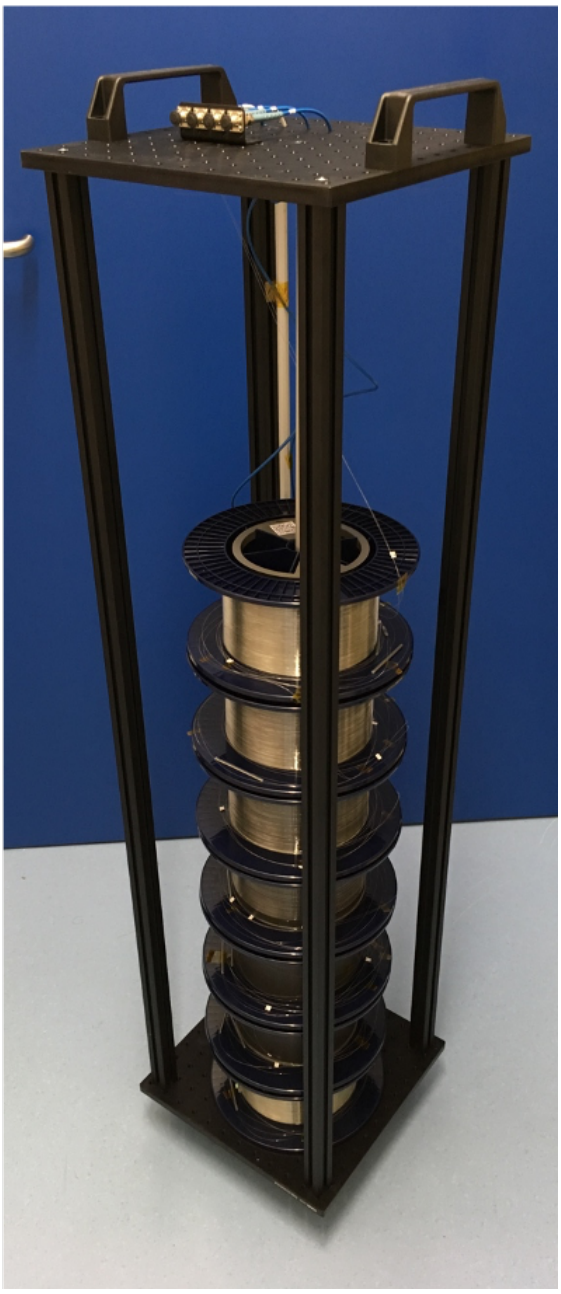

Figure F.1 – Picture of a 128-bin TMD with two input and two output ports (top).